Perera A.G.U., and Ariyawansa G., Terahertz Detection Devices. In: Saleem Hashmi (editor-in-chief), Reference Module in Materials Science and Materials Engineering. Oxford: Elsevier; 2016. pp. 1-49.

Terahertz Detection Devices ☆

AGU Perera, Georgia State University, Atlanta, GA, USA
G Ariyawansa, UES Inc., Dayton, OH, USA

Nomenclature

2D	two dimensional	λ	wavelength
3D	three dimensional	λ_p	peak wavelength
BIB	blocked-impurity-band	λ_t	threshold wavelength
BLIP	background limited infrared performance	**LWIR**	long-wavelength infrared (5–14 μm)
CB	conduction band	**MBE**	molecular beam epitaxy
C–V–T	capacitance voltage temperature	**MWIR**	mid-wavelength infrared (3–5 μm)
D*	detectivity	**NIR**	near infrared (0.8–5 μm)
DWELL	dots-in-a-well	**QD**	quantum dot
FIR	far infrared (30–100 m^{-1})	**QDIP**	quantum dot infrared photodetector
FPA	focal plane array	**QR**	quantum ring
f	frequency	**QRIP**	quantum ring infrared photodetector
f_t	threshold frequency	**QWIP**	quantum well infrared photodetector
FTIR	Fourier Transform Infrared	**QWISP**	quantum well intrasubband photodetector
g	photoconductive gain	**SP**	split-off
η	quantum efficiency	**T**	operating temperature
HEIWIP	Heterojunction Interfacial Workfunction Internal Photoemission	T_{max}	maximum operating temperature
HIWIP	Homojunction Interfacial Workfunction Internal Photoemission	T_{BLIP}	background limited infrared performance temperature
IR	infrared	**THz**	terahertz, 10^{12} Hz
I–V–T	current voltage temperature	**T-QDIP**	tunneling quantum dot infrared photodetector
IWIP	Interfacial Workfunction Internal Photoemission	**UV**	ultraviolet
Jones	shorted form of units of detectivity, cm$\sqrt{\text{Hz}}$ W^{-1}	**VB**	valence band
		VLWIR	very-long-wavelength infrared (14–30 μm)

1   Introduction to Terahertz

Electromagnetic waves propagating at terahertz frequencies (i.e. $1\,\text{THz} = 10^{12}\,\text{Hz} = 33\,\text{cm}^{-1} = 4\,\text{meV}$) are known as terahertz radiation or T-rays. In terms of the wavelength, 300 μm far infrared (FIR) radiation corresponds to the frequency of 1 terahertz. The electromagnetic spectrum from 100 μm (3 THz) to 1 mm (300 GHz) is commonly designated as the terahertz region, however, the region from 30 μm (10 THz) to 100 μm (3 THz) can also be included in the terahertz region. Due to blackbody emission, a full spectrum of radiation including terahertz radiation is emitted by almost all objects with different intensities depending on the temperature of the object. However, terahertz radiation cannot be seen by the human eye since the frequency is almost a factor of 300 lower than the detection limit of the human eye. Unlike heat or thermal radiation (infrared), it cannot be felt due to the very weak energy in a terahertz photon. Similar to X-rays, T-rays have the ability to penetrate clothing, but unlike X-rays will not damage cells or DNA. The ability to penetrate material such as walls and packaging opens up various possibilities including security and commercial applications. This allows one to use terahertz radiation to study various materials without any damage if suitable detectors and sources can be developed. Although electronics and photonics have been heavily studied over the past several decades, the terahertz region which is not in either category was left behind, generating the 'THz Gap'. Recent advances in technology have opened the way for the development of strong terahertz sources. Some of these sources include free electron lasers (Ramian, 1992; Colson *et al.*, 2002), diodes (Siegel, 2002) and quantum cascade lasers (QCLs) (Kohler *et al.*, 2002; Williams *et al.*, 2005). In large accelerator settings, high power terahertz radiation has been observed from relativistic electrons as synchrotron radiation (Carr *et al.*, 2002). Very recently, room temperature quantum cascade terahertz lasers have been reported (Belkin *et al.*, 2008), which in turn has generated renewed interest in developing terahertz detectors. The availability of terahertz systems consisting of high power sources and highly sensitive detectors will open up a wide range of terahertz applications. These include biological, chemical, gas sensing, and imaging; biomolecular, semiconductor, and superconductor characterization; homeland security, environmental, and industrial applications.

Peter Siegel in his review on terahertz technology (Siegel, 2002) reports that the term terahertz can be traced back to the 1970s as listed in the Oxford Dictionary. However, interest in terahertz technology has grown (Colson *et al.*, 2002; Kohler *et al.*, 2002; Carr *et al.*, 2002; Sherwin, 2002; Zhang *et al.*, 2002; Chen *et al.*, 2004) in leaps and bounds since the early 2000s. Terahertz Sensing Technology vols. 1 and 2 (Woolard *et al.*, 2003, 2004) discusses two terminal static or dynamic terahertz devices, system applications, and technology. Here, the focus will be on semiconductor quantum terahertz detectors. Although material growth and characterization is extremely important for detector development efforts, it is not the focus of this work. The terahertz detectors discussed here include free carrier based homo and heterojunction devices, quantum well, and quantum dot (QD) based structures. Blocked impurity band (BIB) detectors and antenna based detectors are also mentioned briefly.
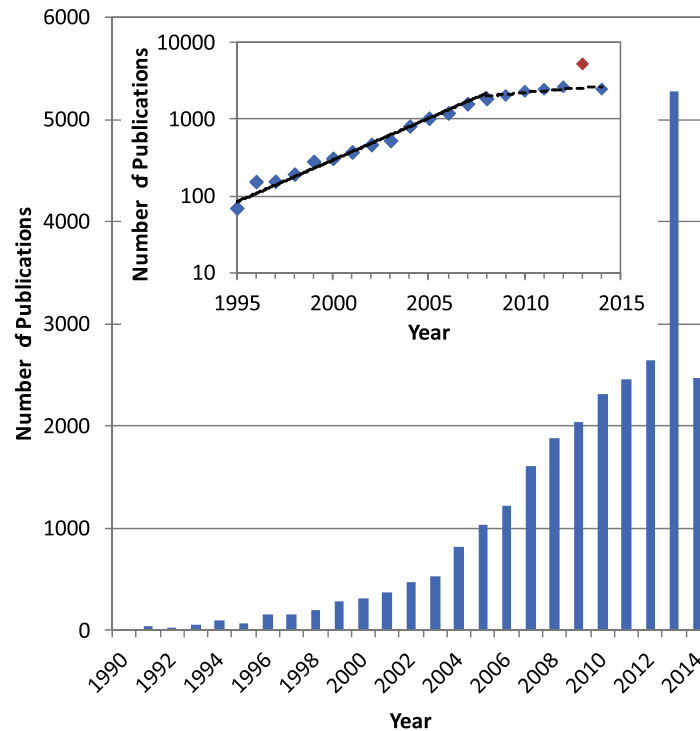
Figure 1 Number of journal publications reported in each year (January–December) as of January 2015 based on a search on the term 'terahertz' in the 'topic' of the ISI Web of Knowledge journals. As shown in the inset, the number of publications shows an exponential growth until 2008. After 2008, it predicts a stable growth in interest of terahertz technology, while a spike in 2013 is clearly observed.

Terahertz spectroscopy (Dexheimer, 2007) has been one of the first terahertz research areas, developed mainly for astronomy applications. Some of the recent work on terahertz science and technology includes Principles of Terahertz Science and Technology by Lee (2008), Terahertz Frequency Detection and Identification of Materials and Objects by Miles *et al.* (2007), Terahertz Optoelectronics by Sakai (2005), Terahertz Science and Technology for Military and Security Applications by Woolard *et al.* (2007), Cutting-edge terahertz technology by Tonouchi (2007), and Sensing with Terahertz Radiation by Mittleman (2004). Most recently, two review articles, *THz* radiation sensors (Sizov, 2010) and Terahertz detectors and focal plane arrays (Rogalski and Sizov, 2011), comprehensively discuss the issues associated with terahertz detectors and focal plane arrays, also discussing various types of terahertz detection devices such as Schottky barrier diodes, pair braking detectors, hot electron mixers and field-effect transistor detectors. A search on the term 'terahertz' as the 'topic' of the ISI Web of Knowledge journals showed roughly an exponential growth in the number of journal articles published until 2008, as shown in **Figure 1**. This trend is similar to the growth of the capacity of memory devices and the speed of microprocessors, which are linked to the Moore's law (i.e., the number gets doubled every year). However, after 2008 a slower but steady rate is observed, while a clear spike can be observed for 2013. Infrared detector development has also kept pace with a similar trend, as shown in **Figure 2**, which hopefully will lead to the elimination of the terahertz gap. The term 'terahertz detector' as the topic was used for the search in ISI Web of Knowledge to generate this figure.

2   Free-Carrier Based Terahertz Detectors

Internal photoemission (IP) detectors were first proposed by Shepherd *et al.* (1971) in Schottky barrier structures. Since then, several different types of internal photoemission detectors have been demonstrated (Shepherd, 1992; Perera *et al.*, 1995; Perera, 2001). Among the most important types are metal-semiconductor Schottky barrier IR detectors, such as PtSi/Si detectors (Kosonocky, 1992) operating in 3–5 µm; semiconductor heterojunction IR detectors, Ge_xSi_{1-x}/Si detectors (Lin and Maserjian, 1990; Tsaur *et al.*, 1991) developed for 8–14 µm or even longer wavelengths; and a degenerate Si homojunction detector (Tohyama *et al.*, 1991), which has a response in the 1–7 µm range. The absorber/photoemitter 'electrode' is a metal, a metal silicide or a degenerate semiconductor in the Schottky barrier, silicide, and degenerate homojunction detectors, respectively. A similar detector concept was proposed and demonstrated by Liu *et al.* using Si MBE multilayer structures in the long-wave infrared (LWIR) range (Liu *et al.*, 1992). However, the basic operating mechanism is the same, and following the terminology of Lin and Maserjian (Lin and Maserjian, 1990), all of these detectors including the free carrier based detectors can be described as Heterojunction or Homojunction Internal Photoemission (HIP) detectors.
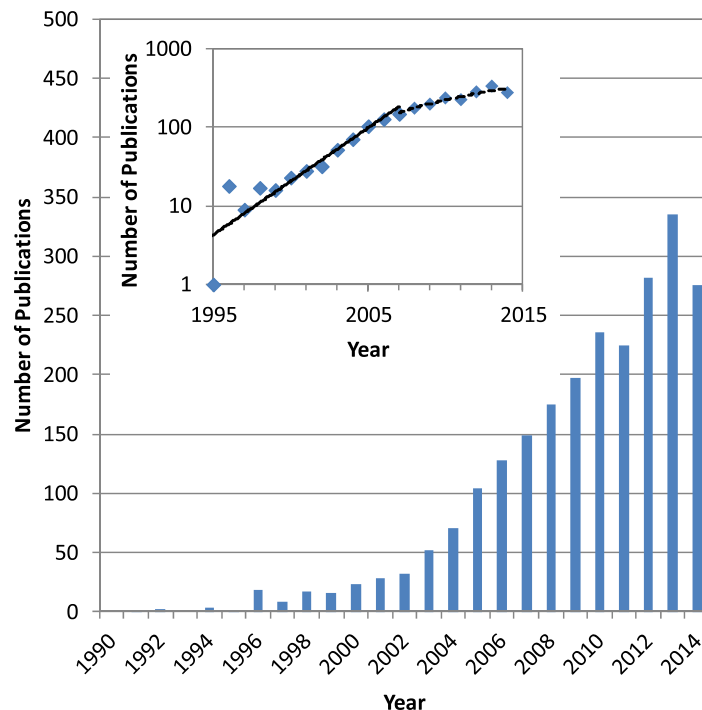
Figure 2   Number of journal publications reported in each year (January–December) as of January 2015 based on a search on the term 'terahertz detector' in the 'topic' of the ISI Web of Knowledge journals. A similar trend as for 'terahertz' is observed for 'terahertz detector', while there is a clear indication of continuous increase in number of publications.

2.1   Types of HIP Detectors

A basic HIP detector consists of a doped emitter layer and an undoped barrier layer. In the homojunction detectors, the absorber/photoemitter will be a doped semiconductor. The doping will cause the bandgap to narrow, forming a barrier at the interface with an undoped layer of the same material. The height and the shape of the barrier will depend on the doping level in the HIP, which can be divided into three types (type-I, -II, and -III) (Perera *et al.*, 1995; Perera and Shen, 1999). These basic types of detectors operate similarly for both *n*- and *p*-doping (except for the carriers; electrons in *n*-type and holes in *p*-type), and will be described here for *p*-type detectors. Significant effective band-gap shrinkage has been observed for heavily doped *p*-type Si (Dumke, 1983), Ge (Jain and Roulston, 1991), and GaAs (Harmon *et al.*, 1994). Better carrier transport properties of GaAs such as higher mobility, will translate into a higher gain, which may produce improved performance for these types of detectors. In the heterojunction case, the only difference is the use of different bandgap materials for the emitter and barrier, which will introduce an additional component for barrier formation.

2.1.1   Type I HIP detectors: $N_a < N_c \left(E_F > E_v^{p^+} \right)$

The type I detectors are characterized by a doping concentration (N_a) in the p^+-layer high enough to form an impurity band but still below the Mott critical value (N_c), so the Fermi level (E_F) is located in the impurity band at low temperatures. The incident FIR light is absorbed by impurity photo-ionization, with a threshold workfunction given by $\Delta = E_F = E_v^{p^+}$, where $E_v^{p^+}$ is the valence band (VB) edge in the p^+-layer. The photoexcited holes are collected by an electric field formed in the *i*-layer due to an external bias. Type I HIP detectors are analogous to semiconductor photoemissive detectors (Escher, 1981) in their operation, which can be described by a three-step process (see **Figure 3(a)**): (1) holes are photoexcited from impurity band states into VB states; (2) phonon relaxation rapidly thermalizes the photoexcited holes to the top of the VB, then diffuse to the emitter/barrier interface, with the transport probability determined by the hole diffusion length; and (3) the holes tunnel through an interfacial barrier (ΔE_v), which is due to the offset of the valance band edge caused by the bandgap narrowing effect, and are collected by the electric field in the *i*-region. The collection efficiency will depend on the tunneling probability and hence on the *i*-region electric field. The threshold frequency, f_t, can be tailored with the doping concentration to some extent, because with the increase of doping concentration, the impurity band broadens and the band edge moves towards the valance band rapidly (Jain *et al.*, 1991).

The impurity compensation effect (Perera *et al.*, 1995), which was neglected in the previous discussion, can induce an electric field in the p^+-layer. This field may extend over a wide region of the p^+-layer for very small compensating concentrations. This is the case of BIB detectors (Petroff and Stapelbroek, 1986; Szmulowicz and Madarasz, 1987), for which the photoexcited carrier collection mechanisms ((2) and (3) above) are replaced by field induced sweep out of the carriers. In contrast to the type I HIP
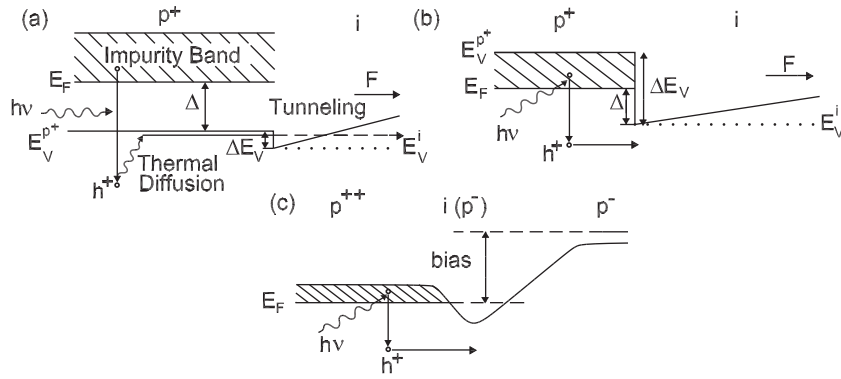
Figure 3 Energy band diagrams for the three different types of HIP detectors for the p-doped case. (a) Type I: $N_a < N_c (E_F > E_v^{p^+})$; (b) Type II: $N_c < N_a (E_v^{p^+} > E_F > E_v^i)$; (c) Type III: $N_a > N_0 (E_F < E_v^i)$. Here, N_c is the Mott critical concentration and N_0 is the critical concentration corresponding to $\Delta = 0$. In (a) and (b), the valence band edge of the i-layer is represented by a dotted line for $V_b = V_0$ (flatband) and by a solid line for $V_b > V_0$. Reused with permission from Perera, A.G.U., 2001. Handbook of Thin Film Devices: Semiconductor optical and Electro optical Devices. Copyright 2001, Academic Press.

detector, the BIB detector resembles a reverse-biased photovoltaic detector in its operation, with the collection efficiency in the electric field region approaching 100%. However, if the compensated acceptor concentration is high in the majority of the p^+-layer there is no electric field induced when an external voltage is applied, except for a very small depletion region near the p^+-i interface. In this case, the photoresponse mechanism can still be described by the processes developed above for type I HIP detectors.

2.1.2 Type II HIP detector: $N_c < N_a < (E_v^{p^+} > E_F > E_v^i)$

For doping concentrations above the Mott transition, the impurity band merges with the VB, and the p^+-layer becomes metallic. However, as long as the concentration does not exceed a critical concentration N_0, the Fermi level can still be above the VB edge of the i-layer ($E_F = E_v^i$) due to the bandgap narrowing effect. The difference between the Fermi level and the VB edge in the barrier then forms a workfunction $\Delta_d = E_F - E_v^i$ at the emitter/barrier interface as seen in **Figure 3(b)**. The detectors operate by free carrier absorption, followed by internal photoemission of the excited carriers and sweepout of the emitted carriers by an externally applied electric field. Since the workfunction in theory can be reduced to a small value as desired by adjusting the doping concentration there is no restriction on threshold frequency (f_t). However, the f_t was found to be limited by hole transitions (Rinzan *et al.*, 2005b). Although the free carrier absorption in Type II HIP detectors is less than what is found in Schottky barrier detectors which they resemble, they have a higher internal quantum efficiency due to a lower Fermi level and increased hot electron scattering lengths. For heterojunction detectors, the only difference is the barrier which has an additional component Δ_x from the band offset due to the material difference, making the total workfunction $\Delta = \Delta_d + \Delta_x$. The basic absorption, photoemission, and collection will be the same as in the homojunction case.

2.1.3 Type III HIP detector: $N_a > N_0 (E_F < E_v^i)$

When the doping concentration is so high that the Fermi level is above the conduction band (CB) edge of the i-layer, the p^+-layer becomes degenerate. The space charge region causes a barrier to form at the p^+-i interface due to the electron diffusion, as shown in **Figure 3(c)**. The barrier height depends on the doping concentration and the applied voltage, giving rise to an electrically tunable f_t. This type of device was first demonstrated by Tohyama *et al.* (1991) using a structure composed of a degenerate n^{++} hot carrier emitter, a depleted barrier layer (lightly doped p, n or i), and a lightly doped n-type hot carrier collector. As the bias voltage is increased, the barrier height is reduced, the spectral response shifts toward lower frequency, and the signal increases at a given frequencies. The photoemission mechanism of type III HIP detectors is similar to that of type II HIP detectors, with the major difference in that they have different response frequency (wavelength) ranges and different operating temperature (T) ranges due to diferences in the barrier heights. The type II HIP detector is a FIR detector, and usually operates at temperatures much lower than 77 K. In contrast, the type III HIP detectors operate near 77 K and have responses in the MWIR and LWIR ranges (Shepherd, 1992).

2.2 Workfunction Dependence on Doping Concentration Above the Mott Transition

The type II HIP detectors can be further categorized as Homojunction Interfacial Work-function Internal Photoemission (HIWIP) and HEterojunction Interfacial Workfunction Internal Photoemission (HEIWIP) detectors. The only difference between the HIWIP and HEIWIP detectors will lie in the source of the barrier offset forming the workfunction. In the HIWIPs, the offset will be solely due to effects of doping in the emitter, while in the HEIWIPs the majority of the offset is due to the band offsets coming from material difference, although doping can also contribute.

When the doping concentration is above the metal-insulator transition (Mott transition) value, the detector can be regarded as a metal photoemitter (type II detector), which was denoted as homojunction interfacial workfunction internal photoemission (HIWIP) FIR detectors (Perera et al., 1995), otherwise it can be regarded as a semiconductor photoemitter (type I detector). Following a linearly distributed space charge model (Haegel, 1988), it was shown that the space charge effect at the interface is negligible at low temperatures.

2.2.1   Barrier height variation in HIWIPs

As the doping concentration increases, the impurity band broadens and becomes increasingly asymmetrical, and its peak moves towards the CB edge rapidly. At the same time, the CB edge also starts moving downwards in the bandgap. At the Mott transition concentration, the impurity band and the CB merge with each other, and the semiconductor changes from a nonmetal to a metal (Mott transition). Above the Mott transition, with further increasing the doping concentration, the impurity band starts to shrink and finally becomes absorbed into the CB (Jain et al., 1991).

It has been shown (Perera and Shen, 1999) that raising of the VB edge ΔE_c (lowering of the CB edge, ΔE_c) can be described using the high-density (HD) theory. HD theory (Jain et al., 1991) describes the behavior of heavily doped Si, GaAs and Ge to a fair degree of accuracy in the high-density regimes, i.e., above the Mott critical concentration, and gives reasonable results even at doping concentrations as low as 10^{18} cm^{-3}. The main result of this theory is that the electron-electron interaction (many-body efect) causes a rigid upward (downward) shift of the valence (conduction) band, ΔE^{ex}, which is also known as the exchange energy. The electron-impurity interaction causes an additional shift, ΔE_i, and also distorts the density of states function. In this theory, the semiconductor is assumed to be uncompensated with completely ionized impurities so that the free carrier concentration is equal to the doping concentration N_d. In principle, this theory is valid close to 0 K.

Jain and Roulston (1991) have derived a simple and accurate expression for the shift of the majority band edge, ΔE_{max}, that can be used for all n- and p-type semiconductors and for any doping concentration in the high-density regime. By introducing a correction factor to take deviations from the ideal band structure (anisotropy of bands for n-type material) into account the workfunction for the homojunction has been obtained (Perera and Shen, 1999). The threshold frequency is given by $f_t(\text{THz}) = 0.242\,\Delta$ (meV).

As seen in **Figure 4**, as N approaches N_0, f_t becomes very sensitive to N, hence, only a small increase in N can cause a large increase in f_t. It should be pointed out that although the high-density theory is valid in the high doping range ($N > N_c$), it cannot be used for moderately doped semiconductors where N is in the neighborhood of N_c (Jain et al., 1991). The metal-to-nonmetal transition and several properties of moderately doped semiconductors, such as the Fermi level position, the shape of density-of-states which is highly distorted in this case, cannot be modeled by this theory.

To determine the Δ vs N relationship in the intermediate doping range, other theories, such as Klauder's multiple scattering theory (Klauder, 1961), are needed. In theory, the work function Δ_d can be varied almost close to zero by controlling the doping concentration giving rise to wavelength tailorable HIWIP detectors.

2.2.2   Barrier height variation in HEIWIP

HEIWIP detectors which combine the free carrier absorption of the HIWIP (Homojunction Interfacial Workfunction Internal Photoemission) detectors (Shen et al., 1997) with the material composition of Quantum Well Infrared Photodetectors (QWIPs) have been experimentally demonstrated (Perera et al., 2001), covering the frequency range from 2.42 to 75 THz. The typical HEIWIP detector structure consists of a p-doped GaAs emitter (absorber) region followed by an undoped AlGaAs barrier region. Although the structure appears similar to a p-type QWIP the emitter/absorber in a HEIWIP is thicker than the well of a QWIP. As a result the carriers form a 3-dimensional distribution in HEIWIPs rather than being in quantized states as in a QWIP. The basic idea of HEIWIP detectors is to add the VB offset for the GaAs/AlGaAs interface to the offset from the doping (N_A) in the emitters. The contribution from the doping (Δ_d) is the same as for HIWIPs. The Al fraction contribution is taken as $\Delta_{Al} = (x^*530)$ meV where x is the Al fraction. The total barrier at the interface is then $\Delta = \Delta_d + \Delta_{Al}$.

The threshold frequency can be determined directly from $f_t = \Delta/4.133$ where f_t is in THz and the workfunction Δ is in meV. A practical lower limit for the Al fraction will be around $x \geq 0.005$ with $f_t \geq 2.7$ THz. Further decrease in f_t below 2.7 THz (i.e. beyond ~ 110 μm) requires a change in the design due to the minimum $\Delta = \Delta_d$ from the bandgap narrowing. One possible approach to avoid this limit is to use AlGaAs as the emitter and GaAs as the barrier (Rinzan et al., 2005b). In such a device the bandgap narrowing in the doped AlGaAs is partially offset by the increased bandgap of the AlGaAs material relative to the GaAs, giving $\Delta = \Delta_d - \Delta_{Al}$. For example, a $f_t = 0.9$ THz (335 μm) detector would have an Al fraction of ~ 0.01. The FIR absorption in AlGaAs is very similar to GaAs (Rinzan et al., 2005a), due to the very low Al content giving performances similar to the devices with AlGaAs barriers. Another approach is to increase doping concentrations to reduce the bandgap narrowing contribution. This has been done in n-type GaAs/AlGaAs structures (Weerasekara et al., 2007) leading to detectors with response out to 3.2 THz. The variation of the threshold frequency with the Al fraction for n-type AlGaAs HEIWIPs and p-type HEIWIPs using both GaAs and AlGaAs emitters is shown in **Figure 5**, The experimentally observed thresholds are represented by symbols, which will be discussed later.
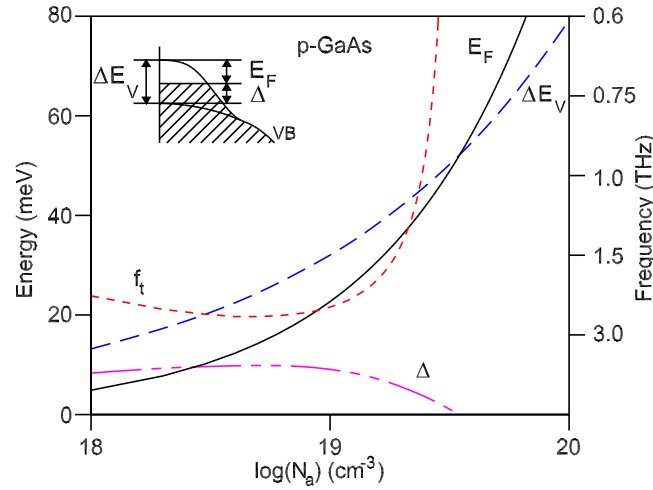
Figure 4 Doping concentration dependence of ΔE_c (ΔE_v), E_F, Δ, and f_t, calculated using the high-density theory for p-type GaAs. Reused with permission from Perera, A.G.U., 1999. Opto-Electronics Review, 7, 153–180.Copyright 1999, Springer.
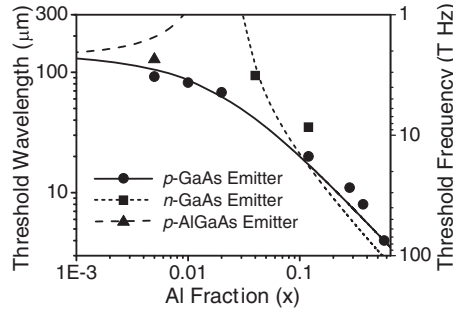
Figure 5 The variation of the threshold frequency with Al fraction for n-type HEIWIPs using GaAs emitters, and for p-type HEIWIPs with GaAs and AlGaAs emitters. The symbols represent the experimentally observed thresholds, which will be discussed later.

2.3 Light Propagation in the Structure

The radiation propagation in a semiconductor detector structure has been described (Esaev et al., 2004a) by the matrix method (Klein and Furtac, 1986), using the complex refractive index and complex permittivity (Blakemore, 1982). The propagation through the whole structure is described by the matrix Q (Esaev et al., 2004a)

$$\begin{pmatrix} E_{tr} \\ E_{ref} \end{pmatrix} = Q \cdot \begin{pmatrix} E_0 \\ E_{0ref} \end{pmatrix} \tag{1}$$

where E_0 is the amplitude of the incident radiation. The transmission $t = E_{tr}/E_0$ and the reflection $r = E_{0ref}/E_0$ coefficients for the structure were then found from the condition that at 'infinity' there is no reflected wave, and so $E_{ref} = 0$. This leads to

$$r = -Q_{2,1}/Q_{2,2}; \quad t = \det(Q)/Q_{2,2} \tag{2}$$

Transmittance $\mathcal{T}$ and reflectance $\mathcal{R}$ of the structure were defined as $\mathcal{T} = |t|^2$ and $\mathcal{R} = |t|^2$. Total absorption in the structure were calculated as the difference between unity and the sum of the reflectance and transmittance $\mathcal{A} = 1 - \mathcal{T} - \mathcal{R}$.

The optical electric fields in the $(j)^{th}$ layer at a distance z from the incident surface are

$$\begin{pmatrix} E_j^+(z) \\ E_j^-(z) \end{pmatrix} = \begin{pmatrix} \exp(ik(\omega)n_j z) & 0 \\ 0 & \exp(-ik(\omega)n_j z) \end{pmatrix} \cdot \tilde{Q} \cdot \begin{pmatrix} 1 \\ r \end{pmatrix} \cdot E_0 \tag{3}$$

where matrix $\tilde{Q}$ is a matrix for the first to $(j-1)^{th}$ layers. Optical electric field distribution across the structure is given by $|E_j(z)|^2 = |E_j^+(z) + E_j^-(z)|^2$.

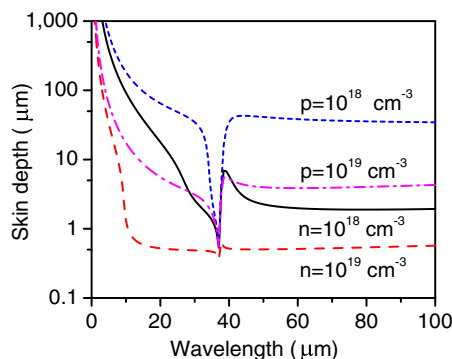**Figure 6** Skin depth for infrared radiation in GaAs with both *n*- and *p*-type doping of 10^{18} and 10^{19} cm^{-3}. The skin depth is relatively constant at low frequencies and increases rapidly at high frequencies. The feature between 8.5 and 7.5 THz (35 and 40 μm) is due to the reststrahlen effect. Skin depth is least for *n*-type material. Reused with permission from Esaev, D.G., 2004. Journal of Applied Physics, 96, 4588. Copyright 2004, American Institute of Physics.

The depth to which the incident radiation penetrates into the layers, skin depth $\delta(\omega)$, depends on the frequency, doping concentration *N*, and effective mass of the free carriers. The variations of $\delta(\omega)$ with frequency for an *n*- and *p*-type GaAs layers with doping concentrations 10^{18} and 10^{19} cm^{-3} have been calculated (Esaev *et al.*, 2004a) and are shown in **Figure 6**. At higher frequencies, $\delta(\omega)$ is high and has a strong frequency dependence, while at lower frequencies $\delta(\omega)$ approaches a saturation. Hence, a thin emitter layer will be almost transparent to higher frequencies providing a negligible contribution to the photo current.

It is suggested that due to the shorter skin depth of *n*-type layers at the same doping concentration causing higher reflectivity than *p*-type, *n*-type layers are better for mirrors inside the structure, allowing selective increase of absorption of photons at desired frequencies (Esaev *et al.*, 2004a), leading to enhanced detector response. A model for optimizing the response has been suggested (Zhang *et al.*, 2002), with experimental confirmation of enhanced absorption in a device structure (Zhang *et al.*, 2003).

2.4 Responsivity

The responsivity of a photodetector at frequency *f* is given by (Esaev *et al.*, 2004a)

$$R = \eta g_p \frac{q}{hf} \tag{4}$$

where *h* is Planck's constant, η is total quantum efficiency, and g_p is the photoconductive gain. The responsivity calculations included effects of photoexcitation of carriers in the emitter, hot carrier transport, thermalization, and photoemission into the barrier. Total quantum efficiency (Perera *et al.*, 1995) which is the product of photon absorption η_a, internal photoemission η_i, and hot-carrier transport probabilities is given as η_t, $\eta = \eta_a \eta_i \eta_t$. The η_i was described by an 'escape cone' model (Williams, 1970), and η_t followed the Vickers–Mooney model (Vickers, 1971; Mooney and Silverman, 1985).

The absorption probability is proportional to the imaginary part of the permittivity. In determining the absorption for use in responsivity only the photoexcitation is included, and not the contributions from phonon generation. Radiation absorbed via optical phonon generation is dissipated in the crystal lattice, without producing any hot carriers, and hence does not contribute to the photocurrent. The absorption coefficient is related to the skin depth as a $a(f) = 2/\delta(f)$. As shown in **Figure 6** and $\delta(f)$ for *n*-type GaAs is about ten times lower than for *p*-type at doping concentrations of 10^{19} cm^{-3} for frequencies lower than 38 THz. This increased absorption is due to the reduced carrier mass of the electrons compared to the holes. Details of the responsivity calculations can be found in Esaev *et al.* (2004a).

2.5 Dark and Noise Current

The dark current of a detector plays a major role in the device performance. Dark current variation with temperature allow the determination of the work function through Arrhenius plots (Sze, 1981). Dark current in the HEIWIP structure is a sum of the thermo-emission current over the barrier and the tunneling current through the barrier (Perera *et al.*, 1995). The thermionic current in the HEIWIP structure can be described in the frame of the 3D carrier drift model (Kane *et al.*, 1992). The measured and calculated dark currents and the 300 K photocurrent for a HEIWIP detector with a threshold frequency of 4.6 THz at various temperatures are shown in **Figure 7**.

As THz detectors typically operate at low temperatures, the thermal noise is typically negligible in these detectors. Hence the primary sources of noise in the devices are the shot noise from the injection of carriers into the detector at the contact barrier interface, and the generation–recombination (g–r) noise from the carrier capture and emission from trap states. In most cases, the
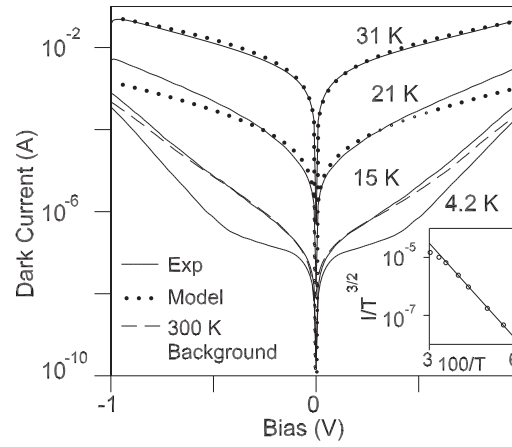
Figure 7   Dark current at various temperatures for the HEIWIP detector. The dark current at 10 K is almost the same as for 4.2 K. Also shown is the 300 K background current (dashed line) indicating BLIP operation at 14 K. Reused with permission from Perera, A.G.U., 2001. Applied Physics Letters, 78, 2241. Copyright 2001, American Institute of Physics.

shot noise will dominate the g–r noise at high frequencies and the noise current is related (Levine, 1993) to the mean current through the detector, $\bar{I}$ by

$$I_{noise}^2 = 4q\bar{I}g_n\Delta f \qquad [5]$$

where g_n is the noise gain and δf is the measurement bandwidth.

The noise gain g_n and photocurrent gain g_p are given by (Ershov and Liu, 1999)

$$g_n = \frac{1 - p_c/2}{p_c(N+1)} + \frac{1 - (1-p_c)^{N+1}}{p_c(N+1)^2[1-p_c)^N]} \qquad [6]$$

$$g_p = \frac{1}{p_cN} \qquad [7]$$

where p_c is the capture probability of a carrier traversing an emitter, and N is the number of such emitters. The ratio g_n/g_p varies from 0.5 to 1 when p_c varies from 0 to 1 and N from 1 to infinity. Hence, the difference between them may be ignored in many applications, particularly if the capture probability is low.

Typical noise current spectra (Perera and Shen, 1999) of a p-GaAs HIWIP FIR detector at 4.2 K for various forward bias values are presented in **Figure 8**. Similar noise behavior was observed under reverse bias conditions. All the spectra display $1/f$ noise dependence at frequencies (f) below 1 kHz and are independent of frequency at higher values.

The $1/f$ noise power density is proportional to I_d^α with an α value of 2.05–2.10. This type of behavior indicates that the origin of the $1/f$ noise could be interpreted in terms of a random fluctuation in the occupancy of the interface trap centers which can lead to generation–recombination (g–r) $1/f$ noise (Jantsch, 1987). Two representative models of the $1/f$ noise have been proposed (Shklovskii, 1980; Luo et al., 1988).

The noise measurements could also be used for gain determination (Levine, 1993). For frequencies above 1 kHz, the noise was independent of frequency and was dominated by shot noise. The determined gain increases rapidly with bias at low voltages and then saturates (Perera and Shen, 1999). This behavior is similar to the case of QWIPs (Levine, 1993). The highest value of g recorded for this detector was $\sim$0.95 (Perera and Shen, 1999) at a bias corresponding to the highest responsivity, in good agreement with the estimation of 0.984, by combining the experimental responsivity and quantum efficiency.

2.6   Homojunction Detectors

HIWIP detectors have been demonstrated based on different material systems. In general, the doping in the emitter of HIWIP detectors is higher than that of HEIWIP detectors. While p^+-Si/Si HIWIPs were developed (Perera et al., 1998a) some times ago, p^+-GaAs/GaAs HIWIPs were started to be developed due to the rapid development and growth of GaAs. Presently, HIWIPs based on other materials, such as GaSb (Jayaweera et al., 2007), have also been tested, however, the progress of growth techniques plays a role for these new materials to be used for potential high performance detectors. In HIWIPs, the active region consists of a junction formed by a doped layer (emitter) and undoped layer (barrier) made of the same material. The primary detection mechanism in a
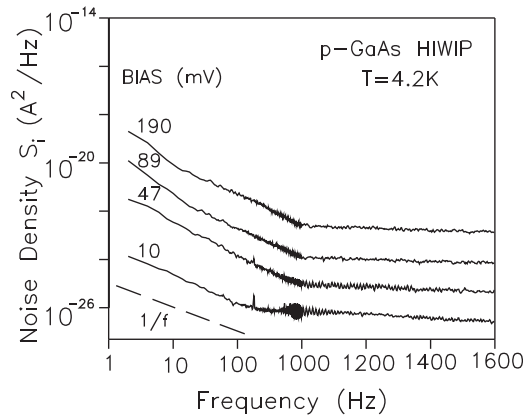
Figure 8 Measured dark current noise spectra of p-GaAs HIWIP far-infrared detector at 4.2 K for various forward biases. The dashed line represents the $1/f$ dependence of the noise power density S_i. Reused with permission from Perera, A.G.U., 1999. Opto-Electronics Review, 7, 153–180. Copyright 1999, Optical Society of America.

Table 1   A comparison of different terahertz HIWIP detectors. Here, f_t is threshold frequency, R_p is peak responsivity, f_P is peak frequency, and D^* is detectivity

Reference	Material system	f_t (THz)	R_p (A W^{-1})@ fp	T (K)	D^* (Jones)
Perera *et al.* (1998a)	p^+-Si/Si	6.25	12.3 @ 10.9	4.2	6.6×10^{10}
Ariyawansa *et al.* (2006b)	p^+-Si/Si	8.6	1.8 @ 12	4.6	1.2×10^{11}
Jayaweera *et al.* (2007)	p^+-GaSb/GaSb	3.1	9.7 @ 8.3	4.9	5.7×10^{11}
Shen *et al.* (1997)	p^+-GaAs/GaAs	3.0	3.1 @ 8.9	4.2	5.9×10^{10}
Esaev *et al.* (2004b)	p^+-GaAs/GaAs	4.3	7.4 @ 8.8	4.2	3.6×10^{11}

HIWIP involves free carrier absorption, internal photoemission across the barrier and the carrier collection. The interfacial workfunction (Δ), which arises due to doping different in the emitter and the barrier, determines the terahertz threshold. Several HIWIPs are listed in **Table 1**.

2.6.1 p^+-Si/Si HIWIP detectors

A THz response was reported in Si p–i–n diodes (Perera *et al.*, 1992, 1993) showing a threshold of 5.26 THz (57 μm) with a peak response of 1.5×10^4 V W^{-1} at 10 THz (30 μm). Another Si p–i–n diode (Perera *et al.*, 1992) showed a response up to 1.36 THz (220 μm) at 1.5 K. Following this, a Silicon p-type sample was specifically developed for HIWIP THz response (Perera *et al.*, 1998a). The spectral response at 4.2 K measured at different forward biases and having a wide spectrum with high responsivity is shown in **Figure 9**. The long tailing behavior at low frequencies reflects the nature of internal photoemission. The responsivity has a similar spectral shape and strong bias dependence for both polarities, increasing significantly with increasing bias. However, the bias cannot increase indefinitely as the dark current also increases with bias.

Several sharp peaks were seen in the spectra under high biases, becoming stronger with increasing bias. At low biases, the photoconductivity is due to the usual photon capture by the impurity states, where f_t of the response is determined by the energy gap Δ. At high biases, for high enough doping concentration, the wave functions of excited impurity states overlap, leading to hopping conduction among ionized dopant sites. These peak positions are in good agreement with the theoretical energies of transitions from the ground states to the first (2P$_0$), second (3P$_0$) and third (4P$_0$) excited states (marked by arrows in **Figure 9**) (Perera *et al.*, 1998a). For this device the f_t was reported (Perera *et al.*, 1993) as 6.25 THz at low biases, decreasing to around 3.30 THz at a bias of 0.791 V. The highest responsivity reported was 12.3 ± 0.1 Å W^{-1} at 10.9 THz (in the flat region), and 20.8 ± 0.1 Å W^{-1} at 9.55 THz (in the spike region). Hopping conduction can be clearly seen in the I–V data in the inset of **Figure 9**, where the dark current increases rapidly with bias above 0.75 V. The highest D^* (6.6×10^{10} Jones for 4.2 K under a bias of 10 mV at 10.9 THz) occurred at low biases, since the dark current increases rapidly with the bias. However, D^* also increases slightly with the bias due to the rapid increase in responsivity, and finally decreases again due to the onset of hopping conduction.

2.6.2 p^+-GaSb/GaSb HIWIP detector

A p^+-GaSb/GaSb HIWIP detector structure responding up to 3.1 THz has also been reported (Jayaweera *et al.*, 2007). In a separate publication (Perera *et al.*, 2008), it has been reported that a similar GaSb-based HIWIP detector also responds with a flat response in the terahertz range 3–1.5 THz as shown in **Figure 10**. The sharp dip at $\sim$7 THz (43 μm) is due to reststrahlen absorption in
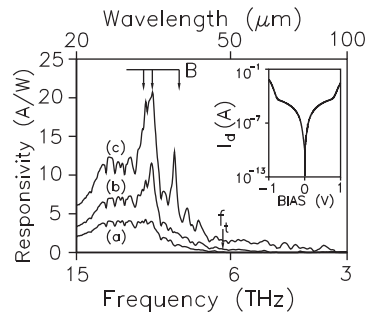
Figure 9 Spectral response of p-Si HIWIP FIR detector measured at 4.2 K under different forward (top positive) bias V_b (a) 0.377 V, (b) 0.539 V, and (c) 0.791 V. A peak responsivity of 12.3 Å W^{-1} is observed at 10.9 THz (27.5 μm) in curve (c). The sharp response peaks are associated with excited impurity states with the theoretical energy levels marked by arrows. The other minor features are due to the instrument response function against which the detector output was ratioed. The inset shows the variation of the dark current, I_d, with bias at 4.2 K. Reused with permission from Perera, A.G.U., 1998. Applied Physics Letters, 72, 2307. Copyright 1998, American Institute of Physics.

GaSb. Based on the Arrhenius calculation, the activation energy was reported as 128 meV, which is in good agreement with the observed free carrier threshold of 3.1 THz. The flat response in the range 3–1.5 THz is relatively weak compared to the free carrier response, but is an order of magnitude higher than the system noise level as shown in **Figure 10**. Although the mechanism of this response has also not been established yet as in the case of terahertz response in GaN/AlGaN structure, this result also implies the possibility of developing GaSb/InGaSb terahertz HEIWIP detectors, which would provide flexibility in controlling the threshold with the In fraction. Based on the lower band gap offset between GaSb and InSb, it is clear that f_t of 1 THz could be achieved, while keeping the In fraction in the practical range. Therefore, GaSb based HEIWIPs would also be possible substitutions for GaAs, where high accuracy of the alloy fraction (Al fraction in AlGaAs) is needed to control the threshold.

2.6.3 p^+-GaAs/GaAs HIWIP detectors

The spectral responses reported at different forward biases for a GaAs HIWIP sample consisting of 20 periods of 4×10^{18} cm^{-3} doped GaAs emitters and undoped GaAs barriers are shown in **Figure 11**. This was the highest response as well as the lowest threshold frequency (3.0 THz) reported for GaAs HIWIP detectors (Shen *et al.*, 1997). The long tailing behavior in the low frequency region reflects the nature of internal photoemission. This detector reported a peak response of 3.1 A/W for a bias of 192 mV, and the peak D^* was 5.9×10^{10} Jones for a bias of 83 mV at 4.2 K and 8.9 THz. (Esaev *et al.*, 2004b).

2.7   Light-heavy hole transition effects

While in principle the barrier height can be reduced to any desired value by increasing the doping in the emitter, it was reported (Perera *et al.*, 2003) that the transitions between the light and heavy hole states in detectors lead to an increase of the threshold frequency. The measured and calculated from HD theory Δ and f_t values as well as the values predicted from the light-heavy hole transitions are shown in **Figure 12**. This calculation (Shen *et al.*, 1998) used a modified Fermi level expression, which provides a correction for the difference in the values for the Fermi level determined by the conventional density of state calculation and the values determined by the experimental luminescence spectra (Jain and Roulston, 1991). From this correction, the effect on the work function was $\sim 5 \pm 1$ meV, as can be observed from a comparison between the curves in **Figures 4** and **12**. The reported values of Δ were obtained using Arrhenius plots of the current vs temperature, while f_t was obtained from the spectral measurements. For low doping densities ($< 10^{19}$ cm^{-3}) the predicted values of both quantities were in good agreement with the measured values. However, at higher doping where f_t was expected to decrease, it remained nearly constant even though the measured Δ decreased as expected. The differences between spectral and Arrhenius results were explained (Perera *et al.*, 2003) in terms of direct excitations from the heavy to light hole bands. For highly doped materials, the carriers excited directly into the light hole band can escape leading to reduced population in the heavy hole band, and hence an increased threshold frequency. This is the reported cause for the limit on the effective threshold for p-type detectors even at high doping (Perera *et al.*, 2003).

2.8   BIB Detectors for Terahertz Applications

As mentioned previously, the BIB detectors are related to type I HIP detectors. These detectors have been of extensive interest for FIR/THz applications due to their low dark current (Petroff and Stapelbroek, 1986). A BIB detector structure is formed by a thin undoped semiconductor layer (barrier) and a thick highly doped layer (absorber). Depending on the dopant (or the impurity), the structure can be either n-type or p-type. The detection wavelength corresponds to the binding energy of the donor or the acceptor atoms in the material. Most of the BIB detectors were fabricated using Si and Ge materials. In Si BIB detectors, As and Sb (Stetson *et al.*, 1986; Reynolds *et al.*, 1989; Huffman *et al.*, 1992) are the commonly used impurities, a response upto 10 THz was obtained
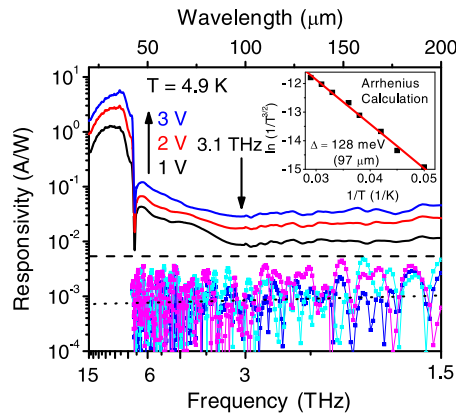
Figure 10 The response of a p^+-GaSb/GaSb HIWIP detector in the 15–1.5 THz range at 1, 2, and 3 V bias voltages at 4.9 K. The arrow indicates the free carrier response wavelength threshold at the 3.1 THz (97 μm). The noise curves at the bottom were obtained under dark conditions, and the dashed line shows the maximum noise level of the spectral response measurement setup. The Arrhenius curve, which translates to a activation energy of 128 meV (97 μm) is also shown in the inset. Reused with permission from Perera, A.G.U., 2008. Microelectronics Journal 39, 601. Copyright 2008, Elsevier.
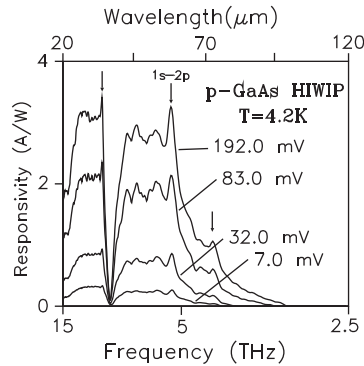

Figure 11 Spectral response measured at 4.2 K for a p-GaAs HIWIP detector with emitters doped to 8×10^{18} cm^{-3} at different forward biases. Reused with permission from Shen, W.Z., 1997. Applied Physics Letters, 71, 2677. Copyright 1997, American Institute of Physics.
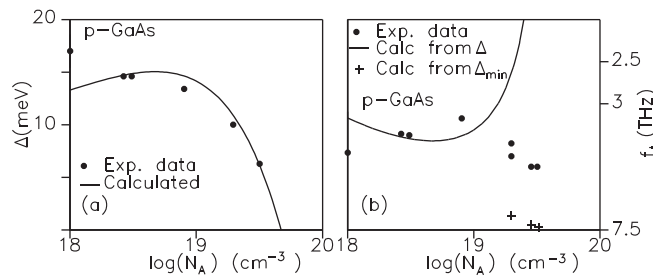
Figure 12 Plots of (a) calculated and measured (based on from Arrhenius analysis) work-function Δ and (b) calculated and measured (from response spectra) f_t vs. doping in HIWIP detectors. The solid line indicates the results from the HD theory while the points (•) are the experimental results. Also shown in (b) are the threshold limit ($+$) calculated from the heavy-light hole transition. Reused with permission from Perera, A.G.U., 2003. Infrared Physics & Technology, 44, 347. Copyright 2003, Elsevier.

depending on the impurity (Sclar, 1984; Rogalski, 2003). However, Si BIB detectors are not discussed here since they are not promising for the THz range below 10 THz.

For terahertz detection, Ge:Ga BIB structures attracted the attention, demonstrating terahertz detectors with thresholds upto 1.6 THz (Watson and Huffman, 1988). In 1993, Watson et al. (1993), the threshold has been extended to 1.36 THz with a quantum efficiency of ∼14%. However, integrated cavity architecture could further increase the efficiency upto 100% (Lifshifts et al., 1967). A list of several terahertz BIB detectors are given in **Table 2**. Recently, a Ge:Sb BIB detector (Bandaru et al., 2002)

Table 2 Several terahertz BIB detectors along with their performances. Here, f_p is peak frequency, f_t is threshold frequency, n is efficiency, and T is operating temperature

Reference	Material system	f_p (THz)	f_t (THz)	η %	T (K)
Watson et al. (1988)	Ge:Ga	2	1.6	4	1.7
Watson et al. (1993)	Ge:Ga	2	1.36	14	1.7
Bandaru et al. (2002)	Ge:Sb	2.5	1.5	-	2
Beeman et al. (2007)	Ge IBIB	–	1.35	1.2	1.3

grown by liquid phase epitaxy on a pure Ge substrate has shown a response threshold of ~ 1.5 THz. Extending the threshold further, Beeman et al. (2007) demonstrated an ion-implanted BIB (IBIB) detector with a threshold of 1.35 THz.

Lately, there has been work on developing GaAs based BIB detectors (Reichertz et al., 2005; Reichertz et al., 2006; Haller and Beeman, 2002). In GaAs BIB detectors, the low donor binding energy, giving rise to an impurity transition energy of ~ 4.3 meV, is the key for terahertz detection. According to Reichertz et al. (2006), detection of terahertz radiation upto 1 THz could be expected. However, the material quality in the barriers of BIB structures needs to be very high in order to obtain high performance. This has been one of the problems for GaAs BIB detectors, hence, only preliminary results are presently available. Recently, Cardozo et al. (2005) has reported high absorption of terahertz radiation near 1 THz for a GaAs BIB structure grown by liquid phase epitaxy. Also, the absorption coefficient drops to 50% of the maximum at 0.9 THz.

2.9 Heterojunction Detectors

The difficulties of controlling the barrier height and extending the threshold to low THz frequencies has led to the development of the HEIWIP detectors (Perera and Matsik, 2007) which use the Al fraction in one or both of the layers to control the workfunction. The band diagram for two different types of HEIWIP detectors using GaAs and AlGaAs are shown in **Figure 13**. The choice between these two types of detectors is determined by the desired threshold frequency. The first type (**Figure 13(a)**) is the standard HEIWIP detector, which uses doped GaAs emitters and undoped AlGaAs barriers. The contributions from the doping and Al fraction to the workfunction are both in the same direction, i.e. increasing the Al fraction can increase the threshold frequency from a minimum of ~ 2.72 THz for an Al fraction of 0.005 up to a limit of ~ 130 THz for an AlAs emitter. The lower limit is due to the Al fraction at which the Al starts to act as an isoelectronic dopant and does not produce a consistent change in the VB. While an Al fraction of zero is possible, that would correspond to the HIWIP case which had the threshold frequency limitation. The second type of design uses doped AlGaAs as the emitter, and undoped GaAs as the barrier as shown in **Figure 13(b)**. In this approach the band offset from the Al fraction is used to reduce the band offset from the doping in the emitter. In this approach, the Al fraction must be kept small ($x < 0.17$) such that the band offset does not exceed the doping offset. In theory, this approach will allow the workfunction to be reduced down to zero.

2.9.1 p-GaAs emitter/AlGaAs barrier HEIWIP detectors

Results were reported (Perera et al., 2001) on a device structure consisting of 20 periods of 158 Å GaAs wells and 800 Å $Al_{0.02}Ga_{0.98}As$ barriers. The wells were doped with Be to 3×10^{18} cm^{-3}. The response increased as the bias was increased up to ~ 200 mV after which it remained relatively constant. Strong response was reported for frequencies higher than 6 THz with a threshold frequency of 4.3 THz. The peak responsivity was ~ 6 Å W^{-1} at a frequency of 9.23 THz. The specific detectivity (D*) was $\sim 2 \times 10^{13}$ cm$\sqrt{Hz}$W^{-1} (Jones), with a Noise Equivalent Power (NEP) of 1.4×10^{-15} W$\sqrt{Hz}^{-1}$ (Perera et al., 2001).

Device structures with different Al fractions from 0.005 to 0.02 showing variations in the threshold from 3.6 to 4.6 THz (92–68 μm) have been reported (Matsik et al., 2003). The Al fraction was varied, with x=0.02, 0.01 and 0.005 for samples 2409, 2410, and 2411 respectively, to adjust f_t, with the expected barrier heights of 18, 13.5 and 11.2 meV, respectively. The responsivity results for the three samples at a bias field of 3.5 kV cm^{-1} for 4.2 K are shown in **Figure 14** with a strong response for frequencies higher than 6 THz. The inset shows the raw response normalized so that the response was 1 at the frequency where the signal equaled the noise determined from the deviation of multiple measurements. The threshold values (indicated by the arrows) were $f_t = 4.6 \pm 0.1$, 3.9 ± 0.1, and 3.6 ± 0.1 THz (65, 84, and 92 μm) for samples 2409, 2410 and 2411 respectively. The responsivity at 10 THz (30 μm) was ~ 5.6 Å W^{-1} for samples 2409 and 2410 Ånd 6.0 Å W^{-1} for 2411. The quantum efficiency was 22% for 2409 and 2410 and 25% for 2411 at 10 THz (30 μm). The D* was 4×10^{10} Jones (cm$\sqrt{Hz}$ W^{-1}) for 2409 and 2410 and 3.6×10^{10} Jones for 2411 at 4.2 K (Matsik et al., 2003).

2.9.2 p-AlGaAs emitter/GaAs barrier HEIWIP detectors

As discussed previously, p-type HEIWIP detectors have a threshold frequency limit due to the limit on Al fraction. One approach to overcome this difficulty is to use AlGaAs emitters with a low aluminum fraction. Absorption measurements have been performed on doped AlGaAs films giving good agreement with the model for the absorption coefficient (Rinzan et al., 2004) as seen in **Figure 15(a)**. The model was the same as for the GaAs absorption with the material parameters obtained by a linear interpolation of the values for GaAs and AlAs. Based on these results, detectors using AlGaAs emitters were designed and results have been reported
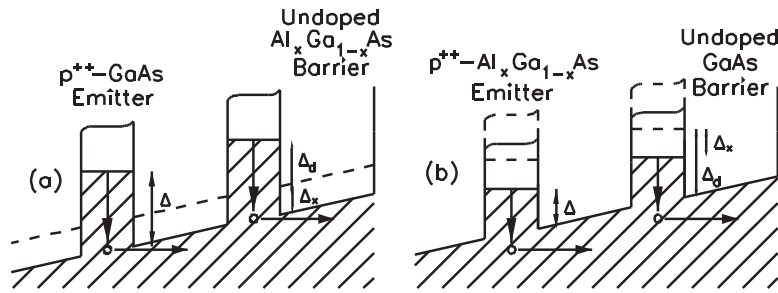
Figure 13   The band diagram for a HEIWIP detector using doped GaAs emitters, and undoped AlGaAs barriers. The contributions from both the doping and the Al fraction will increase the workfunction. (b) The band diagram for a HEIWIP detector using doped AlGaAs emitters, and undoped GaAs barriers. Here the contribution from doping increases the work function while the contribution from the Al fraction decreases it.
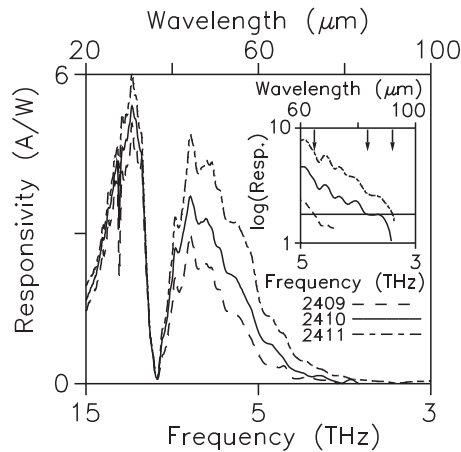

Figure 14   Experimental responsivity spectra for 2409, 2410 and 2411 at 3.5 kV cm^{-1} obtained at 4.2 K. The only difference in the samples was the Al fraction which was $x=0.02$, 0.01 and 0.005 for 2409, 2410 and 2411 respectively. The data shows a decrease in f_t with decreasing x. The sharp decrease near 8 THz is due to the reststrahlen effect. The inset shows a log plot of the raw response with all curves normalized to have the same noise level indicated by the horizontal line. The threshold (indicated by the arrows) variation, with $f_t=4.61$, 3.57, and 3.26 THz for samples 2409, 2410 and 2411 respectively can be clearly seen. Reused with permission from Matsik, S.G., 2003. Applied Physics Letters, 82, 139. Copyright 2003, American Institute of Physics.

(Rinzan et al., 2005b) on a sample consisting of 10 periods of 3×10^{18} cm^{-3} Be-doped 500 Å thick Al$_{0.005}$Ga$_{0.995}$As emitters and 2000 Å thick GaAs barriers sandwiched between two contacts.

The variation of Δ obtained from Arrhenius plots with the bias field for three devices with different electrical areas are shown in **Figure 15(b)**. The Δ decreased from ~ 17 meV at zero bias to 10.5 meV at 2 kV cm^{-1} (Rinzan et al., 2005b). The source of this decrease is yet to be explained. The variation of responsivity with the bias field at 4.8 K is shown in **Figure 16**. For frequencies >6 THz, the responsivity increases with the field with a maximum responsivity of 9 Å W^{-1} at 1.5 kV cm^{-1}. Although further increase in the field decreases the higher frequency response, the lower frequency (<6 THz) response increases. As expected, Δ_b decreases with the field, increasing the threshold to 2.3 THz for a bias field of 2.0 kV cm^{-1}. The semi-log scale of **Figure 16** clearly shows the variation of f_t with the applied field. A dark current limited peak detectivity of 1.5×10^{13} Jones, was obtained at the bias field of 1.5 kV cm^{-1} at 4.2 K. A BLIP temperature of 20 K for a 0.15 kV cm^{-1} bias field was recorded (Rinzan et al., 2005b).

2.9.3   n-GaAs emitter/AlGaAs barrier HEIWIP detectors

Most of the HIWIP and HEIWIP work has been carried out based on p-type materials. However, results have been recently reported (Weerasekara et al., 2007) on an n-type GaAs/AlGaAs HEIWIP device structure consisting of an undoped 1 μm thick Al$_x$Ga$_{1-x}$As ($x=0.04$) barrier layer sandwiched between two 1×10^{18} cm^{-3} Si doped GaAs contact layers. The 100 nm top contact and a 700 nm bottom contact layers serve as emitters in this design. The Δ was estimated to be 13–14 meV corresponding to a threshold frequency f_t of 3.1–3.4 THz from Arrhenius analysis (Weerasekara et al., 2007). The calculated Δ should be between ~ 10–20 meV, corresponding to a 2.4–5.0 THz (125–60 μm) threshold frequency.

The maximum peak response (R_{peak}) of 6.5 Å W^{-1} at 7.1 THz (42 μm) (Weerasekara et al., 2007) was seen at a bias field of 0.7 kV cm^{-1} in the forward bias operation (top emitter positive) as shown in **Figure 17(a)**. The R_{peak} obtained in the reversed bias was 1.7 Å W^{-1} at 0.25 kV cm^{-1}. At a bias field of 0.5 kV cm^{-1}, The R_{peak} in the forward bias was 6.1 Å W^{-1} while the R_{peak} in
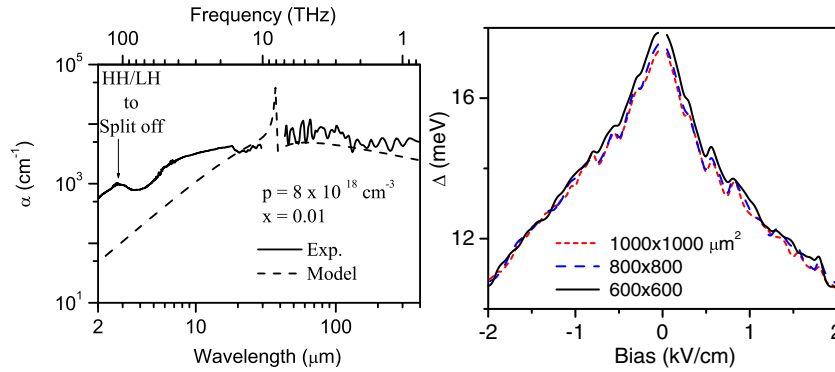
Figure 15 (a) The measured and calculated absorption coefficient for an $Al_{0.01}Ga_{0.99}As$ film with doping of 8×10^{18} cm^{-3}. For low Al fractions, the experimental results are in good agreement with the model developed for absorption in GaAs. Reused with permission from Rinzan, M.B.M., 2004. Applied Physics Letters, 85, 5236. Copyright 2004, American Institute of Physics. (b) Variation of workfunction, Δ with the bias field for three mesas with different electrical areas. The workfunction at different bias fields were obtained using Arrhenius plots. The zero bias workfunction is ~ 17 meV for all the mesas. Reused with permission from M. B. M. Rinzan, Applied Physics Letters, 86, 071112 (2005). Copyright 2005, American Institute of Physics.
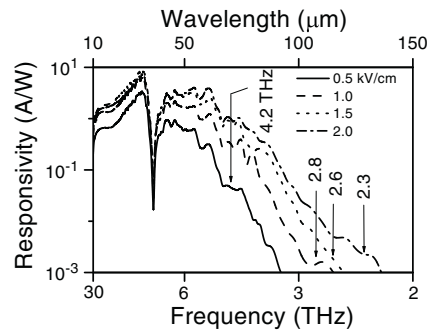

Figure 16 The variation of responsivity with applied field for p-AlGaAs/GaAs HEIWIP (sample V0207) at 4.8 K. The peak responsivity, 9 Å W^{-1} at 9.6 THz, was obtained at 1.5 kV cm^{-1}. The increase in response with the field around f_t is due to threshold shift with the bias. The sharp dip at ~ 8 THz is due to the interaction of radiation with GaAs-like TO phonons. The bias field decreases the effective work function pushing f_t towards 2 THz with the increasing field. Reused with permission from Rinzan, M.B.M., 2005. Applied Physics Letters, 86, 071112. Copyright 2005, American Institute of Physics.

reverse bias is 1.1 Å W^{-1}. The responsivity ratio in forward and reverse bias operations agrees with the thickness ratio of the bottom and the top contact layers (Weerasekara et al., 2007). Based on the spectral response, a threshold of 3.2 THz was observed. The variation of the responsivity values at 7.1 and 10.4 THz with bias are shown in **Figure 17(b)**. The R_{peak} under 0.7 kV cm^{-1} bias field decreases from 6.5 to 0.1 Å W^{-1} when the operating temperature increases from 6 to 25 K. The variation of the responsivity values at 7.1 and 10.4 THz with operating temperature is shown in **Figure 17(c)**.

The experimentally observed (symbols) and the calculated (lines) thresholds for p-GaAs/AlGaAs, p-AlGaAs/GaAs, and n-GaAs/AlGaAs HEIWIP detectors with different Al fractions are shown in **Figure 5**. The results for p-GaAs/AlGaAs HEIWIP detectors are based on samples 2409, 2410, and 2411 with $x = 0.02, 0.01, 0.005$; the p-GaAs/$Al_{0.12}Ga_{0.88}As$ HEIWIP detector reported by Matsik et al. (2004); and p-GaAs/$Al_xGa_{1-x}As$ HEIWIP detectors ($x = 0.28, 0.37$, and 0.57) reported by Jayaweera et al. (2008). The p-$Al_{0.005}Ga_{0.995}As$/GaAs detector reported by Rinzan et al. (2004) has shown the shortest frequency (highest wavelength) threshold. Experimental thresholds of most of the p-GaAs/AlGaAs detectors agree with the calculated values. As seen in the plot corresponding to n-GaAs emitter, the threshold of the n-GaAs/$Al_{0.04}Ga_{0.96}As$ HEI-WIP detector reported by Weerasekara et al. (2007) is also in good agreement with the theoretical calculation. However, the threshold obtained for an n-GaAs/$Al_{0.12}Ga_{0.88}As$ HEIWIP detector deviates from the calculated value. In any of the detectors considered for the comparison in **Figure 5**, the actual Al fraction after the growth of the structure in AlGaAs has not been reported, instead the designed Al fraction has been considered for the plot. Since a deviation in the Al fraction during the growth can occur, one of the possible reasons for the slight deviation in the threshold could be due to this difference.

2.9.4 n-GaN/AlGaN HEIWIP detectors
A GaN/AlGaN HEIWIP detector structure responding in the terahertz range has also been reported (Ariyawansa et al., 2006c), indicating the feasibility of terahertz detector development with the rapidly developing GaN/AlGaN material system. The detector
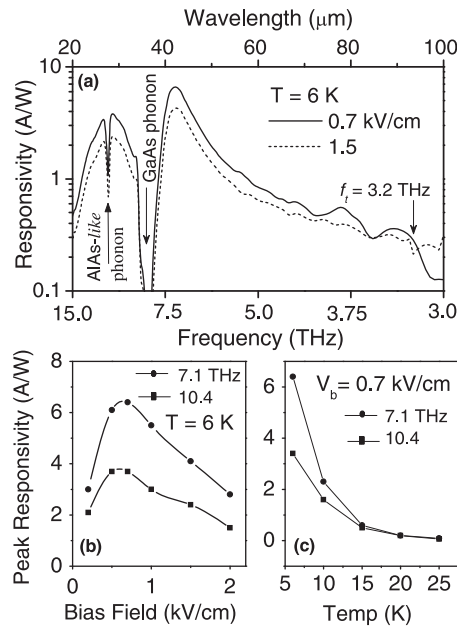
Figure 17   Responsivity variation of the n-GaAs/AlGaAs HEIWIP for 0.7 and 1.5 kV cm^{-1} is shown. The highest R_{peak} is 6.5 Å W^{-1} at 0.7 kV cm^{-1} at 6 K. The f_t is 3.2 THz. The f_t which is 3.2 THz was determined by the instrument noise level. The inset shows the device structure. Top and Bottom contacts are 100 and 700 nm thick n-doped GaAs respectively. The barrier is 1 μm thick undoped GaAs/Al$_{0.04}$Ga$_{0.96}$As. (b) Variation of R_{peaks} at 7.1 and 10.4 THz under different bias fields. (c) The R_{peak} variation with temperature at the bias field of 0.7 kV cm^{-1} and responsivity vanishes after 25 K. Reused with permission from Weerasekara, A., 2007. Optics Letters 32, 1335. Copyright 2007, Optical Society of America.

structure was grown by OMCVD on a sapphire substrate. The complete response of this detector at 5.3 K is shown in **Figure 18** with the response composed of three parts based on three detection mechanisms. The free carrier response exhibits a threshold at 27 THz (11 μm), while the sharp peak at 5.5 THz (54 μm) is due to the 1s–2p$\pm$ transition of silicon (Si) dopant atoms, which has been observed previously (Moore et al., 1997) with the same energy of $\sim$23 meV. In addition to the free carrier and impurity-related responses discussed above, there is also a slower mechanism which responds out to 300 μm (1 THz). This response was reported to be due to either a thermal or pyroelectric effect, however, the exact mechanism has not been confirmed yet. Further studies on the response mechanism will benefit the development of GaN-based terahertz detectors.

2.10   Tunable hot-carrier photodetectors for terahertz frequency operation

The spectral response of common optoelectronic photodetectors is restricted by a cutoff wavelength limit (λ_c) that is related to the activation energy (or band-gap) of the semiconductor structure (or material) (Δ) through the relationship: $\lambda_c = hc/\Delta$ (Sze, 1981). This spectral rule dominates device design and intrinsically limits the long wavelength response of a semiconductor photodetector. The typical operating principle of a heterojunction photodetector is photoexcitation of carriers in the absorber (or emitter), and their escape over the barrier by an internal photoemission process occurring at the emitter–barrier interface. The escape probability is characterized by an internal work function (Δ), which is defined as the energy difference between the Fermi level of the absorber and the band edge of the barrier. Modifying the energy distribution of carriers, for example by introducing hot-cold carrier interactions, can lead to a change in this threshold response.

By utilizing the hot-cold carrier energy transfer mechanism, p-type GaAs/AGaAs heterojunction detectors with $\Delta = 0.32$ eV (or 3.9 in wavelength) has shown a response up to 103 μm (Lao et al., 2014). As shown in **Figure 19(a)**, they consist of three p-type GaAs regions ($p = 1 \times 10^{19}$ cm^{-3}), i.e., an injector, absorber and collector, for which the VB alignment is schematically plotted in **Figure 19(b)** (equilibrium) and **Figure 19(c)** (negative bias). The injector provides a hot-hole reservoir upon photoexcitation. Holes surmounting the barrier are 'hot' because of their excess energies relative to the band edge of the absorber.

The photoresponse shown in **Figure 20(a)** was measured at 5.3 K. The most striking fact is that, a very long-wavelength infrared (VLWIR) response is seen up to 55 μm, whilst the conventional limit is only 3.9 μm (shaded region) according to the internal work function (i.e., Δ) of the absorber/constant barrier junction ($\Delta = 0.32$ eV). The agreement between λ_c and Δ in terms of $\lambda_c = hc/\Delta$ is typically found to be good in a variety of detectors, and has been used as a guideline to tune spectral response through varying Δ, and to determine band offsets (Lao et al., 2012) However, there is clearly no agreement for the observed VLWIR response in this case.
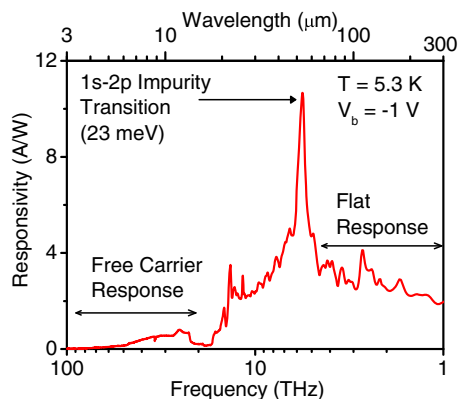
Figure 18 The response of the GaN/AlGaN HEIWIP detector at 5.3 K and -1 V bias. There are three response mechanisms, which can contribute to the photocurrent: free carrier response, impurity-related response, and a flat terahertz response.
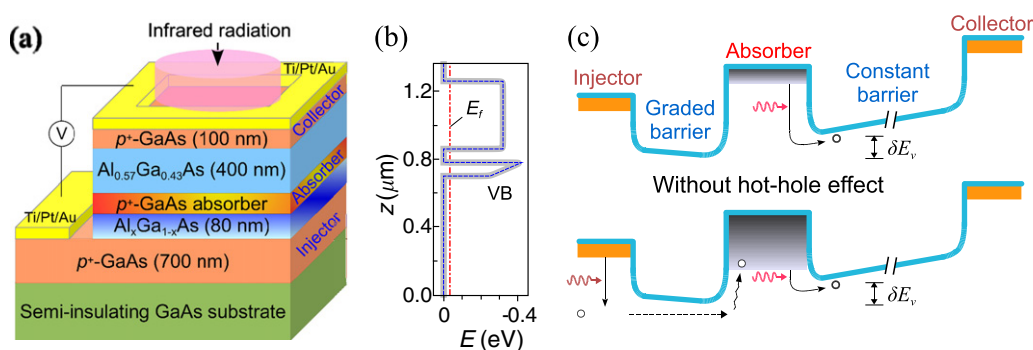

Figure 19 (a) Schematic diagram of the p-type GaAs/Al$_x$Ga$_{1-x}$As structures. (b) Calculated equilibrium valence-band alignment, with and without image-force barrier lowering (thick-gray and dashed-blue lines, respectively). (c) Schematic valence band diagrams (including band bending) under negative bias (positive polarity applied on the injector), with a comparison of hole photoexcitation and emission without (top) and with (bottom) the hot-cold hole energy transfer. After Lao *et al.* (2014).

In general the observed VLWIR response could be due to a bolometric effect, (Yan *et al.*, 2012) or an impurity-band/free-hole carrier based response. Possible optical transitions contributing to photon absorption by the p-type GaAs absorber in the infrared range include the impurity band-to-VB transition, and intra-/inter-VB transitions, both of which are free-carrier type effects. Increasing the doping concentration shifts the absorption peak and broadens the absorption width, as a result of enhanced carrier scatterings, and the shifting/increasing of the Fermi level/free-carrier plasma frequency, respectively. The absorber, though, has a major effect on the bolometric response and impurity-band absorption. By measuring a control sample (LH1002) which contains the same GaAs absorber as the samples SP1005–1007 (SP1005–1007 display a VLWIR response; see **Figure 20(b)**), we can exclude these two mechanisms as a cause of the VL-WIR response. LH1002 responds as expected, in accordance with the '$\lambda_c = hc/\Delta$' rule. Comparison of LH1002 (having a symmetric flat-barrier configuration) with SP1005–1007 (asymmetric band alignment) indicates that the VLWIR response is critically dependent on the structure details. Additionally, the bolometric response, proportional to the temperature variation of the absorber upon photon absorption and the corresponding resistance change, monotonically increases with increasing bias. This effect contrasts with the strongly non-monotonically bias-dependent VLWIR response, as shown in the calculated spectral weight (SW) (**Figure 21**), (**Schneider** *et al.*, **2007**) defined as

$$SW \propto \int_{\lambda_{\max}}^{\lambda_{\max}} \mathcal{R}(\lambda) d\lambda \qquad [8]$$

where $\mathcal{R}(\lambda)$ is the spectral responsivity. The VLWIR response reaches a maximum at about -0.1 V. For these reasons, a bolometric effect cannot be considered to be contributing to the VLWIR response. Also, the impurity-band to VB optical transition can barely have any influence on the response, as the impurity band is actually merged with the VB at $p = 1 \times 10^{19}$ cm^{-3}. Another possible doping-related effect is dopant-correlated potential fluctuations and the relevant tailing states at the band edge; however, absorbing photons with energies as high as the value Δ are required to excite holes in these band tailing states and allow them to escape over the barrier. Instead, here, we discuss a two-phase hot-hole mechanism to explain the VLWIR response: hot-cold hole energy transfer, and the response of high-energy cold holes to the VLWIR radiation. The dominant absorbing mechanism will then

be based on the intra-band free-hole absorption. It should be noted that the free-carrier based VLWIR response in this work differs markedly from the previous reported free-carrier response in which a small value of Δ is required.

The proposed mechanism for the hot-hole response implies a need for injecting hot holes to trigger the VLWIR response. This can be achieved through electrical and/or optical approaches. For the electrical approach, to obtain a non-trivial current passing through the graded barrier, a bias substantially higher than that at which hole distribution peaks are observed, is required. Under such a high bias, the VLWIR response is no longer present. An optimized solution is to separate the injection of hot holes and the collection of photoexcited holes by altering the device structure. Here, we show the optical approach; the advantage of this is that it gives a convenient control of the hot-hole injection through varying the optical intensity. **Figure 22(a)** shows a schematic diagram of the experimental apparatus. A cut-on wavelength (λ_{Co}) is selected, and a long-pass filter is used to block high-energy photons from the FTIR spectrometer from being incident onto the sample. **Figures 22(b)–22(d)** map the SW, which is measured using filters with different λ_{Co} (the GaAs beamsplitter and optical excitation source are not used in this case). Increasing λ_{Co} reduces the energies of the injected hot holes, thus reducing the VLWIR response. The use of $\lambda_{Co} = 4.5~\mu m$ (**Figure 22(d)**) fully suppresses the VLWIR response because of the absence of hot holes in the absorber. However, as shown in **Figure 22(e)**, the VLWIR response can be recovered by utilizing an optical excitation source which induces hot hole injection. These results are in good agreement with the hot-cold hole energy transfer mechanism.

The responsivity of our samples is of the order of 10 Å W^{-1}, which is relatively low compared to reported detectors. The use of a single-emitter structure with relatively low absorption is one of the reasons. Also, the bulk semiconductor based absorber leads to a fast carrier lifetime (e.g., ~ 0.1 ps for $p = 1 \times 10^{19}$ cm^{-3}). By using structures such as QDs, an increase in the lifetime by a factor of 10^4–10^8 is possible. Despite the low responsivity, an advantage of our results is the negligible dark current owing to the high activation energy (0.32 eV), even though a VLWIR response is obtained. This offers the possibility of incorporating a long-wavelength response into a short-wavelength detector. In fact, the noise current is far below the experimental sensitivity ($\sim 10^{-15}$ Å/Hz$^{1/2}$). Using this limit, a conservative estimate of the specific detectivity is $\sim 1 \times 10^9$ cm Hz$^{1/2}$ W^{-1} (using the highest
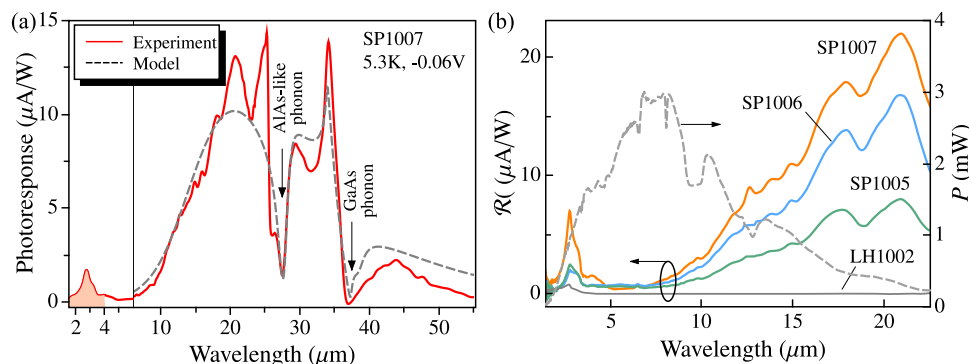
Figure 20 (a) Photoresponse at 5.3 K. The dashed line is the escape-cone model fit. The marked features are associated with GaAs and AlAs-like phonons. (b) Comparison of the response for samples SP1005–1007 and LH1002 at 5.3 K. The optical power spectrum of the FTIR spectrometer used in the experiment (incident on a sample with active area of $260 \times 260~\mu m^2$) is also shown. After reference Lao *et al.* (2014).
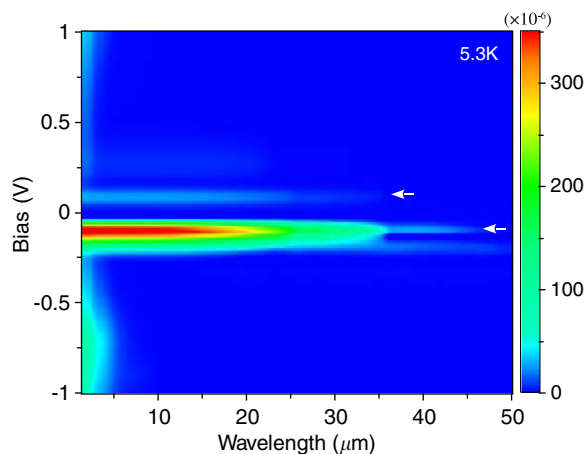
Figure 21 The variation of SW (sample SP1007) with bias and λ_{min}, calculated using eqn [8] where λ_{max} is 55 μm. After reference Lao *et al.* (2014).
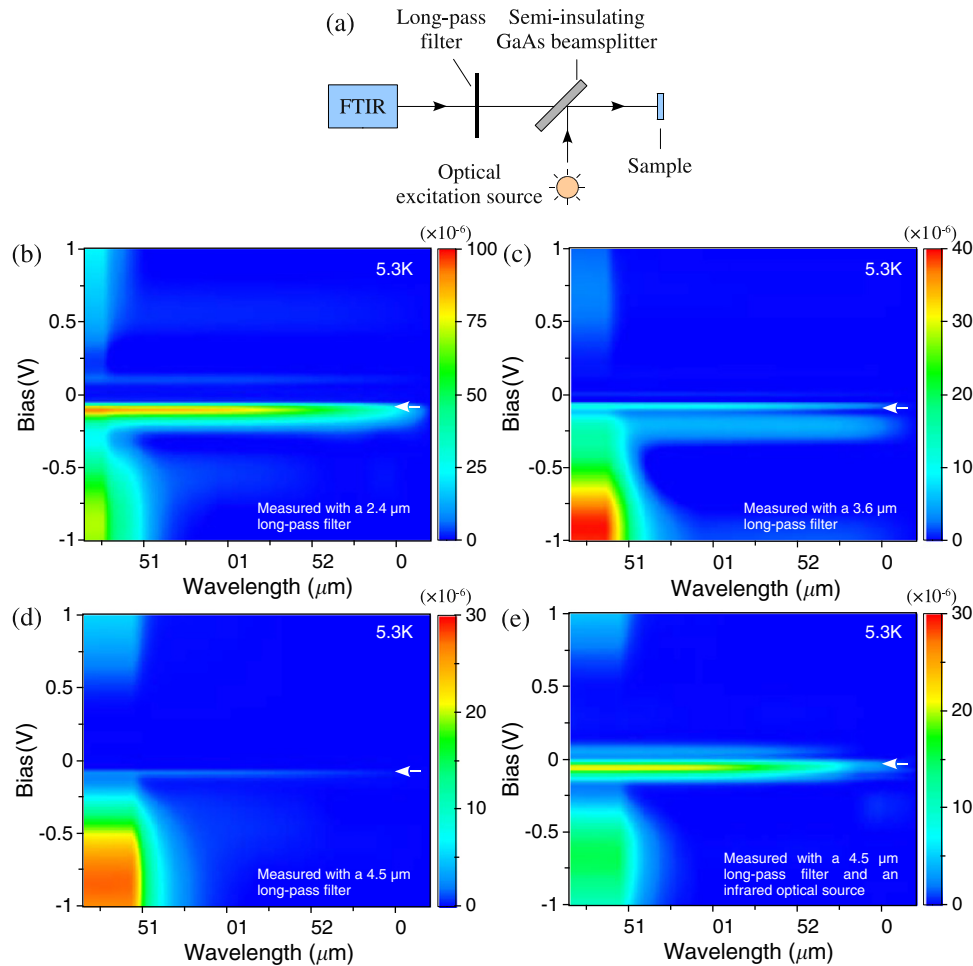
Figure 22   (a) Experimental apparatus, where the semi-insulating GaAs is double-side polished and acts as a beamsplitter. (b)–(d) Spectral weights (SW) of the response (sample SP1007) measured by using long-pass filters with cut-on wavelengths (λ_{CO}) of (b) 2.4 μm, (c) 3.6 μm and (d) 4.5 μm, respectively. The VLWIR response is gradualy diminished by increasing λ_{CO}, and is barely seen when a $\lambda_{CO} = 4.5$ μm filter is used. (e) Recovery of the VLWIR response by providing hot holes through an external optical excitation source, measured with a 4.5 μm long-pass filter. After reference Lao *et al.* (2014).

responsivity of up to 69 μm Åt h mA W^{-1}). In addition to the 5.3 K operation, we have measured the VLWIR response up to 30 K, showing the possibility of higher-temperature operation. Optimized quantum structures may lead to improvement in the responsivity as well as the operating temperature.

The finding of the hot-carrier effect opens up many possibilities for new applications based on traditional semiconductor technologies, for example, utilizing well established III–V semiconductor epitaxy and process technology. Normally, applications of semiconductors are confined to specific wavelength ranges in accordance with their band gaps. With the additional degree of freedom enabled by tuning the energies of cold carriers, it is now possible for a particular material to respond beyond its standard spectral limit. In addition to photodetection, the hot-carrier concept can be applied to photovoltaic devices, which, in addition to their original absorption band, will have wavelength-extended absorbing capabilities, with a tunability controlled through varying the degree of hot-hole injection in order to meet the demands of specific applications. Moreover, the hot-carrier effect is expected to improve energy efficiency of both photodetectors and photovoltaics, since the energies of hot carriers are diverted from heating the lattice to heating cold carriers.

2.11   Dualband Detectors

In both HIWIP and HEIWIP detectors, it has been reported (Ariyawansa *et al.*, 2005b) that interband transitions in the undoped barrier and intraband transitions within the emitter lead to dualband response characteristics. Incident radiation with an energy greater than the band gap of the barrier are absorbed, generating an electron–hole pair. The standard detection mechanism in HIWIPs and HEIWIPs including free carrier absorption's leads to the detection of terahertz radiation. Excited carriers are then collected by the applied electric field. The interband response threshold is determined by the band gap of the barrier material.
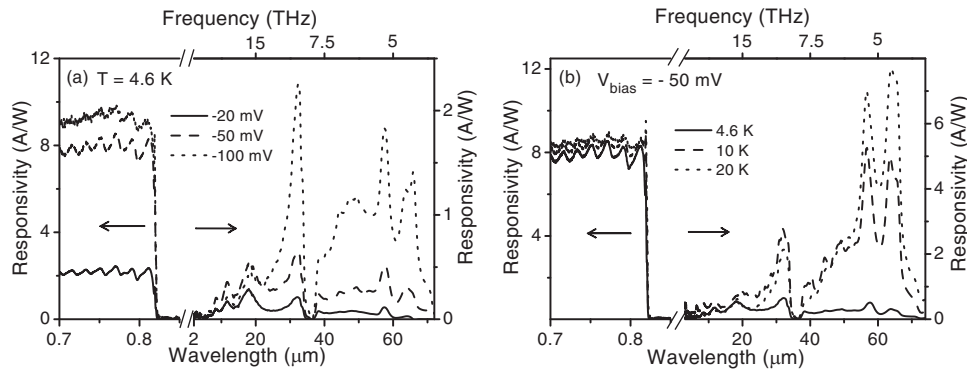
Figure 23   The interband and intraband response at 4.6 K under different reverse bias values. (b) Shows both interband and intraband response at different temperatures under -50 mV bias. The left and right axes are corresponding to NIR and FIR responsivity respectively and a break on the frequency axis at 39 THz has been made in order to expand the view in both regions. Reused with permission from Ariyawansa, G., 2005. Applied Physics Letters, 86, 143510. Copyright 2005, American Institute of Physics.

Hence, using different material systems (such as Si, GaAs/AlGaAs, GaN/AlGaN, etc.), the interband response can be tailored to different wavelength regions.

2.11.1   NIR-THz dualband HIWIP detectors

A NIR-THz dualband detector based on a p-GaAs HIWIP detector has been reported (Ariyawansa et al., 2005b). The structure consisted of a bottom contact (p^{++}) layer with 1.0 μm thickness, a barrier layer with 1.0 thickness, an emitter (p^+) layer with 0.2 μm thickness, and a top contact layer. The spectral response for different bias voltages in both NIR and THz regions at 4.6 K is given in **Figure 23(a)**. The optimum responsivity at 0.8 is ~ 9 Å W^{-1} while the detectivity is $\sim 2.7 \times 10^{11}$ Jones under 100 mV reverse bias at 4.6 K. The response due to intraband transition is observed up to 4.3 THz with a responsivity of ~ 1.8 Å W^{-1} and a specific detectivity of $\sim 5.6 \times 10^{10}$ Jones at 5.26 THz (57 μm) under 100 mV reverse bias. The sharp drop around 37 μm was assigned to the strong absorption around the reststrahlen band of GaAs and the peaks at 57 and 63 μm were assigned to transitions of impurity atoms in the barrier region (Esaev et al., 2004b). The spectral responsivity curves due to both interband and intraband transitions for temperatures from 4.6 K to 20 K are shown in **Figure 23(b)**. An optimum responsivity of ~ 8 Å W^{-1} and a detectivity of $\sim 6 \times 10^9$ Jones were obtained at 0.8 μm for interband response, while a responsivity of ~ 7 Å W^{-1} and a detectivity of $\sim 5 \times 10^9$ Jones were reported at 5.26 THz (57 μm), under 100 mV reverse bias at 20 K (Ariyawansa et al., 2005b).

Following the same principle a second detector operating in both the NIR and THz ranges has been reported based on a p-type Si HIWIP detector (Ariyawansa et al., 2006b). The NIR response at -1 V bias had a threshold of ~ 1.05 μm, agreeing with the ~ 1.17 eV bandgap of Si at 4.6 K. A NIR responsivity of 0.024 Å W^{-1} was obtained at 0.8 μm with a detectivity of $\sim 1.7 \times 10^9$ Jones at 0.8 μm under -1 V bias at 4.6 K. The THz response is in the range of 8.6–60 THz. A responsivity of 157 Å W^{-1} at 12 THz at -2 V bias was reported, which translates to an efficiency-gain product of 7.8.

2.11.2   UV-THz dualband HEIWIP detectors

Recently, a nitride based dualband detector was also demonstrated which showed response in both the UV and THz ranges (Ariyawansa et al., 2006a; Perera, 2007) similar to the previous NIR-THz detectors. This detector used interband absorption to detect the UV radiation and intraband absorption to detect the IR radiation. The GaAs was replaced by GaN and the AlGaAs replaced by AlGaN. While the initial detector using only two contacts required separate modulations to distinguish the UV from the IR, a later design using three contacts and separate active regions for the UV and the IR were able to distinguish UV from IR without separate modulations (Jayasinghe et al., 2008). This approach allows tremendous variations in the thresholds. By using AlGaN in both Layers with different Al fractions and adjusting the Al fraction in the barriers, the UV threshold can be tailored, while by adjusting the difference between the fractions in the emitters and barriers, the IR threshold can be tailored. However, for high performance devices, the quality of the GaN/AlGaN material system needs to be improved, which is presently the focus of many researchers.

3   Terahertz Quantum Well Detectors (QWIPs)

Quantum well (QW) structures have been studied for more than two decades with the aim to develop various optoelectronic devices. A QW structure can be considered as a 1D quantum mechanical system. The ability to tune the optical properties, primarily by changing the width of the quantum well, has led to the development of quantum well structures for various applications. Additionally, the barrier height and doping concentration are two parameters that can be easily changed. Various

combinations of these parameters (well width, doping concentration, and barrier height) and phenomena such as resonant tunneling, cascade, and mini-band structures make these systems highly adaptable. QWIPs were one of the most developed QW structures. Since the initial work (Coon and Karunasiri, 1984; Coon et al., 1986) began, there has been a tremendous amount of work reported for QWIPs (Levine et al., 1987; Levine, 1993; Choi, 1997; Liu and Capasso, 2000a) operating in mid infrared (MIR) (Li et al., 2005) and very long wavelength infrared (VLWIR) regions (Gunapala et al., 1994; Perera et al., 1998b, 2000) and QWIP focal plane arrays (FPAs) (Liu and Capasso, 2000b; Gunapala et al., 2003, 2007b; Jhabvala et al., 2004; Rogalski, 2004).

The feasibility for terahertz QWIPs has been reported theoretically (Etteh and Harrison, 2002; Ryzhii and Khmyrova, 2002; Ting et al., 2007; Feng et al., 2008) and several experimental (Liu et al., 2004; Luo et al., 2005; Graf et al., 2004; Patrashin and Hosako, 2008) demonstrations were also reported in the literature. While the majority of the research on QWIPs focused on the 3–5 and 8–14 μm range, a QWIP with a 20 THz (15 μm) threshold was reported (Bandara et al., 1992) in 1992. In 1998 the threshold was extended to 10.7 THz (28 μm) (Perera et al., 1998b) and 9.37 THz (32 μm) (Perera et al., 2000). Most recently, the response has been extended (Liu et al., 2004; Luo et al., 2005; Graf et al., 2004) further to 3.2 THz (94 μm). Most recently, further progress in terahertz QWIP development has been reported (Cao and Liu, 2011; Jia et al., 2014; Zhang et al., 2011; Guo et al., 2013; Zhou et al., 2012; Gu et al., 2014) by a group of researchers, covering multiple areas related to terahertz QWIP such as detector design, simulations, fabrication, experimental demonstration, grating couplers, etc. The most widely used material system for QWIPs is GaAs/AlGaAs, while other material systems such as InGaAs/GaAs, GaN/AlGaN (Beeler et al., 2014), etc are also potentially useful. Technically, increasing the well width pushes the operating wavelength of the QWIP into the terahertz region. However, the very small energy involved in the terahertz transition becomes a domain for various thermal mechanisms. In order to overcome these difficulties and improve the performance, new materials, device concepts, and phenomena need to be explored. In a recent publication, Guo et al. (2009) reported that it is important to consider the many many-body effects when terahertz QWIP detectors are designed. Here, a brief description is provided for several terahertz QWIP approaches reported recently in the literature (Liu et al., 2004; Luo et al., 2005; Graf et al., 2004; Patrashin and Hosako, 2008).

3.1 Intersubband Terahertz Quantum Well Detectors

A terahertz QWIP with a peak response at 7 THz has been reported by Liu et al. (2004). This article by Liu et al. addresses the problems associated with the reported detector, possible causes as well as the issues to overcome in order to improve the performance of terahertz detectors. In general, QWIPs are designed (Liu and Capasso, 2000a) so that the excited state overlaps with the continuum. For terahertz detectors, the energy spacing between the two states involved in the transition should fall in the energy range of 1.4–41 meV (10–1 THz). To satisfy these two conditions (matching the excited state with the continuum and having the energy spacing between the states in the terahertz region), both the well width and the barrier height should be changed. Based on the calculation carried out by Liu et al. (2004) detection at 1 THz is possible with a GaAs/$Al_{0.008}Ga_{0.99}$2As QW structure having a well width of 30 nm. However, this is a stringent requirement even for well developed and sophisticated growth techniques such as molecular beam epitaxy (MBE), especially because of the low Al fraction of 0.008. As shown in **Figure 24**, GaAs/AlGaAs QWIPs can be designed to exhibit peaks in the 8 to 1 THz range by adjusting the well width (from 11 to 30 nm) and the Al fraction in the AlGaAs barrier (from 0.54 to 0.008). While this calculation proves the feasibility in terms of bandgap-engineering, the expected performance, particularly the operating temperature under background limited conditions, needs to be addressed for each different application. According to theoretical calculations Liu et al. (2004), the predicted BLIP temperature for 10 and 1 THz QWIPs was expected to be 15–25 K and $\sim$2 K, respectively.

The terahertz QWIP detector reported by Liu et al. (2004) consists of 50 periods of GaAs/$Al_{0.05}Ga_{0.95}$As quantum wells with 12 nm GaAs wells and 40 nm $Al_{0.05}Ga_{0.95}$As barriers. A 10 nm region in the center of each well was doped with Si to a level of 10^{17} cm^{-3}. Two doped GaAs layers (10^{17} cm^{-3}) with a thickness of $\sim$400 nm and $\sim$700 nm were used as top and bottom contacts, respectively. The measured spectral response of the detector under 45°-illumination at 8 K and 0.4 V bias is shown in **Figure 25**. Theoretical predictions shown in **Figure 24** agreed well with the experimentally observed peak at 7 THz (42 μm). The dip around 8–9 THz (34–36 μm) was assigned to the optical phonon absorption in GaAs. Using the equation $R=(e/h\nu)\eta g$, where R is the responsivity, η is the absorption efficiency, and g is the photoconductive gain, a value for g was calculated using a value for R at 7 THz and η of $\sim$0.5%. This value for g is similar to that of QWIPs responding in other wavelength regions. Hence, it can be concluded that the capture probability and excited carrier lifetime for the terahertz QWIP and regular QWIPs are similar.

Another observation in this work by Liu et al. (2004) is the limitation of the operating temperature for the reported detector. The calculated and experimental dark current variation with the bias at different temperatures is shown in **Figure 26**. Similar to the variation of the responsivity with bias at 5, 10, and 15 K, the dark current remains the same at temperatures below 15 K, hence only 15 K dark current is shown in the figure. This dark current behavior (not reducing with the temperature) resulted in a lower BLIP temperature than the expected BLIP of $\sim$15 K, as seen in **Figure 24**. While the exact cause of the dark current behavior has not been confirmed by Liu et al., it was assumed that this dark current limitation could be due to inter-well tunneling of carriers. In order to confirm the cause of this dark current as inter-well tunneling, a similar set of terahertz QWIPs (Luo et al., 2005) were grown with different well widths and thicker barriers compared to the previous QWIP reported by Liu et al. (2004). This study confirmed the inter-well tunneling concept and lead to background limited terahertz QWIPs.
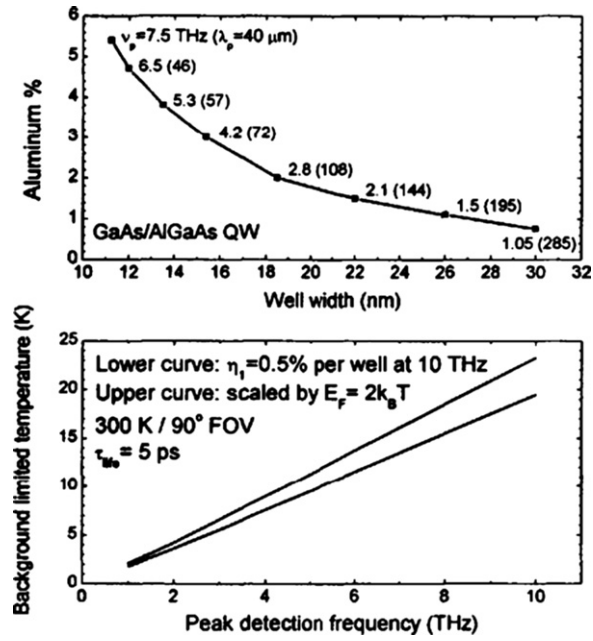
Figure 24   (Top) Calculated well width (L_w) and aluminum fraction (x) in the barrier for optimized GaAs/Al$_x$Ga$_{1-x}$As quantum well detectors responding at different wavelengths. (Bottom) Variation of calculated BLIP temperature with peak detection frequency. The background temperature is 300 K and the field-of-view full cone angle is 90°. Reused with permission from Liu, H.C., 2004. Applied Physics Letters, 84, 4068. Copyright 2004, American Institute of Physics.

Figure 25   Spectral response of a terahertz QWIP reported by Liu *et al.* (2004). The dip in the 33 to 37 meV range is due to optical phonon absorption. Reused with permission from Liu, H.C., 2004. Applied Physics Letters, 84, 4068. Copyright 2004, American Institute of Physics.

Figure 26   Dark current characteristics at various temperatures. The measured dark current becomes practically unchanged for temperatures of 15 K and lower. Reused with permission from H. Liu, C., 2004. Applied Physics Letters, 84, 4068. Copyright 2004, American Institute of Physics.

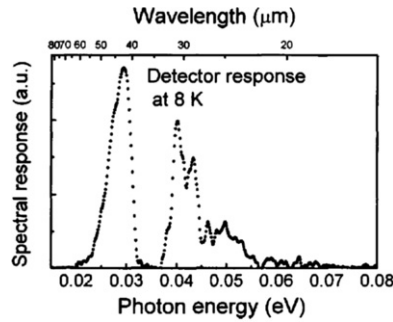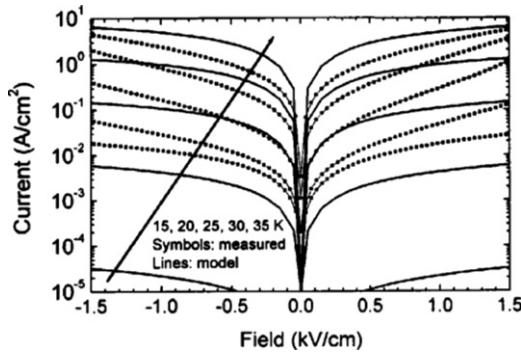**Table 3** Structure parameters for the THz QWIPs (Luo *et al.*, 2005).

Sample	L_w (nm)	L_b (nm)	[Al] (%)	N_d (cm^{-3})	N	f_{calc} (THz)	f_{exp} (THz)	BLIP(K)
V265	11.9	55.2	5	1×10^{17}	40	7.0	9.7	17
V266	15.5	70.2	3	6×10^{16}	30	4.2	5.4	13
V267	22.1	95.1	1.5	3×10^{16}	23	2.2	3.2	12

L_w is the well width, L_b is the barrier width, [Al] is the barrier aluminum fraction, N_d is the doping value in the center 10 nm of each QW, N is the number of QWs; and f_{calc} is the calculated peak frequency corresponding to intersubband transition energy. The GaAs/AlGaAs MQWs are sandwiched between 400 nm top and 800 nm bottom GaAs contact layers doped with Si to 10^{17} cm^{-3}. The experimentally observed peak frequency (f_{exp}) and the BLIP temperatures are also given. Reused with permission from H. Luo, Applied Physics Letters, 86, 231103 (2005). Copyright 2005, American Institute of Physics.
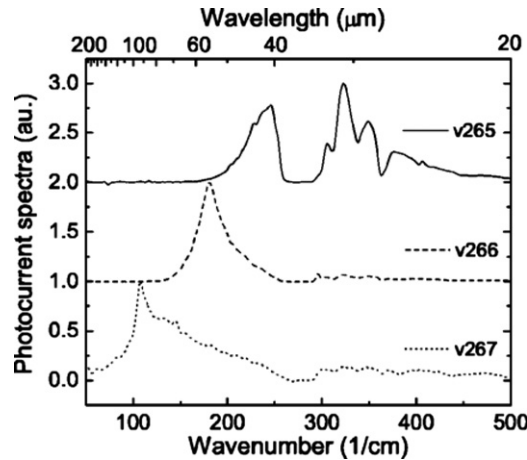

Figure 27 Normalized responsivity of the terahertz QWIP reported by Luo *et al.*, (2005) at 8 K. The solid, dashed, and dotted curves correspond to sample V265, V266, and V267, respectively. Sample V265, V266, and V267 were biased at 0.8, 0.15, and 0.03 V and showed peak responses at 9.7 THz (31 µm), 5.4 THz (56 µm), and 3.2 THz (93 µm), respectively. The curves were offset for clarity. Reused with permission from Luo, H., 2005, Applied Physics Letters, 86, 231103. Copyright 2005, American Institute of Physics.

All three samples in the set consist of multiple periods of GaAs/Al$_x$Ga$_{1-x}$As quantum wells with layer parameters given in **Table 3**. The number of periods, N, were determined based on the total epilayer thickness (around 3.5 µm). The well widths (L_w) are 11.9, 15.9, and 22.1 nm for the samples v265, v266, and v267, respectively, and have Al fractions (x) of 5, 3, and 1.5% in the Al$_x$Ga$_{1-x}$As barrier, respectively. The barrier thickness (L_b) has been designed to reduce the inter-well tunneling and the L_b of v265, v266, and v267 are 52.2, 70.2, and 95.1 nm, respectively. The 10 nm region in the center of each well was doped with Si. Two doped GaAs layers (10^{17} cm^{-3}) with a thickness of ~400 and ~700 nm were used as top and bottom contacts, respectively.

According to the prediction in **Figure 24**, the expected peak positions for the v265, v266, and v267 samples should be 7.0, 4.2, and 2.2 THz. Feng *et al.* (2008) have reported a photocurrent model for terahertz QWIPs and simulated responsivity spectra for the v265, v266, and v267 samples with peak responsivity values consistent with **Figure 24**. However, as shown in **Figure 27**, the measured values were at 9.7 THz (322 cm^{-1}, 31 µm), 5.4 THz (180 cm^{-1}, 56 µm), and 3.2 THz (108 cm^{-1}, 93 µm) with BLIP temperatures of 17, 13, and 12 K for samples v265, v266, and v267, respectively. The broad spectra seen for all samples confirm bound-to-continuum carrier transitions. The observed peak positions do not exactly match with the calculated values and the cause for the deviation possibly could be associated with the change in structure parameters during growth. The variation of the responsivity with applied bias at different temperatures is shown in **Figure 28**. All three samples show a similar variation, which is typical for a QWIP operating on bound-to-continuum transitions. Another important achievement is that these samples exhibit BLIP operation. The measured (dash line) and calculated dark current curves at different temperatures are shown in **Figure 29**. As expected, higher operating wavelength (lower frequency) detectors show higher dark current, limiting the applied bias for long wavelength detectors. For all the samples, a typical dark current variation with the temperature around the BLIP temperature was observed. The BLIP operation was achieved by preventing inter-well tunneling using thick barriers.

Patrashin and Hosako (2008) have recently demonstrated a 3 THz (100 µm) QWIP with a responsivity of 13 mA W^{-1} under a bias of 40 mV at 3 K. This QW structure consisted of 20 periods of 18 nm *n*-GaAs quantum wells in 80 nm Al$_{0.02}$Ga$_{0.08}$As barriers. Two doped GaAs layers with thicknesses of 0.4 and 0.8 µm were used as top- and bottom-contact layers. Terahertz detection in this structure is based on intersubband transitions of electrons between the ground state (E_1) and the first excited state (E_2) which aligned with the top of the barrier. The doping concentration was determined to be 5.6×10^{16} cm^{-3} so that only the Fermi level
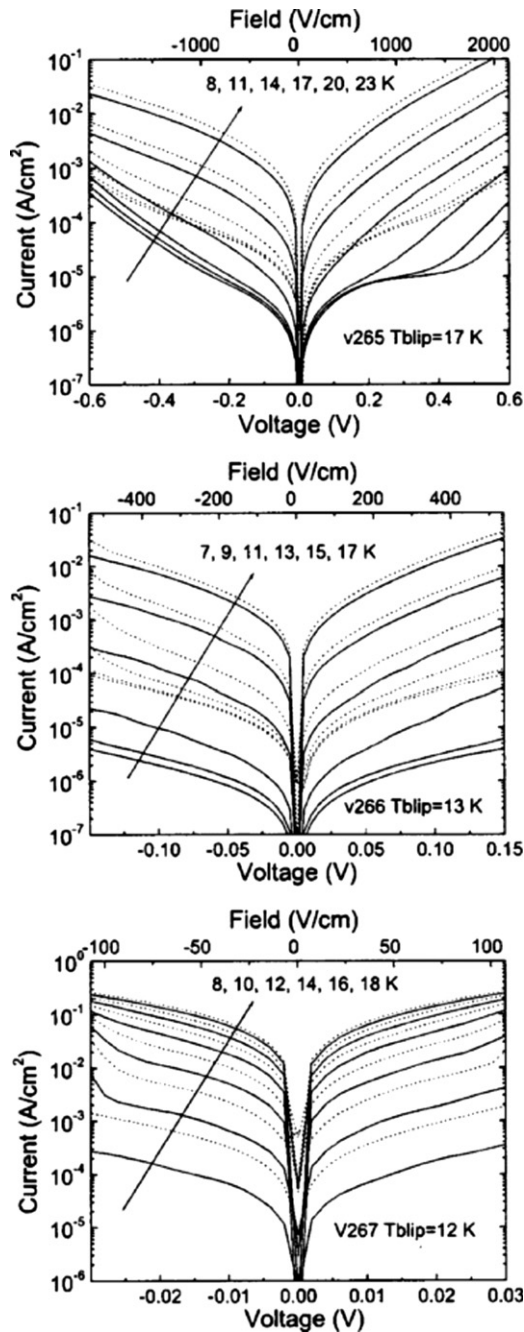
Figure 28 Variation of the calibrated responsivity of terahertz QWIPs (reported by Luo et al., (2005) with bias at different temperatures). Reused with permission from Luo, H., 2005. Applied Physics Letters, 86, 231103. Copyright 2005, American Institute of Physics.

was below the E_2 state. Based on the calculations (Patrashin and Hosako, 2008), the energy spacing between the E_1 and E_2 states is 11.1 meV (2.68 THz). As shown in **Figure 30**, the experimental response with a peak at 3 THz is in good agreement with the theoretical simulation.

Within past few years, significant progress in development of terahertz QWIPs including THz light coupling efficiency has been reported by a group of researchers (Cao and Liu, 2011; Jia et al., 2014; Zhang et al., 2011, 2014; Guo et al., 2013; Zhou et al., 2012; Gu et al., 2014). In a paper published in 2011, Zhang et al. (2011) have reported three GaAs/AlGaAs QWIPs with 1D metal gratings fabricated on top of the detector structures. These detectors are operated under front-side-illumination configuration. For the three detector structures labeled as V266, V267, and V458; the well-width is 155, 221, and 195 Å; barrier thickness is 702, 951, and 830 Å; number of periods is 30, 23, and 32; Al fraction is 3, 1.5, and 2%; and doping concentration is 6×10^{16}, 3×10^{16}, and 1.5×10^{17}, respectively. They are designed to respond at 3.8, 1.9, and 3.8 THz, respectively. Also, the 1D gratings coupled with
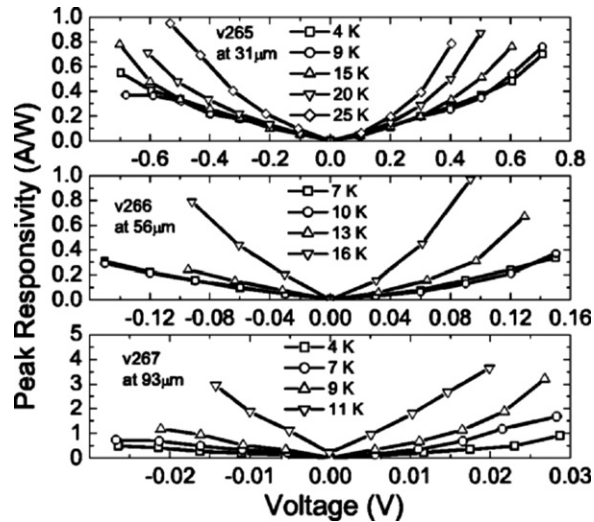
Figure 29 Current–voltage characteristics at different temperatures under dark condition (solid) and under a 90° FOV 300 K background (dashed). Reused with permission from Luo, H., 2005. Applied Physics Letters, 86, 231103. Copyright 2005, American Institute of Physics.
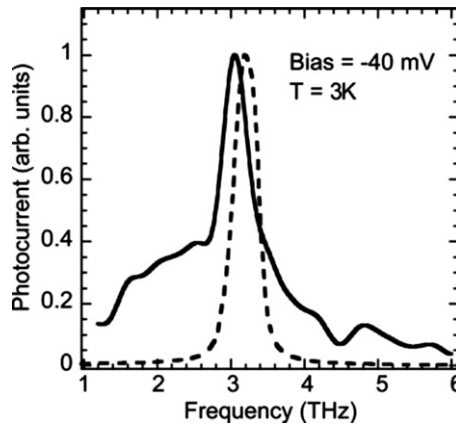

Figure 30 Normalized responsivity (solid curve) of the terahertz QWIP reported by Patrashin and Hosako, (2008) compared with the results of numerical simulations. Reused with permission from Patrashin, M., 2008. Optics Letters 33, 168. Copyright 2008, American Institute of Physics.

V266, V267, and V458 have a period of 20, 33, and 20 μm, respectively, and a fill-factor of 50%. As reported by Zhang *et al.* (2011) photocurrent spectra have been measured for two sets of detectors, one with 45°-facet without gratings and the other set with gratings. The photoresponse for grating-coupled detectors have been measured under front-side normal incidence geometry. A comparison between the two sets of spectra, also indicating the experimental photoresponse peaks for each structure, is shown in **Figure 31**. A promising observation is that the two sets of spectra measured under two geometries (45°-facet and grating-coupled) have pretty much the same spectral shape. That indicates that gratings effectively couple THz light without spectrally limiting the photoresponse. The peaks observed at 5.4, 3.2, and 5.5 THz for V266, V267, and V458, respectively, are longer than the designed values (3.8, 1.9, and 3.8 THz) and the broader response of V458 is reported to be due to higher doping.

The second part of the paper discusses an analysis on grating designs for THz light coupling and to optimize the grating period to the experimentally observed response peaks. The structure V266 is used to test two more grating designs, which have periods of 12 and 15 μm. These detectors are labeled as V266-G12 and V266-G15, respectively. As Zhang *et al.* (2011) have reported, the numerical calculations predict the best grating for the V266 structure to have a period of 14.6 μm, while a grating with a period of 15 μm is best for 5.28 THz which is close enough to detector's peak. The other grating, having a period of period of 12 μm, is best for 6.27 THz. In **Figure 32(a)**, the experimental spectral response for V266-G12 and V266-G15 is compared against that of the detector with a 45°-facet. Vertical lines indicate the frequencies at which the gratings were designed to work. No significant distortion observed, other than the expected minor red-shift for V266-G15, while the 12 μm grating caused the shoulder appearing near 6.2 THz on the spectrum for V266-G12. The other important merit is the coupling efficiency, which is quantified using the responsivity. As shown in **Figure 32(b)**, the maximum responsivity is observed for the detector with 15 μm grating. With respect to
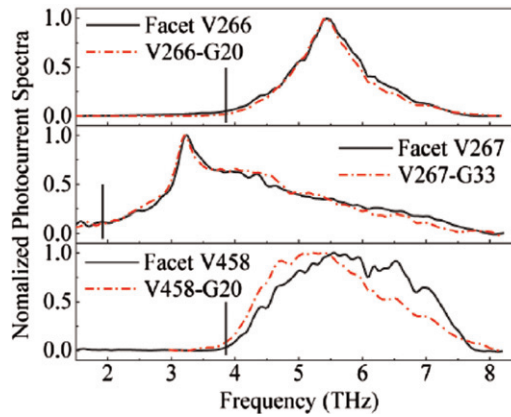
Figure 31   Normalized photoresponse spectra of the three QWIP detectors measured at 8 K, reported by Zhang *et al.* (2011). The solid lines represent the spectra measured for detectors without gratings but with 45-facet, while the dashed lines represent the spectra for grating coupled detectors measured under front-side normal incidence geometry. The vertical lines indicate the peak values expected by design for detectors and gratings. After Reference Zhang *et al.* (2011).
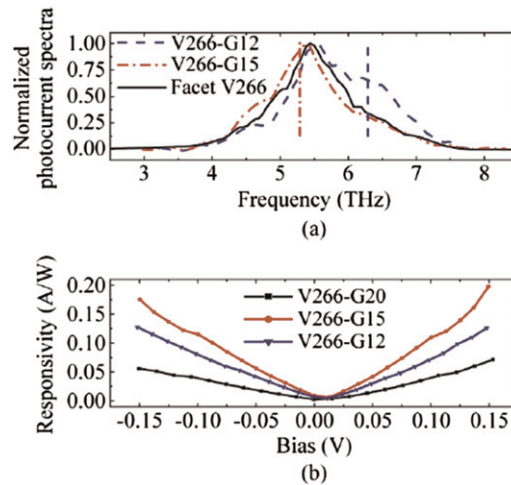

Figure 32   (a) Comparison of the normalized spectral response for the QWIP detectors with two grating structures (period of 12 and 15 μm). Vertical lines indicate the frequencies at which the gratings were designed to work. (b) Responsivity variation with bias for all three grating-coupled QWIP detectors. After Reference Zhang *et al.* (2011).

the responsivity of V266-G20 (with a 20 grating), an improvement factor of 1.83 and 2.81 at a bias of 0.15 V can be observed from the results shown in **Figure 32(b)**. As reported by Zhang *et al.* (2011) these improvement factors are fairly close to values predicted numerically, 1.58 and 3.27, respectively. The authors also report that the responsivity of the best detector (V266-15G) at 0.15 V is 0.197 Å W^{-1} and it is factor of 2.17 less than that of the detector with a 45°-facet. Moreover, this QWIP has a detectivity greater than 10^{11} cm Hz$^{1/2}$ W^{-1} at 4.2 K.

In a more recent publication, (Zhang *et al.*, 2014) the same authors have reported more efficient coupling of THz light using 1D reflection grating. It is a direct extension of their previous work discussed before. The same detector structure, V266, has been used with the reflection grating fabricated on top of the structure. In that case, the illumination is through the back-side of the structure (GaAs substrate). Fabrication of the reflection-grating has been done by growing an extra layer of 1.2 μm thick undoped GaAs layer, patterning it to a 1D grating pattern with 50% fill-factor, etching the open lines to a known depth, and deposition of a metal layer to cover the entire grating pattern. Through numerical modeling, the optimum grating period for 5.85 THz has been found to be 13.2 μm. Also, a strong dependence for the coupling efficiency on the grating height (defined by etch depth of the GaAs layer) has been theoretically reported, as shown in **Figure 33**. For the experimental verification, grating height of 1.2 μm has been chosen as the shape of the coupling efficiency spectrum and its peak fairly match with those of the QWIP detector (V266 structure). A direct comparison between the peak responsivity of the grating-coupled QWIP and the QWIP with a 45°-facet at 3.6 K is shown in **Figure 34**. Unlike the case discussed before (**Figure 32(b)**), where the grating-coupled detector had lower responsivity compared to the detector with a 45°-facet, about 22% increase in the responsivity has been reported for the QWIP coupled with a reflection
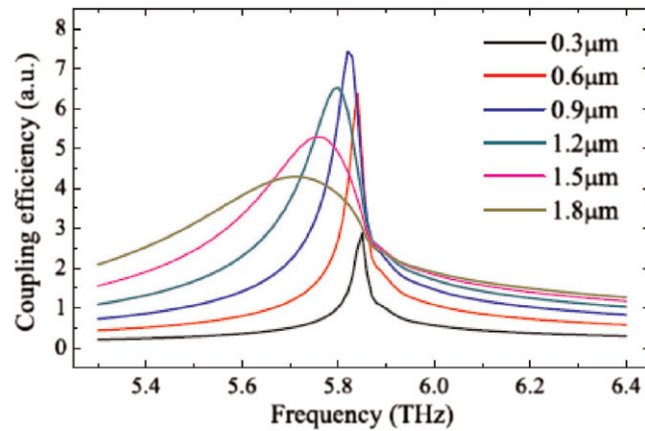
Figure 33 Calculated dependence of the THz coupling efficiency on the height of the stripes in a 1D reflection-grating. After Reference Zhang *et al.* (2014).
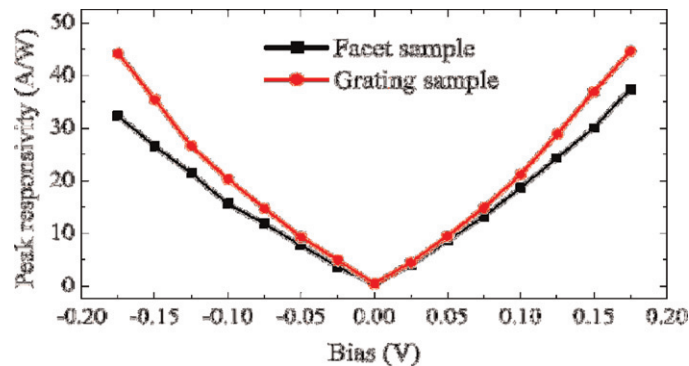

Figure 34 Variation of the responsivity (at 5.8 THz) with bias at 3.6 K for the QWIP (V266 structure) coupled with a reflection-grating compared with that of a QWIP fabricated from the same structure but with a 45°-facet. After Reference Zhang *et al.* (2014).

grating. This is a significant progress. A noise equivalent power of around 10 pW has also been reported for this detector. Authors have also mentioned that further improvement could be possible using triangular gratings and using dry etch process for grating fabrication.

3.2 Terahertz Quantum Well Intrasubband Photodetectors (QWISPs)

Quantum well intrasubband (inside a subband) photodetectors (QWISPs) in which intra-subband absorption lead to terahertz detection, were theoretically proposed by Ting *et al.* (2007) to overcome the low quantum efficiency of terahertz QWIPs. Since terahertz QWIP operation is based on intersubband (between subbands) transitions, the ground state should be very close to the top of the barrier. Hence, a low doping is used to keep the dark current as low as possible, which leads to low absorption and low quantum efficiency. In QWISPs, the intrasubband absorption mechanism and higher doping concentrations in the QW have shown a significant improvement in the performance. Three QWISP designs have been reported (Ting *et al.*, 2007) with peak responses for normal incidence light at 8.1, 5.2, and 2.75 THz (37, 58, and 109 μm).

A comparison between the CB profile and electronic transitions in QWIPs and QWISPs is shown in **Figure 35**. QWIPs use a wide well and lower barriers to satisfy the basic QWIP design requirements (Gunapala and Bandara, 1995), while QWISPs consist of a narrow well and high barriers where only the ground state falls inside the barriers. This modification of QWISPs allows higher doping concentrations in the well without increasing the dark current. Electrons photoexcited by terahertz radiation via intra-subband transitions escape into the continuum resulting in a photocurrent. However, QWISP mechanism does not conserve the momentum (or $k_\parallel$), hence an additional process is required to provide the change in momentum. Ting *et al.* (2007) have proven that the elastic scattering by dopants in the quantum well provides this momentum change for both intrasubband transitions and photoexcited carrier escape. In comparison with HEI-WIPs (Matsik *et al.*, 2004; Esaev *et al.*, 2004a; Weerasekara *et al.*, 2007), the detection mechanism in QWISPs involve 2D intrasubband absorption and a 2D–3D carrier excitation mechanism, while HEIWIPs involve 3D intraband absorption and 3D–3D carrier excitation mechanisms. In QWISPs, the activation energy, E_a, defined by
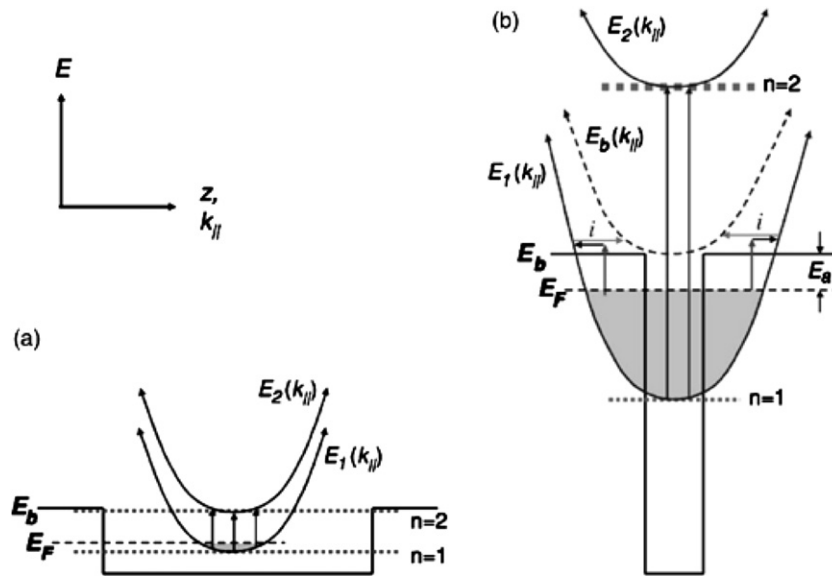
Figure 35 Schematic diagram of the energy dispersions and energy band diagrams of (a) a FIR/terahertz QWIP and a (b) QWISP showing intersubband and impurity scattering assisted intrasubband optical absorption and carrier extraction mechanisms. E_a, E_b, and E_F represent activation energy, barrier energy, and Fermi energy level, respectively. Reused with permission from David Z.-Y. Ting, 2007. Applied Physics Letters, 91, 073510. Copyright 2007, American Institute of Physics.

Table 4   Simulation parameters and results for GaAs/AlGaAs QWIPs (Luo *et al.*, 2005) (P1, P2, and P3) and QWISPs (S1, S2, and S3)

Sample	L_w (Å)	L_b (Å)	[Al] (%)	N_d (cm^{-3})	τ_l (ps)	τ_r (ps)	F (V cm^{-1})	E_a (meV)	λ_p (μm)	f (THz)
P1	119	552	5	1×10^{17}	10	200	3000	33.9	34	8.8
P2	15.5	70.2	3	6×10^{16}	10	350	600	19.9	57	5.2
P3	22.1	95.1	1.5	3×10^{16}	10	700	120	9.4	111	2.7
S1	50	552	15.9	5×10^{18}	5	50	3000	33.8	37	8.1
S2	50	702	14.2	5×10^{18}	5	50	600	20.6	58	5.2
S3	50	951	12.8	5×10^{18}	5	50	120	9.7	109	2.75

Here, τ_l, τ_r, F, E_a, λ_p, and f are capture lifetime, relaxation time, field, peak wavelength, and frequency, respectively. Reused with permission from David Z.-Y. Ting, Applied Physics Letters, 91, 073510 (2007). Copyright 2007, American Institute of Physics.

$E_a = E_b - E_F$ where E_b and E_F are barrier energy and the Fermi level, determines the wavelength threshold of the response, which also determines the dark current characteristics. Hence, unlike in QWIPs where the well width determines the operating wavelength, the well width in QWISPs is not the primary parameter. Instead, the barrier height (or the Al fraction in AlGaAs barriers) and the doping concentration together determine the operating wavelength, similar to HEIWIPs. According to Ting *et al.* (2007), the QWISPs are limited to low-temperature operation since the intrasubband relaxation times are considerably shorter at higher temperature (~ 100 fs). The modeling of QWISPs has been carried out using a three-dimensional supercell approach for incorporating impurity scattering effects at high doping concentrations, a 14-band k.p method (Cheah *et al.*, 2002) based formulation, and standard methods (Liu and Capasso, 2000a; Kozlowski *et al.*, 1991) for obtaining energy levels, wave functions, and properties such as absorption coefficient and responsivity.

Ting *et al.* (2007) have also carried out a theoretical analysis with a direct comparison between terahertz QWIP structures (reported by Luo *et al.* (2005)) and QWISP designs. Here, 'set P' refers to the terahertz structures reported by Luo *et al.* (2005) (samples V265, V266, and V267) and 'set S' refers to the QWISP designs proposed by Ting *et al.* (2007). The parameters used for the analysis are given in **Table 4**. For the terahertz QWIP structures, the required parameters such as well width (L_w), barrier width (L_b) barrier composition (Al%), and well doping density (N_d) were taken from Luo *et al.* (2005). The three QWISP designs S1, S2, and S3 had identical well widths (50 Å), but different barrier heights (Al fractions of 15.9, 14.2, and 12.8%, respectively) in order to match the activation energy values to QWIP structures P1, P2, and P3, respectively, as given in **Table 4**. In addition, all QWISP designs have high doping concentrations, while the capture lifetimes (τ_l) and relaxation times (τ_r) for QWISPs were obtained based on the experimental results (Schmidt *et al.*, 2002; Murdin *et al.*, 1997; Lutgen *et al.*, 1996). Based on the calculation of the absorption coefficient, the QWIPs (P1, P2, and P3) have shown absorption peaks for z-polarized light at 8.8, 5.3, and 2.7 THz (34, 57, and 111 μm), respectively, and these values agree with the experimental results (Luo *et al.*, 2005). All QWISP designs have
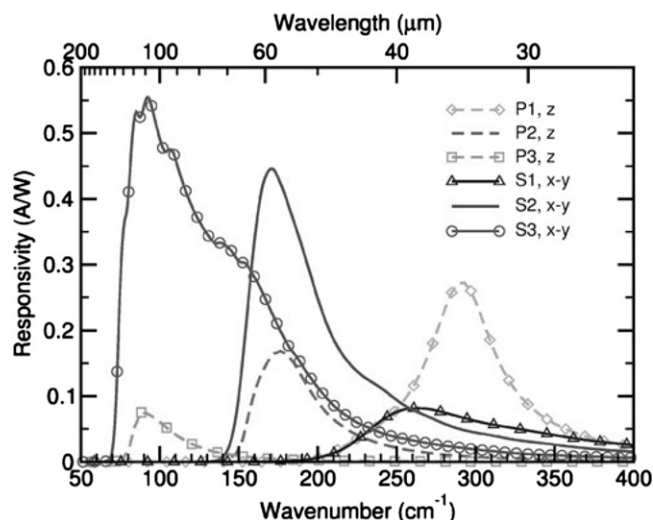
Figure 36 Calculated responsivity for terahertz QWIPs (P$_1$, P$_2$, and P$_3$) for 45°-incidence radiation and QWISPs (S$_1$, S$_2$, and S$_3$) for normal-incidence radiation. Reused with permission from David Z.-Y. Ting, 2007. Applied Physics Letters, 91, 073510. Copyright 2007, American Institute of Physics.

shown an absorption peak for z-polarized light at $\sim$30 THz (10 μm) due to bound-continuum electronic transitions (from n$=$1 state to n$=$2 state). For xy-polarized light, the samples S1, S2, and S3 have shown absorption peaks at $\sim$150 μm due to impurity scattering induced intrasubband transitions, which is the mechanism of interest in QWISPs for terahertz detection.

The calculated responsivity for QWIPs (P1, P2, and P3) for z-polarized light and for the QWISP designs (S1, S2, and S3) for xy-polarized light is shown in **Figure 36**. For corresponding samples in the two sets, the applied bias was chosen so that the electric field and the dark current stay comparable (see **Table 4**). The peak response wavelengths for the P1, P2, and P3 samples are the same as their absorption peak wavelengths (8.8, 5.3, and 2.7 THz), as expected. QWISP designs (S1, S2, and S3) have exhibited their peak responses for xy-polarized light at 8.1, 5.2, and 2.75 THz (37, 58, and 109 μm), respectively, while the response for z polarized light was not significant (not shown in the figure). As evident from **Figure 36**, calculations have shown that QWISPs dominate over QWIPs in the long wavelength region, while QWIPs become dominant in the short wavelength region. Also, QWISPs operate with normal incidence light (xy-polarized light), which is another advantage over QWIPs. Hence, the concept of QWISPs may be another option for terahertz detector development.

3.3 Terahertz Quantum Well Detectors Based on QCL-Like Superlattice Structures

While the terahertz QWIPs discussed before are based on bound-continuum electronic transitions, Graf *et al.* (2004) have reported a MBE grown GaAs/AlGaAs quantum cascade laser (QCL)-like superlattice structure in which bound-to-bound electronic transitions lead to terahertz radiation detection. A terahertz QWIP with a peak at $\sim$3.5 THz (54 μm) has been demonstrated with a responsivity of 8.6 mA W^{-1} and a detectivity of 5×10^7 Jones at 10 K. Another difference of this detector compared to other QWIPs is the ability to be operated under zero bias, which would lead to improved noise characteristics.

The active region consists of 60 periods of alternating Al$_{0.15}$Ga$_{0.85}$As/GaAs layers with thicknesses of 45, 110, 40, 135, 38, 145, 36, 180, 34, 210, 15, 100 Å. Only the 145 Å thick GaAs well was doped with Si to 2×10^{18} cm^{-3}. Each period was separated by a 200 Å GaAs spacer layer. Two 2×10^{18} cm^{-3} Si doped 6000 and 1000 Å thick GaAs layers were used as top- and bottom-contact layers, respectively. The CB profile of the structure at 10 K along with the calculated energy states and wave functions is shown in **Figure 37**. There are eight bound states (labeled as states 0–7) existing in different regions and the transitions leading to 3.6 THz occurs between the ground state (state 0) and states 4 (13.6 meV) and 5 (16 meV). The carriers excited into state 4 or 5 can tunnel into state 3, from where they fall down to the ground state of the next period ($3 \rightarrow 2 \rightarrow 1 \rightarrow 0$), effectively contributing to photocurrent. This mechanism is possible under zero bias. However, under an applied bias, the anti-crossing behavior of the strongly coupled (under zero bias) states 4 and 5 changes the tunneling probability, reducing the response.

As shown in **Figure 38**, the peak at $\sim$3.5 THz (54 μm) is due to transitions of electrons from state 0 to states 4 and 5 ($\Delta E=13.7$ and 16 meV). Also, it is reported that the transitions from state 0 to states 6 and 7 ($\Delta E=27.5$ and 34.2 meV) lead to photoresponse peaks at 6.5 THz (46 μm) and 8.8 THz (34 μm), respectively. This device has shown a peak responsivity of 8.6 mA W^{-1} and a detectivity of 5×10^7 Jones at 3.5 THz and 10 K temperature. At around -0.65 V, a substantially reduced differential resistance has been observed and this was attributed to the alignment of state 4 with state 0 in the next period. Furthermore, based on the Arrhenius plot (see inset to **Figure 39**) the activation energy was found to be 13.2 meV, which is in good agreement with the
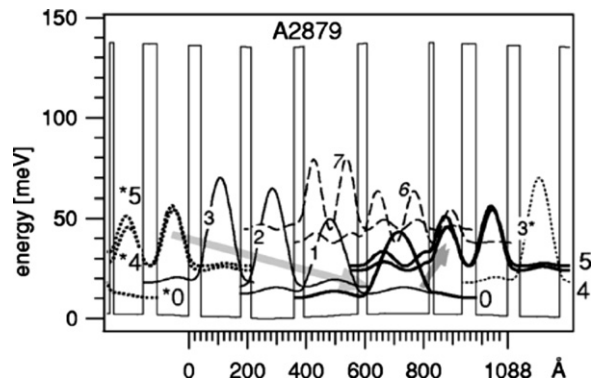
Figure 37 Self-consistently calculated conduction band profile of the QCL-like superlattice terahertz detector structure (Graf *et al.*, 2004) at 10 K. The observed transitions take place between the state 0 (ground state) and the states 4 and 5. These transitions have energies of 13.7 and 16.0 meV. The states 3, 2, and 1 provide a relaxation channel for the electrons tunneling into the ground state of the next period. Reused with permission from Graf, Marcel, 2004. Applied Physics Letters, 84, 475. Copyright 2004, American Institute of Physics.
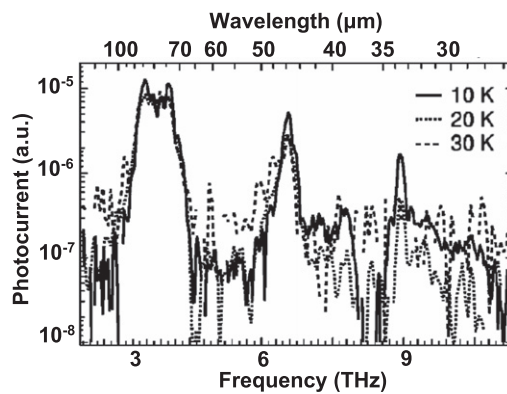
Figure 38 Responsivity of the QCL-like superlattice terahertz detector at 10, 20, and 30 K. The different peaks can be matched with the calculated transition energies. Reused with permission from Graf, Marcel, 2004. Applied Physics Letters, 84, 475. Copyright 2004, American Institute of Physics.
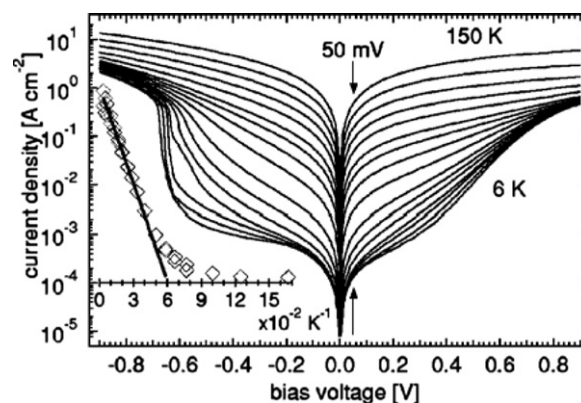
Figure 39 Dark IV characteristics of the QCL-like superlattice terahertz detector at temperatures in the 6–150 K range. The inset shows an Arrhenius plot of current densities at 50 mV bias. The solid line is a fit resulting in an activation energy of 13.2 meV which is in good agreement with the (0→4) transition energy of 13.7 meV. Reused with permission from Graf, Marcel, 2004. Applied Physics Letters, 84, 475. Copyright 2004, American Institute of Physics.

calculated transition energy and the observed peak position. From this study, it can be concluded that the QCL-like band structure could be a potential choice for terahertz detector development. Further optimizations are possible based on the band structure modification and avoiding unwanted current paths to reduce the dark current.

Figure 40 The variation of the transition energies in the DMS-based QWIP corresponding to maximal oscillator strength for spin-down and spin-up electrons against magnetic-field, at a fixed electric field of 1 kV cm^{-1} at 1.5 K. Reused with permission from Savic, Ivana, 2005. Journal of Applied Physics, 98, 084509. Copyright 2005, American Institute of Physics.

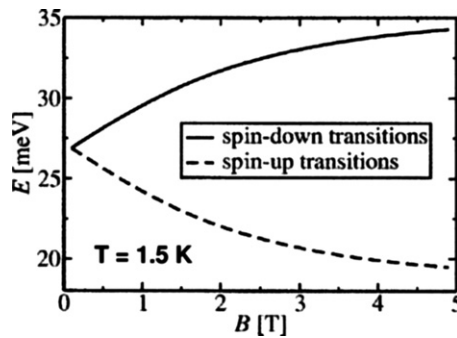### 3.4 Magnetic-Field Tunable Terahertz Quantum Well Detectors

Real time wavelength tunability is an important property for a photodetector, which can be achieved using an applied electric field (Krishna *et al.*, 2005; Ariyawansa *et al.*, 2008) or a magnetic field. Savic *et al.* (2005) reported a QWIP based on a dilute magnetic semiconductor (DMS) material system, CdMnTe, with 8.64 nm $Cd_{0.89}Mn_{0.11}Te$ magnetic wells and 86.4 nm $Cd_{0.855}Mg_{0.145}Te$ non-magnetic barriers. As reported by Savic *et al.* (2005), the unique property of a DMS is associated with the band structure with two electronic subsystems: delocalized band electrons and magnetic impurity electrons with magnetic moments localized in ionic open 3d (or 4f) shell. These localized magnetic moments provides the magnetic sensitivity in the DMS material giving rise to the magnetic field sensitivity of the QWIP. The magneto-optical properties of DMSs result from the strong spin-dependent $sp - d(f)$ exchange interactions between these two subsystems (Furdyna, 1988). In a QW structure made of DMS materials, the CB edge changes with the applied magnetic field due to the *sp–d* interaction, which in turn modifies the potential profile of the well for the two spins. In an optical transition caused by z-polarized light, due to the conservation of the spin and Landau level, the energy associated with the transition varies with the applied magnetic field, leading to a tunability in the light absorption wavelength (or response wavelength of the detector), thus providing magnetic field tunability.

In Savic's design, the optical transition energy between the ground and the first excited state (continuum state) under an electric field of 1 kV cm^{-1} and 0 T magnetic field is 26.9 meV. As shown in **Figure 40**, the transition energy at 1.5 K increase with magnetic field up to 34.3 meV for spin-down, while it decreases to 19.5 meV for spin-up case. Since the $sp - d$ exchange interaction saturates at 5 T, the variation of the transition energy becomes constant beyond 5 T. Hence, the maximum range of tunability in the transition energy is 19.5–24.1 meV and it translates to a detection frequency range of 5.8–8.3 THz (51.4–36.1 μm) for a magnetic field ranging from 0 to 5 T.

4 Terahertz Quantum Dot Detectors

In the field of infrared (IR) detector technology, quantum dot infrared photodetectors (QDIPs) have been studied aiming to develop IR optoelectronic devices with improved performance. In comparison with QWIPs, QDIPs have additional degrees of confinement, leading to three major advantages (Rogalski, 2003): (1) sensitivities to normal-incidence radiation, which is forbidden in *n*-type QWIPs due to polarization selection rules, (2) comparatively long ($\sim$ 100's of picoseconds) effective carrier lifetimes, which has been predicted by theory (Urayama *et al.*, 2001) and confirmed by experiment (Kim *et al.*, 2004), and (3) low dark current. QDIPs are expected to show improved performance characteristics such as high responsivity, high detectivity, and high operating temperatures. However, such dramatic improvements have not yet been demonstrated probably due to the bound-to-continuum transitions in reported QDIPs, as opposed to transitions from ground-state to a bound-state in the QDs.

Work on QD based infrared detectors has been increasing for the past few years. QDIPs ranging from single element detectors (Su *et al.*, 2006; Ariyawansa *et al.*, 2008; Aslan *et al.*, 2003; Kochman *et al.*, 2003; Liu *et al.*, 2001; Jiang *et al.*, 2003; Raghavan *et al.*, 2002; Krishna *et al.*, 2003; Ariyawansa *et al.*, 2005a; Bhattacharya *et al.*, 2005; Jiang and Singh, 1997; Su *et al.*, 2005; Chakrabarti *et al.*, 2005) to FPAs (Krishna *et al.*, 2005; Gunapala *et al.*, 2007a; Tsao *et al.*, 2007) have been reported. In addition to the afore mentioned advantages, QDIPs are reported to have improved radiation hardness (Ryzhii and Khmyrova, 2002; Ryzhii, 1996; Leon *et al.*, 2000) and polarization sensitive spectral responses (Aslan *et al.*, 2003; Pal *et al.*, 2003). QDIPs operating at temperatures above 77 K (Kochman *et al.*, 2003; Sergeev *et al.*, 2002; Ye and Campbell, 2002; Phillips *et al.*, 1998; Maimon *et al.*, 1998; Pan *et al.*, 1998; Lim *et al.*, 2007) indicate the possibility of developing uncooled or thermo-electrically (TE) cooled IR imaging systems. In a recent publication, Matthews *et al.* (2007) reported an extremely long carrier lifetime of 3–600 ns for a DWELL detector, which

also exhibits a photoconductive gain of 10^4–10^5 in the 20–100 K temperature range. However, there is very limited work reported on the development of terahertz detectors based on QD structures. While the potentials and benefits of QD-based structures as photodetectors have been identified, there are several areas still needing to be understood and developed. One of the major problems associated with QD-based devices is related to the QD size and shape, which play a major role in QDIPs. The growth of QDs is a self-assemble process that results in an unintentional size fluctuation. In general, the size fluctuation of QDs affects the electrical and optical properties of the device, limiting the overall performance. Although there are issues still to be resolved, possible results on QD-based detectors for terahertz detection have been reported (Su *et al.*, 2006; Huang *et al.*, 2008) recently. Even though the most common material used for QDIPs is the InAs/GaAs (or InGaAs/GaAs) material system, QDIPs are being developed using SiGe/Si (Lin *et al.*, 2007; Tong *et al.*, 2005; Cha *et al.*, 2007) and GaN/AlN material systems (Doyennette *et al.*, 2006). These could also be of interest for possible terahertz detector development.

4.1   Calculation of the Energy States in a Quantum Dot

A large amount of theoretical work (Jiang and Singh, 1997; Amtout *et al.*, 2004; Califano and Harrison, 2000; Lin and Singh, 2002; Schmidt *et al.*, 1996; Pokatilov *et al.*, 2001) has been carried out to solve a 3D confined quantum mechanical systems, such as QDs. Finding solutions for a hypothetical 3D system is complicated but achievable with high accuracy. However, the QDs formed by a self assembled process, having odd shapes, introduces many complications for modeling. These complications will be further enhanced when the stress, primarily due to lattice mismatch, is involved, which in general plays a role in the formation of QDs in the self assembled process. Hence, the existing theoretical models involving complicated calculations will always present a high uncertainty in the results. The most commonly reported model for solving the energy spectrum of QDs is the 8-band k.p model (Jiang and Singh, 1997). This model uses the strain in the QD, calculated using the valence force field (VFF) model which has been successful in calculating the strain tensor in self-assembled QDs.

While the calculation of the band structure and energy states in QD system is useful to determine potential device designs, the investigation of optical properties of a QD system is also invaluable. The intersubband absorption coefficient of a photon with energy $\hbar\omega$ in a QD layer can be expressed as (Kochman *et al.*, 2003)

$$\alpha(\hbar\omega) = \frac{\pi e^2 \hbar}{\varepsilon_0 n_0 c m_0^2 V_{av}} \frac{1}{\hbar\omega} \sum_{fi} |a \cdot Pfi|^2 N(\hbar\omega) \qquad [9]$$

where V_{av} is the average QD volume, a is the polarization of the incident light, p_{fi} is the momentum matrix element between energy states, and $N(\hbar\omega)$ is the electron density of states. Considering a Gaussian inhomogeneous broadening due to the large fluctuation in QD size, $N(\hbar\omega)$ is given by

$$N(\hbar\omega) = \frac{1}{\sqrt{2\pi}\sigma} \exp\left\{\frac{-(E_{fi} - \hbar\omega)^2}{2\sigma^2}\right\} \qquad [10]$$

where E_{fi} is the energy separation between states, and σ is the linewidth of the transition. The momentum matrix element is calculated from the QD wavefunctions, which can be obtained from the 8-band **k.p** model. The spectral response of a QD-based detector is characterized by peak wavelength (λ_p), peak responsivity (R_p), and the peak quantum efficiency (η_p). Responsivity is given by $R = q\eta\lambda/hc$, where q is the electron charge, λ is the wavelength, h is the Planck constant and c is the speed of light. Quantum efficiency can be calculated from the absorption coefficient (from Eq. [9]) and the thickness of the absorption region.

Apart from this method, several other approaches were tested for solving a QD-based system. For example, an energy level calculation model for a DWELL system was proposed by Amtout *et al.* (2004). DWELL structures with different QDs have been tested experimentally, and electronic spectra obtained by the model are in good agreement with the experimental results (Amtout *et al.*, 2004). The pyramidal shape (Su *et al.*, 2006) QDs have been confirmed by transmission electron microscopy. The Hamiltonian of a system with a quasi-zero dimensional QD placed in a two-dimensional QW is defined with a potential energy consisting of four terms: the potential in the QD region, the potential in the QW region, the potential in the barrier region, and the potential from the applied electric field. The eigenfunctions of the Hamiltonian are derived using a Bessel function expansion. The DWELL detectors tested by Amtout have QDs with base dimensions of 110 and 140 Å and heights of 65 and 50 Å, respectively. The energy spacing between the first and second energy levels obtained from the model for the two samples are 132 and 150 meV, whereas experimental analysis showed energy spacing of 123 and 140 meV, respectively. Although the energy states are shifted by the electrostatic potential from the bias field, the energy spacing between the first two energy states was not changed significantly by the applied electric field. This can be observed in the spectral response of many DWELL detectors (Krishna *et al.*, 2003; Ariyawansa *et al.*, 2005a).

Using these theoretical models, QDIPs can be designed using the transitions of carriers between QD states. Simply, the energy spacing between QD states are adjusted by varying the QD size, shape, and the materials of the QD as well as the barrier. However, for the design to be realistic, growth limitations, particularly the QD size, will have to be taken into account. The most common

size practically possible has base dimensions of ~ 20 nm and a height of ~ 6 nm. Hence, the practical possibilities for tailoring the operating wavelength is very limited. However, there is an increased interest in growing different size QDs and any successful achievement would be beneficial for future QD-based terahertz device development. Keeping the growth possibilities restrained at the current level, there will also be alternative approaches to tune the transition energy states to achieve terahertz detection. One of these approaches is the use of intersubband electron transitions in QDs (Huang et al., 2008), while the other approach uses resonant tunneling (Su et al., 2006) to selectively block the dark current, without blocking the photocurrent. These structures are specifically designed for high temperature operations.

4.2   Self-Assembled Quantum Dot Size Effects

In a QDIP, the size of the dot plays a major role, particularly in determining the response wavelength (frequency) range. However, with the present growth techniques, it is not possible to obtain QDs with any size as desired. The typical size of the near-pyramidal InAs/GaAs self-organized QDs (Krishna et al., 2003; Phillips et al., 1998) is ~ 60–70 Å (height)/~ 200–250 Å (base) with QD density varying between 5–10 $\times 10^{10}$ cm^{-2}. For In$_{0.4}$Ga$_{0.6}$As/GaAs QDs (Bhattacharya et al., 2005), the typical height and base are 60 and 200 Å, respectively. The electron intersublevel energy separation in these QDs ranges between 40 and 80 meV. As reported by Aslan et al. (2003), the height of the disk-shaped QDs can also be as narrow as 25 Å in the growth direction (height), while the base remains around 180 Å. Hence, the confinement along the growth direction is strong, while the in-plane confinement is weak. As reported by Su et al. (2006), the growth of smaller QDs (40 Å of height and 130 Å of width), leading to a large energy spacing (~ 124 meV) between the QD ground and first excited-states, is also possible with InAlAs/GaAs material combination. In such QDs, the intersubband transitions between lower QD states lead to shorter wavelength detection, while the transitions from the upper states (particularly in T-QDIPs discussed in Section 4.4) lead to longer wavelength detection (Su et al., 2006). Smaller QDs also provide a large QD density for the same amount of adatom change, which increases the absorption of radiation.

4.3   Intersubband Terahertz QDIPs

Theoretical calculations carried out by Huang et al. (2008) show that the In$_{0.4}$Ga$_{0.6}$As QDs in GaAs barriers exhibit multiple confined electronic energy states. The transitions of electrons from these energy states to the continuum would lead to multiple response peaks, with at least one falling in the terahertz region. Huang et al. (2008) reported a In$_{04}$Ga$_{0.6}$As/GaAs QD-based terahertz detector exhibiting two color characteristics with response peaks in the 3–13 and 20–55 μm (15–5.4 THz) ranges and operating up to 150 K. With this detector structure, two major disadvantages have been overcome: one is the use of a simple heterostructure compared to complicated terahertz detector structures (Su et al., 2006; Graf et al., 2004) and the other is the higher temperature operation for the terahertz region compared to terahertz QWIPs (Liu et al., 2004; Luo et al., 2005; Graf et al., 2004).

The schematics of the In$_{0.4}$Ga$_{0.6}$As/GaAs QDIP heterostructure grown by MBE on a (001)-oriented semi-insulating GaAs substrate is shown in **Figure 41(a)**. The near-pyramidal (Su et al., 2006) shape QDs had an average base width of 21 nm and a height of 5 nm as estimated from atomic force microscopy measurements (Su et al., 2006). The active region consisted of 20 periods of In$_{0.4}$Ga$_{0.6}$As/GaAs QD layers separated by a 500 Å thick GaAs spacer layer. The QDs and the spacer layers were grown continuously at 500 °C. One of the critical parameters in this design is the doping concentration, since the electron occupancy in the bound states is important for various transitions at different temperatures. QDs were doped with silicon as the dopant to a level of 1 electron per QD. The active layers were then sandwiched between 0.2 and 0.8 μm thick highly doped (2×10^{18} cm^{-3}) GaAs layers, which act as top- and bottom-contact layers, respectively. The tested structures had vertical circular shape mesas with 600 μm diameter for top illumination, which were fabricated using standard photolithography, wet chemical etching, and metallization techniques, and were mounted on chip carriers.

Theoretical calculations based on the 8-band **k.p** model (Jiang and Singh, 1997) exhibited four bound states (E0, E1, E2, and E3) for this structure as shown in **Figure 41(b)**. The locations of the energy states with respect to the GaAs band edge and two sets of possible transitions in the QDs are also shown in the figure. One set includes the transitions of electrons from any of the states to
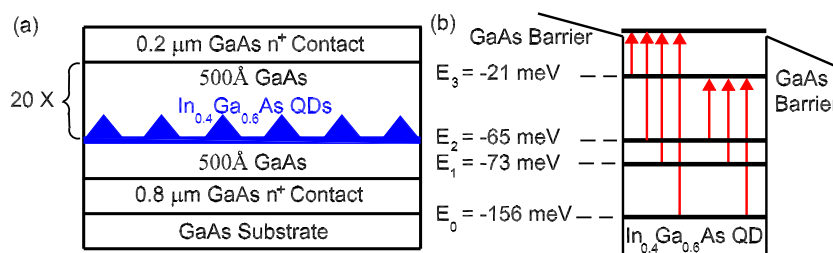

Figure 41   (a) Schematic diagram of the terahertz QDIP structure. (b) Conduction band profile along with the energy states and possible electronic transitions between states. Reused with permission from Huang, G., 2008. Applied Physics Letters, 92, 011117. Copyright 2008, American Institute of Physics.
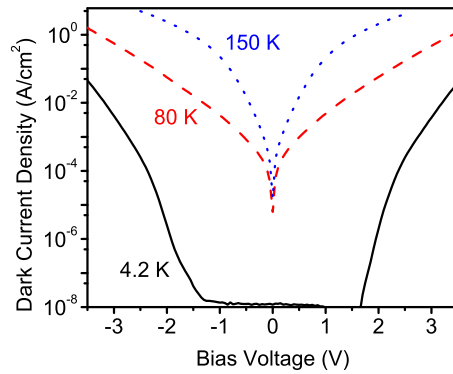
Figure 42   Dark current density of the terahertz QDIP at 4.2, 80.and 150 K. Reused with permission from Huang, G., 2008. Applied Physics Letters, 92, 011117. Copyright 2008, American Institute of Physics.
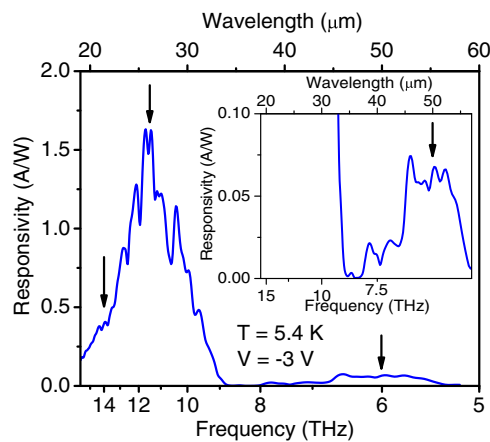

Figure 43   Calibrated spectral response of the terahertz QD-based detector at 5.4 K. The observed peak positions are indicated by vertical arrows. The response around 6 THz (50 μm) has been expanded in the inset.

the continuum, leading to response peaks at 37.5, 17.6, 15.8, and 5.2 THz (8, 17, 19, and 58 μm), while the other set consists of the transitions to the third excited state (E3) leading to response peaks at 32.6, 12.6, and 10.7 THz (9.2, 23.8, and 28 μm). The photocurrent observed due to transitions to the E3 state is weak, as these excited carriers are blocked by the barrier. Also, few of the transitions in the two sets overlap in the energy scale (wavelength) resulting in only a few dominant response peaks. Another important effect will be the temperature dependency of the transitions involving higher states.

The dark current–voltage (IV) characteristics of this detector, as shown in **Figure 42**, shows a typical variation of current density with the temperature. At high temperatures (80 K and above), the dark current density is lower compared to any other detector (excluding QDIPs) responding in comparable wavelength regions. At -2 V bias, the dark current density values are 6.5×10^{-6}, 5.5×10^{-2}, and 2.3 Å cm^{-2} at 4.2, 80, and 150 K, respectively. This observed dark current reduction is attributed to the high carrier confinement in QDs. The calibrated responsivity at 5.4, 80 and 120 K is shown in **Figures 43** and **44**. The agreement of calculated and experimental data confirms the validity of the **k.p** model for pyramidal QDs. The peak centered around 11.5 THz (26 μm) could be matched with the transition from the E_2 state to the E_3 state ($\Delta E = 44$ meV (28 μm)), while the shoulder around 13.6 THz (22 μm) was assigned to transition from the Ei state to the E_3 state ($\Delta E = 52$ meV (23.8 μm)). The peak centered around 6 THz (50 μm) was assigned to the transitions from the E_3 state to the continuum ($\Delta E = 21.3$ meV (58 μm)). In addition, there is a clear peak at 37.5 THz (8 μm) as shown in **Figure 44** (this has not been measured at 5.4 K, although expected). This peak matched with the transition from the E0 state to the continuum ($\Delta E = 155$ meV (8 μm)). The sharp dip at 8.1 THz ($\sim$37 μm) is due to the longitudinal optical phonon absorption in GaAs, which is typical for GaAs-based devices.

In order to confirm the terahertz mechanism in this structure, the temperature dependence of the peaks at 11.5 and 6 THz can be considered. At low temperatures, carrier occupancy in upper states, for example E_3, is relatively low. Hence, the transition from upper states are weak, and as a result, the peak at 6 THz is relatively weak at 5.4 K. At high temperatures, since the carrier density in upper states becomes high, an enhanced responsivity was expected for the response peak originating from upper states (6 THz peak). This effect of the temperature is evident from **Figures 43** and **44**. However, at 80 and 120 K, the separation of the two peaks (11.5 and 6 THz) is not clear. The thermal broadening of the energy states and the enhanced transitions from upper states resulted
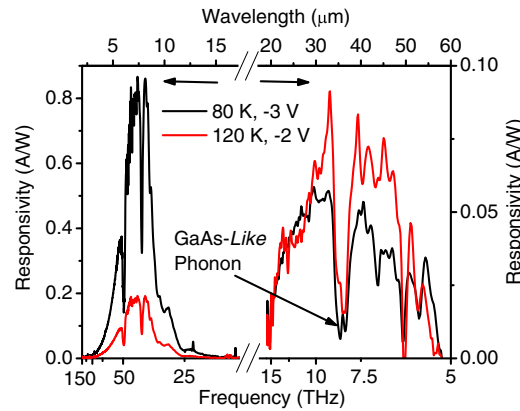
Figure 44 Calibrated spectral response of the terahertz QD-based detector at 80 and 120 K. The response below 20 THz (15 µm) is scaled with left vertical axis, while the response above 15 THz (20 µm) is scaled with the right vertical axis. Reused with permission from Huang, G., 2008. Applied Physics Letters, 92, 011117. Copyright 2008, American Institute of Physics.
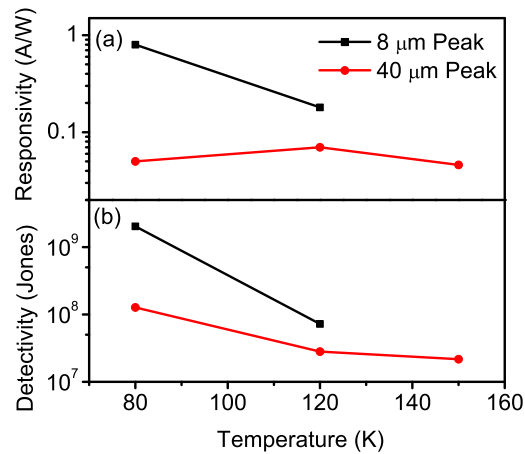

Figure 45 Variation of (a) peak responsivity and (b) specific detectivity of terahertz QD based detector with temperature. Adapted from Huang et al. (2008) with permission.

in a combined broad peak in 15–5.26 THz (20–57 µm) range instead of two separate peaks. However, it is clear that the responsivity at 6 THz has increased, while the responsivity at 11.5 THz has decreased drastically when the temperature was increased from 5.4 to 120 K. The responsivity at 7.5 THz (40 µm) is 0.05 and 0.08 Å W^{-1} at 80 and 120 K, respectively. Furthermore, the peak responsivity of the 37.5 THz (8 µm) peak decreased by 80% when the temperature is increased from 80 to 120 K. The responsivity of the 37.5 THz peak is 0.86 and 0.19 Å W^{-1} at 80 and 120 K, respectively.

The variation of the responsivity with the temperature is depicted in **Figure 45(a)**. These observations are consistent with the thermal effects explained above. The maximum operating temperature reported (Huang et al., 2008) for this device was 150 K with a peak responsivity at 7.5 THz (40 µm) is still as high as 0.05 Å W^{-1}. The specific detectivity (D^*), which is a measure of the signal-to-noise ratio of the device, was calculated from the measured peak responsivity R_p and noise density spectra S_j at different temperatures and applied biases. The noise spectra were measured with a dual channel fast Fourier transform signal analyzer and a low noise preamplifier. The specific detectivity calculated from $D^* = R_p A^{1/2} / S_i^{1/2}$ for the 37.5 THz peak were 2×10^9 Jones at 80 K under -3 V bias and 7.2×10^7 Jones at 120 K under -2 V bias. For the 7.5 THz peak, the values of D^* were 1.3×10^8 Jones at 80 K under -3 V bias, 2.8×10^7 Jones at 120 K under -2 V bias, and 2×10^7 Jones at 150 K under -2 V bias. The variation of the D^* with temperature is shown in **Figure 45(b)**. These D^* values for the terahertz transition are larger compared to terahertz QWIPs discussed before. It can be concluded that the 5 THz detection up to 150 K in the QD-based detector have been achieved based on a thermal-assisted mechanism in QDs.

4.4 Tunneling Quantum Dot Infrared Photodetectors (T-QDIPs) for Terahertz Detection

A typical detector structure, in which the transitions leading to terahertz detection occur between two electronic states with an energy difference of ΔE (~ 4.1 meV for 1 THz), will have limitations for high temperature terahertz detection since the dark current
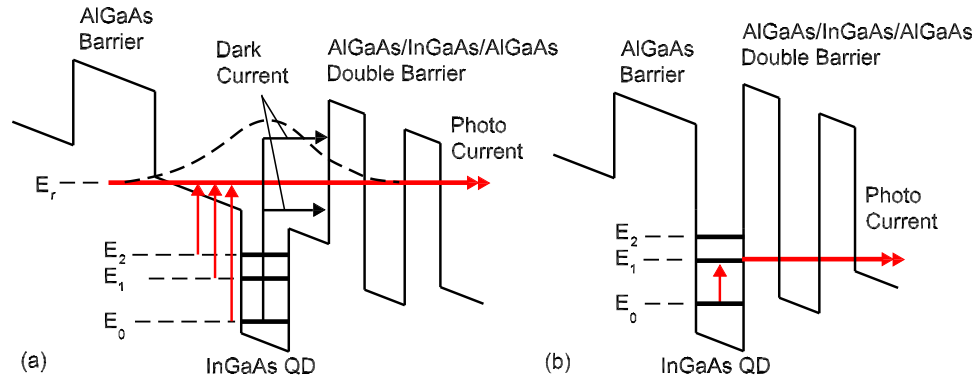
Figure 46 (a) Schematic diagram of the conduction band profile of a T-QDIP structure under a bias. E_0, E_1, and E_2 are the energy level positions in the QD with respect to the resonant-state E_r. Only the carriers excited to the resonant-state contribute to the photocurrent. (b) A possible terahertz T-QDIP structure grown on AlGaAs barriers and directly coupled with a double-barrier. Reused with permission from Bhattacharya, P., 2005. Applied Physics Letters, 86, 191106. Copyright 2005, American Institute of Physics.

due to thermal excitations become dominant even at 77 K due to the small ΔE. However, the tunneling quantum dot infrared photodetector (T-QDIP) structures (Ariyawansa et al., 2008; Bhattacharya et al., 2005; Su et al., 2006, 2005; Chakrabarti et al., 2005), in which the photocurrent is selectively collected while the dark current is blocked, provides the flexibility for modification to obtain terahertz response, thus, offering a suitable platform for high operating temperature terahertz detectors. Su et al. (2006) have explored a resonant tunneling QD device architecture demonstrating room temperature IR detection at 50 and 17.6 THz (6 and 17 μm). Later, the same idea was used to extend the operating wavelength into the terahertz region, demonstrating a terahertz T-QDIP (Su et al., 2006) operating at 6 THz up to 150 K. In general, any device structure designed to reduce the dark current, will also reduce the photocurrent. The characteristics of the terahertz T-QDIP reported by Su et al. (2006), showing two color response at 6 THz, will be discussed here.

A T-QDIP structure can also be considered as an extended DWELL structure. That is, a DWELL structure coupled with a double-barrier (tunneling-barrier) system has several advantages over a regular DWELL structure. Incorporating a double-barrier into a QDIP structure design to achieve resonant tunneling allows the reduction of the dark current without reducing the photocurrent, thus, leading to higher performance. A typical T-QDIP consists of InGaAs QDs embedded in a AlGaAs/GaAs QW, which is then coupled to a AlGaAs/InGaAs/AlGaAs double-barrier system. The CB profile of a T-QDIP structure under an applied reverse bias is shown in **Figure 46(a)**. Pulizzi et al. (2005) have reported resonant tunneling phenomena for a similar QD-based structure coupled with a double-barrier. The photocurrent generated by a transition from a state in the QD (E_0, E_1 or E_2) to a state in the QW, which is coupled with a state in the double-barrier system, is collected by resonant tunneling. In this discussion, the energy state in the QW is denoted as the resonant-state, E_r, since it is associated with resonance tunneling. The double-barrier system blocks the majority of carriers contributing to the dark current (carriers excited to any state other than the resonant-state in the QW). The tunneling probability for carriers excited by radiation with energy equal to the energy difference between the QD ground-state and the resonant-state is near unity (Bhattacharya et al., 2005).

The steps to follow for theoretical modeling of a T-QDIP is straight forward as reported by Su et al. (2005). First, the QD energy levels were calculated using the 8-band **k.p** model (Jiang and Singh, 1997). Then the size of the QD and the confinement potential were determined such that the required spacing between energy levels could be obtained. The width and the confinement potential of the QW, in which QDs are placed, are adjusted to obtain the resonant-state at a level so that the transitions from QD states to the resonant state give rise to response peaks at required wavelengths. The energy states in the QW, including the presence of the wetting layer and the double barrier system, were calculated by solving the one dimensional Schrodinger equation. The double-barrier system (AlGaAs/InGaAs/AlGaAs) is integrated with each QW in which a QD is placed, and is designed such that the resonant-state coincides with a bound state in the double-barrier system under certain bias conditions. This introduced a higher potential barrier for thermal excitations, while the photoexcitation energy remains very low. The transmission probability for the double barrier structure was calculated using the transfer matrix method (Anemogiannis et al., 1997). Due to the energy-dependent tunneling rate of the double-barrier system the dark current resulting from carriers with a broad energy distribution is suppressed. Thus, the dark current can be significantly reduced, particularly at high temperatures.

For designing T-QDIP structures for terahertz sensing, several design modes were used (Bhattacharya et al., 2005; Su et al., 2006). The CB profile of one possible structure is illustrated in **Figure 46(a)**. In this approach (Su et al., 2006), the transition energy between the E_2 state and the E_r state corresponds to 5 THz radiation. The energy spacing for this transition can be adjusted by changing the GaAs QW parameters without changing the QD parameters. Hence, this provides an advantage when the QD size and other parameters are restrained by the growth technique. Flexibility for reducing the QD size would raise the upper energy states closer to the E_r state. However, to obtain a strong transition between these two states, the carrier occupancy in the E_2 state should be increased. One possibility is to adjust the doping concentration in the QDs so that the Fermi level rises above the E_2 state.

Also, in this case the photoresponse can be enhanced by increasing the temperature, similar to the terahertz QD-based detector discussed before. Another possibility is to grow QDs on AlGaAs barriers directly coupling the QDs with a double-barrier, as shown in **Figure 46(b)**. In this design, the transition leading to a terahertz response can be expected to occur under a certain bias condition between the E_0 and E_1 states, if the E_1 state overlaps with the double-barrier state. However, in this case the only way to adjust the responding wavelength is to adjust the QD size. Although increasing the QD size would reduce the energy spacing, pushing the response towards 1 THz, that will introduce other energy states in the QD, diminishing the 3D-confinement effects. Also, for efficient dark current blocking, the broadening of the resonant-state has to be at a minimum, i.e. the resonant-state should be strongly bound. Basic parameters should be adjusted so that the tunneling probability remains close to unity and the carrier escape lifetime is smaller than the carrier recombination lifetime. The Fermi level in the QD (and the QD ground-state) should always be kept below the band edge of the QW. Thus, all these factors need to be taken into account to design an optimized detector exhibiting low dark current.

The structure of the MBE grown terahertz T-QDIP detector, reported by Su *et al.* (2006), is shown in **Figure 47 (a)**. Self organized $In_{0.6}Al_{0.4}As$ QDs were grown on a GaAs layer and doped with Si. The stack of $Al_{0.3}Ga_{0.7}As/In_{0.1}Ga_{0.7}gAs/Al_{0.3}Ga_{0.73}As$ layers served as the double-barrier system. The GaAs and AlGaAs layers were grown at 610 °C and the rest of the structure was grown at 500 °C. The top and bottom GaAs contact layers were n-doped with Si to a level of 2×10^{18} cm^{-3}. In order to obtain a transition leading to a response in terahertz region, the excited-states in the QD was pushed towards the resonant-state by forming smaller QDs. The QDs were doped to raise the Fermi level so that photoexcitations take place from an upper state in the QD to the resonant-state. In order to reduce QD size, $In_{0.6}Al_{0.4}As$ was used instead of InGaAs since the Al-containing islands (QDs) are smaller in size compared to InAs (or InGaAs) islands due to the smaller migration rate of Al adatoms on the growing surface during epitaxy. The QD size was reported (Su *et al.*, 2006) to be 40 Å (height) and 130 Å (width).

The dark current density of terahertz T-QDIP at different temperatures is shown in **Figure 48**. At -2 V bias, the dark current density values are 6.5×10^{-8}, 7.9×10^{-2}, and 8.3 Å cm^{-2} at 4.2, 80, and 150 K, respectively. At temperatures above 80 K, this terahertz T-QDIP

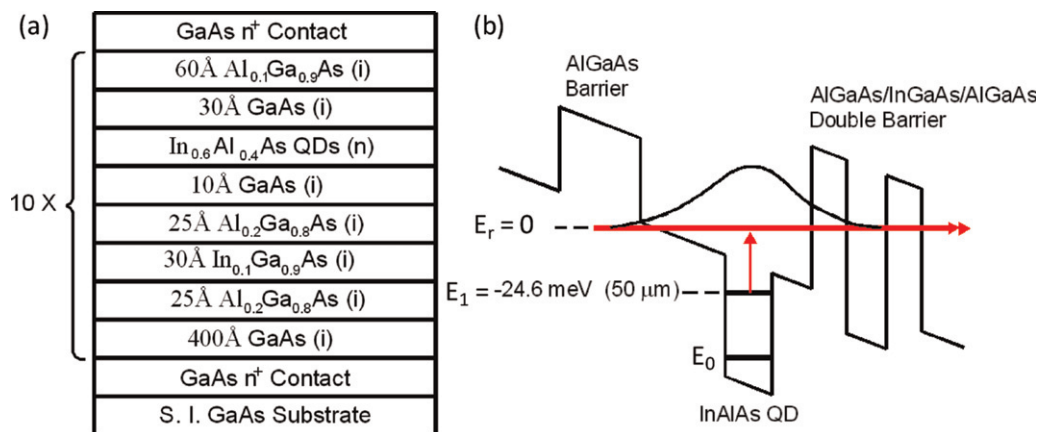**Figure 47** (a) Structure of a T-QDIP THz detector. $In_{06}Al_{04}As$ QDs are n-doped with Si. The growth of smaller QDs compared to InAs or InGaAs QDs was achieved using InAlAs material. The QD size has been considerably reduced to 40 Å (height) and 130 Å (width). (b) Conduction band profile of the THz T-QDIP under reverse applied bias along with the calculated bound state energies in the dots and wells. After Reference Su *et al.* (2006).
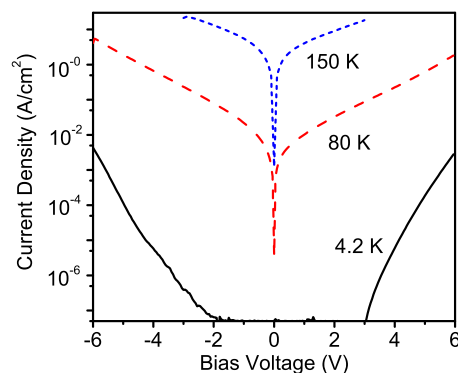

Figure 48 The dark current density of terahertz T-QDIP as a function of bias in the temperature range 4.2–150 K. In the reported response range, the T-QDIP detector shows a lower dark current density compared to other terahertz detectors. Reused with permission from Su, X.H., 2006. Applied Physics Letters, 89, 031117. Copyright 2006, American Institute of Physics.
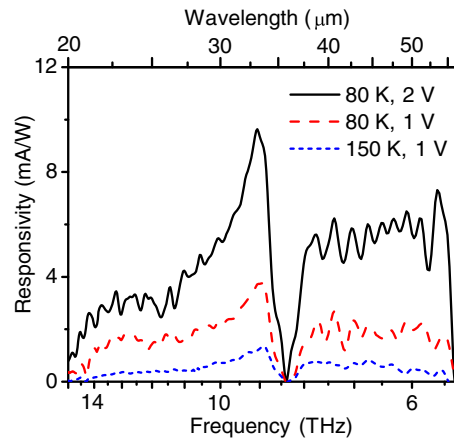
Figure 49   Spectral responsivity of terahertz T-QDIP in the temperature range 80–150 K. The dip at 8.1 THz (37 μm) is the reststrahlen region of GaAs. Terahertz operation at high temperature (150 K) is made possible by the incorporation of resonant tunneling phenomena into the device structure. Reused with permission from Su, X.H., 2006. Applied Physics Letters, 89, 031117. Copyright 2006, American Institute of Physics.

detector showed a lower dark current density compared to other terahertz detectors (Esaev et al., 2004b; Luo et al., 2005) operating in the 15–5 THz ($\sim$ 20–60 μm) range irrespective of the bias voltage. However, compared to the terahertz QD-based detector discussed in Section 4.3, this T-QDIP has a lower dark current density at low temperatures irrespective of the bias. At high temperatures (above 80 K), the T-QDIP showed a lower dark current density only for bias voltages above 1 V. This variation of the dark current for the T-QDIP with bias voltage is attributed to dark current blocking from the tunneling barriers.

The CB profile of the terahertz T-QDIP detector is shown in **Figure 47(b)**. This structure exhibits only two bound states in the QD due to the reduced dot size. The electrons excited from the upper bound state to the resonant state lead to the photocurrent. The location of the upper bound state is -24.6 meV (5.5 THz, 54.6 μm) with respect to the resonant state, and a response peak centered around 5.5 THz is expected. At the frequency of 6 THz, the measured spectral response of the detector at 80 and 150 K showing responsivities of 6 and 0.6 mA W^{-1} is shown in **Figure 49**. The sharp dip around 8.1 THz (37 μm) is due to the reststrahlen band of GaAs, which is present in all GaAs based photon detectors (Rinzan et al., 2005b; Luo et al., 2005). The observed full-width at half maximum (FWHM) of the spectral response is $\sim$ 35 meV. This spectral broadening arises from the inhomogeneous size distribution of self-organized QDs. While this broadening is useful to obtain a broad spectral response, as shown here, it will weaken the resonant conditions. This could be one of the reasons for not exhibiting negative differential regimes in the I–V data as in QWIP structures. For efficient resonant tunneling leading to low dark current, tight resonant conditions are required. Hence, the QD size and shape fluctuations need to be minimum, which could be achieved using improved growth techniques in the future.

The measured detectivity for the terahertz T-QDIP at 6 THz was $\sim 5 \times 10^7$ Jones at 80 K under a bias of 1 V. While this value of D* is not high enough for applications, T-QDIP structure provides the flexibility for optimization. It can be concluded that as the first step towards the development of high temperature terahertz detectors, incorporation of resonant tunneling phenomena into a QDIP structure was demonstrated with a detector operating up to 150 K. In order to achieve terahertz detection in 1–3 THz region at high temperatures, several issues need to be resolved such as the growth of small QDs with reduced size fluctuation, optimization of structure parameters, and tight resonant conditions to maintain a low dark current without reducing the photocurrent.

4.5   Terahertz Quantum Ring Detectors

Advancing QD growth process further, a process in which QDs are transformed into quantum rings (QRs) by postepitaxy thermal annealing has been reported, (Lorke et al., 2001) also demonstrating the feasibility of terahertz detection utilizing the electronics transitions in QRs (Huang et al., 2009; Bhowmick et al., 2010; Dai et al., 2008; Lee et al., 2009a, 2009b) Observation of intermixing and shape changes during the growth of InAs QDs has been reported; (Garcia et al., 1997) and growth of self-organized InGaAs QRs on GaAs substrate was proposed by Lorke et al. (2001).This process starts with growth of QDs capped by a thin GaAs layer. Then a short annealing process is performed, which is the critical step for transforming QDs to QRs. It is also reported that the ring morphology is preserved even after the growth of cladding layers on top of InGaAs islands. Utilizing this process, a number of QR detectors, mainly sensitive to terahertz, has been recently demonstrated (Huang et al., 2009; Bhowmick et al., 2010; Dai et al., 2008; Lee et al., 2009a, 2009b). The QRs can be incorporated into device structures, just like QDs in QDIP structures, in which the electronic transitions from confined energy states in QRs lead to the detection of infrared radiation. Dai et al. reported a terahertz QRIP17 sensitive in the 3–100 THz range with a peak responsivity of 127 mA W^{-1} at 23 μm (detectivity of 2.3×10^{11} cm-Hz$^{1/2}$ W^{-1}) at 10 K. This work was followed by the demonstration of another terahertz QRIP by the same authors (Lee et al., 2009a, 2009b). This detector exhibits three peaks at 7.1, 3.5, and 2.3 THz (42, 85, and 130 μm, respectively) with the lowest frequency

response peak showing a cut-off of 1.7 THz (175 μm). Electronic transitions, leading to the three peaks, are from the ground state in QRs to the continuum (first peak) and to two subbands (second and third peaks). Through analysis, it is shown that the observed spectral characteristics are due to QRs, but not due to conventional QDs, which proves the existence of QRs. This detector also showed a BLIP temperature of 50 K. In a recent article, Mahdi et al. (2013) presented a theoretical work on modeling QRIP detectors, calculating their absorption, responsivity, and dark current characteristics. Electronic energy states and wavefunctions are numerically calculated using effective mass approximation and intersubband absorption coefficient of QRs is obtained. A clear dependence of spectral characteristic on QR size, described by the height, inner diameter, and outer diameter, has been observed, providing various design options of QRs for covering the terahertz spectrum.

In the work reported by Huang et al. (2009) a tunnel QR detector sensitive to terahertz radiation in the 3–8 THz range up to 120 K is demonstrated. The height, inner diameter, and outer diameter of QRs are approximately 2–4, 50, and 80 nm, respectively. The detection mechanism is exactly same as that in a TQDIP structure (illustrated in **Figure 47**) and it involves transition of electrons from the top-most QR state to the resonant state. As reported (Huang et al., 2009), the detector showed low dark current density values ($\sim 5 \times 10^{-5}$, 4.7×10^{-2} and 3.5×10^{-1} Å cm^{-2} under a -1 V bias, at 4.2, 80 and 300 K, respectively). Three prominent response peaks were observed at ~ 6.5, 10, and 12.5 THz up to 120 K. The detectivity values for the 10 THz response peak at 5 and 80 K were 4.9×10^{9} and 9.5×10^{7} Jones, respectively, at a bias of -2 V. A similar QRIP, but without using double-barriers, is reported by Lee et al. (2009a, 2009b) with a threshold at 1.7 THz (175 μm). Three response peaks at 7.1 THz (42 μm). 3.5 THz (85 μm), and 2.3 THz (130 μm) due to bound-to-continuum and bound-to-bound electronic transitions in QRs have been observed at 8 K with a BLIP temperature of 50 K. A detectivity of 1.3×10^{7} Jones has been reported at 1.7 THz and 80 K.

Followed by the work by Huang et al., Bhowmick et al. (Bhowmick et al., 2010) have reported a terahertz QRIP based on intersubband electronic transitions in small QRs. With small QRs, the top most energy state was pushed close enough to the edge of the GaAs barrier to achieve terahertz detection at 1.82 THz. This is the lowest frequency (longest wavelength) among all the terahertz detectors discussed in this article. This detector containing multiple QR layers was grown by MBE on semi-insulating (001) GaAs substrates. The growth parameters for the initial InAs QDs and the anneal conditions to convert them to QRs were carefully tuned to produce the desired smaller size of these nanostructures. First, a 0.8 μm GaAs buffer layer was grown at 600 °C. The substrate temperature was then lowered to 530 °C and 2.1 monolayers of InAs was deposited at a rate of 0.08 monolayer s^{-1}. Self-organized QDs were formed following the growth of 1.8 monolayers of InAs wetting layer. A 10 Å AlAs cap layer was grown on the InAs islands at 530 °C. Growth was interrupted and the capped islands were annealed at 580 °C for 30 s under an As$_2$ flux to form QRs. The function of the AlAs layer was to reduce the surface mobility of group III atoms on the AlAs surface, since AlAs has a higher bonding strength than GaAs. Consequently, the ring shape is better preserved during the annealing process. The complete detector heterostructure, as shown in **Figure 50(a)**, consists of 10 QR layers grown and formed under the conditions described above. The 50 nm GaAs barrier layers shown in this figure are grown immediately after the formation of the QRs. A single Al$_{0.2}$Ga$_{0.8}$As barrier is inserted at the top to reduce the dark current without substantially affecting the photocurrent. In **Figure 50(b)**, an AFM image of small QRs is shown. It was estimated that the density of the rings is 10 times 10 cm^{-2} and the rings have a height in the range of 1.2–1.5 nm and inner and outer radii of 25 and 40 nm, respectively.

Carrier confinement in the rings primarily results from their width and height. With the dimensions considered, there is only one bound state in the potential well which is also the ground state. Then, the transition energy from the ground state to the continuum in the ring corresponds to the frequency range of 1–3 THz. It is important to note that a single confined state in QRs can be obtained only if they are made small. The measured dark current characteristics for this detector at 4.2 K and 80 K are shown in **Figure 51(a)**, while the dark current density values observed here can be considered extremely low ($\sim 10^{-8}$ Å cm^{-2} and 10^{-6} Å cm^{-2} at 4.2 K for bias of -2 V and $+2$ V, respectively). The calibrated spectral response of this terahertz QRIP at 5.3 K and 10 K is also shown in **Figure 51(b)**. The peak at 1.82 THz (165 μm) corresponds to an energy of 7.52 meV, which agrees well with the calculated ground state-to-continuum transition energy for a ring with height of 1.25 nm. It is reported that the peak external quantum efficiencies (internal quantum efficiency gain) are ~ 15 and $\sim 19\%$ at -1 and 1 V bias values, respectively. Moreover,

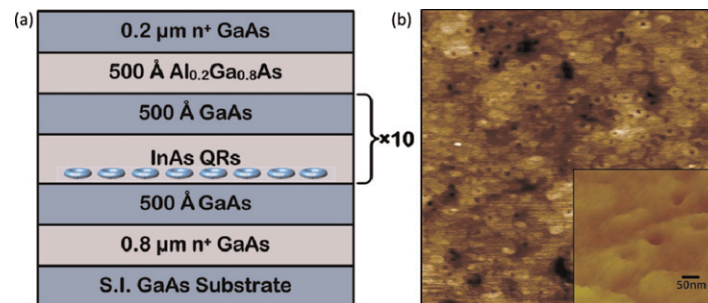**Figure 50** (a) Heterostructure of the terahertz QRIP grown by MBE. It has 10 layers of InAs quantum rings in the active region and a single Al$_{0.2}$Ga$_{0.8}$As barrier at the top. (b) AFM image of InAs quantum rings formed by post-epitaxy thermal annealing of quantum dots. Inset shows a magnified image and dimensions. Modified After Reference Bhowmick et al. (2010).
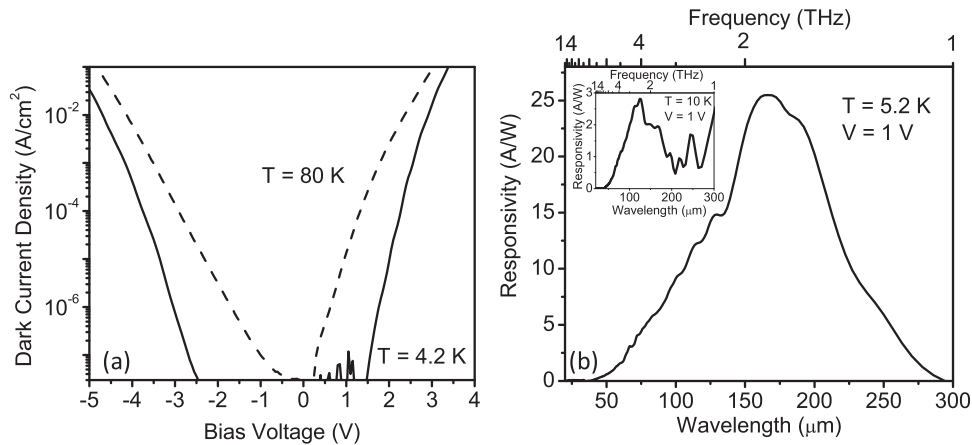
Figure 51   (a) dark current characteristics and (b) measured spectral responsivity of the terahertz QRIP at 5.2 K under 1 V bias (inset shows the responsivity at 10 K under 1 V bias). Modified After Reference Bhowmick *et al.* (2010).
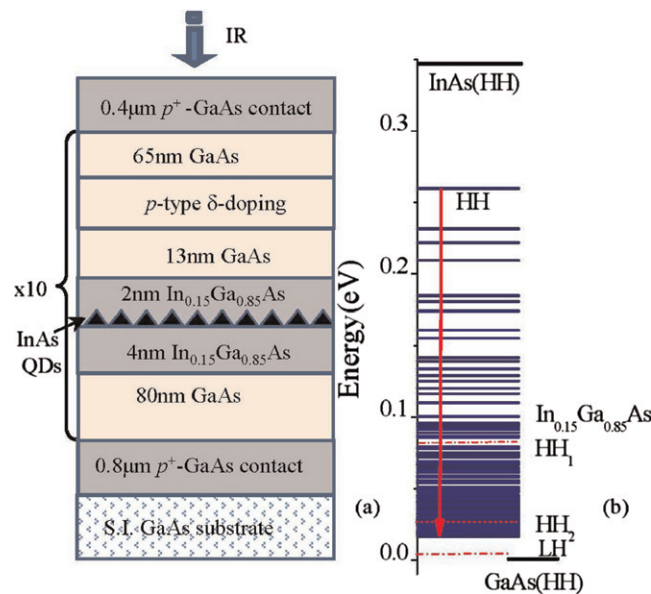

Figure 52   (a) Schematic diagram for *p*-type DWELL structure of InAs QDs embedded in $In_{015}Ga_{as5}As$ QW. (b) QD valence band structure calculated with an eight-band $k \cdot p$ model and the QW states are computed using effective mass method. The spin orbital split-off energy (SO) levels are intentionally omitted for the reason that transitions to SO levels falls in short wavelength region which are not our primary focus. The dashed lines are the two HH and LH states for $In_{0.15}Ga_{0.85}As$ QW. Transitions can be either from bound to bound or from bound to quasi-bound (or continuum) energy level. The MIR absorption is due to transition from ground state to continuum state while the THz transitions are possibly from bound to quasi-bound or continuum states. After reference Wolde *et al.* (2014).

the values of specific detectivity at a bias of 1 V are 1×10^{16} and 3×10^{15} Jones at 5.2 K and 10 K, respectively. These values of detectivity, which are higher than the detectivity of bolometers (10^{14} Jones), prove that QR detectors are another alternative for terahertz detectors, especially where detection at a specific terahertz frequency is required.

4.6   High temperature terahertz response in a p-type quantum dot-in-well photodetector

Most of the THz investigations thus far have been with *n*-type QDIP and used resonant tunneling (Su *et al.*, 2006) or dark current blocking layers (Barve *et al.*, 2011). These have been already discussed before (Su *et al.*, 2006; Huang *et al.*, 2009). So far, little or no attention has been paid to p-type DWELL structures responding in the THz region.

The detector structure shown in **Figure 52(a)** is grown by molecular beam epitaxy (MBE), consists of 10 stacks of DWELL structures sandwiched between two highly doped p^+-GaAs contact layers, grown on a semi-insulating GaAs substrate (Wolde *et al.*, 2014). The active region contains InAs QDs placed in 6 nm thick $In_{0.15}Ga_{0.85}As$ QW which in turn is surrounded by GaAs barrier
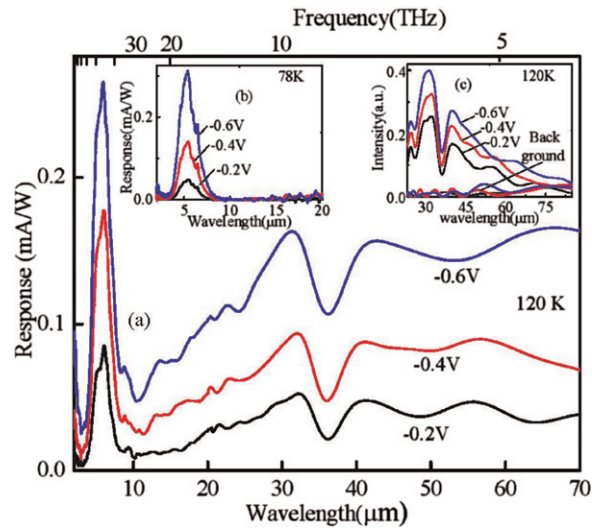
Figure 53 (a) Responsivity versus wavelength measured at $T=120$ K for three different bias values. (b) Response versus wavelength measured at $T=78$ K. This response is due to the transitions from ground state of QD to states near the GaAs band edge. Unlike the response spectra of (a), (b) has only one peak in MIR region. There are no low energy transitions or THz response at 78 K. (c) Comparison of raw data of THz response and background noise level. The THz response spectra is broad and extends beyond ~70 μm. The lower energy response (lower than 17.7 meV or ~70 μm) is below back ground noise level. After reference Wolde *et al.* (2014).

layers. The dot density is about 5×10^{10} cm^{-2}. A δ-doping technique is used, with a sheet density of 5×10^{11} cm^{-2} p-type dopants placed above the QWs, (with a 13 nm thick GaAs spacer) which introduce about 10 free holes in each QD. The QDs have nearly pyramidal shape with the average base widths of ~20–25 nm and height of ~5 nm (Krishna *et al.,* 2003).

The spectral responses were measured over temperature range from 78 to 130 K. The 5.4 μm (0.230 eV) peak corresponds to hole transition from the ground state of QD to states near the GaAs barrier. At 78 K, holes lie in the ground states which lead to the main response peak in the MIR range. The elevated temperature results in the broadening of Fermi distribution function and more carriers occupying the upper energy states where the energy spacing is in the order of THz energy range. Hence the corresponding bound-to-continuum or quasi bound transition results in THz response and increase with temperature. **Figure 53(a)** shows clearly the comparison of MIR and THz responses at three different bias values. The THz response spectra start to appear for temperatures higher than ~100 K, which is featured with a broad spectral range over ~70 μm. Although, detection of terahertz radiation up to 1 THz could be expected due to closely spaced upper energy states, the background noise level due to high dark current dominates the photocurrent at wavelength higher than 70 μm as shown in **Figure 53(c)**.

Variation of MIR and THz response spectra with temperature at a fixed applied bias of -0.4 V (or field of ~1.89 kV cm^{-1}) is shown in **Figure 54**. The THz response increases with increasing temperature which contrasts with decreasing MIR peak at higher temperatures. For a temperature increase from 80 to ~90 K, the response increases reaching the highest response at ~90 K. In QD holes are confined due to energy quantization in all three dimensions and electron-hole scattering is greatly reduced (Kochman *et al.,* 2003). Since the intersubband energy between ground state and continuum is larger than phonon energy, the optical phonon emission is not allowed. As a result, the hole relaxation time from the continuum states increases due to phonon bottle neck19. This increase in response with the temperature may be related to reduced relaxation of carries back to QD from the continuum states4 and to enhanced escape of excited carriers. As the temperature is further increased, due to decrease in carrier concentration of ground state and increase carrier population in excited states, MIR response starts to decrease and THz response starts to appear. In the temperature ranges (~100 to 130 K) where we see the THz response, MIR response decreases with increasing temperature.

The specific detectivity (D^*) is calculated from the measured peak responsivity R_p and the noise density spectra in at different temperature and bias voltage using the relation $D^* = R_p \sqrt{A \times \Delta f}/i_n$, where A is the detector area and Δf is the frequency band width. The dark current noise density in was measured with low-noise voltage preamplifiers and a SRS 760 fast Fourier transform spectrum analyzer. The value of D^* calculated for 5.4 μm absorption peak is 1.3×10^9 Jones at 78 K (-0.8 V bias) and 2.7×10^5 Jones at 130 K (-0.4 V bias). At 9.2 THz absorption peak, 130 K, and -0.4 V, the D^* value is 1.4×10^6 Jones. Significant improvement can be achieved by using a double barrier resonant tunneling heterostructure which suppress most of the dark current without blocking the photocurrent.

The low dark current enhances detectivity and operates at high temperatures. Optimization of the number and density of QDs will also enhance the absorption. The other concern regarding p-type carriers is lower mobility as compared to electrons. Since the dot layer is thinner, the hole mobility is mainly depend on the GaAs barrier. Optimizing thickness of the GaAs barrier between the dot layers can prevent multiple defects throughout the structure and enhance the photocurrent.
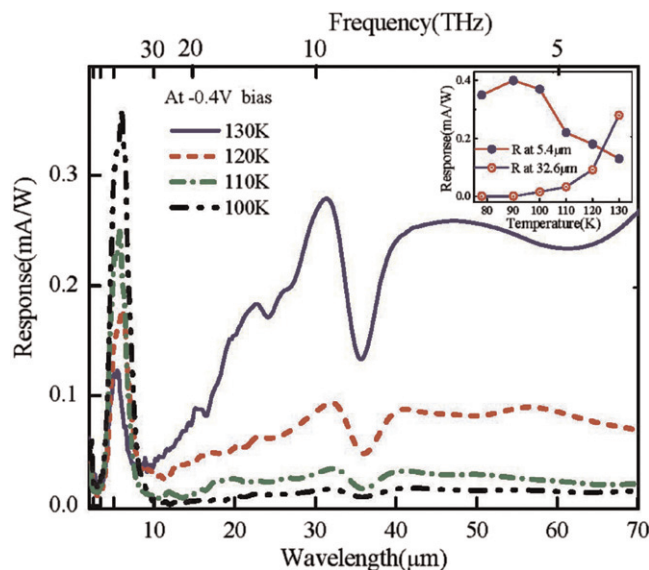
Figure 54   The variation of MIR and THz response spectra with temperature at a fixed applied bias of -0.4 V. As the temperature increases, carriers are excited to higher levels reducing the rate of transitions that give rise to MIR response whereas it enhances lower energy transitions or THz responses. The inset shows comparison of MIR and THz responses variation with temperature. After reference Wolde *et al.* (2014).

5   Antenna-Coupled Terahertz Detectors

When a photoconducting dipole antenna is struck by a fast optical pulse, the antenna radiates an electrical pulse at terahertz frequency. This phenomena has been studied (Mizuno *et al.*, 1977; Smith *et al.*, 1988; Mourou *et al.*, 1981; Heidemann *et al.*, 1983; Auston *et al.*, 1984; DeFonzo and Lutz, 1987) for some time, leading to the development of terahertz time domain spectroscopy (THz-TDS) (Hu and Nuss, 1995; Schmuttenmaer, 2004), which is used in many biological and medical (Siegel, 2004), material characterization (Grischkowsky *et al.*, 1990; Nuss *et al.*, 1991; Pedersen and Keiding, 1992) and gas sensing applications (Mittleman *et al.*, 1998; Harde and Grischkowsky, 1991; Lu *et al.*, 2008). In THz-TDS, optically gated (Hu and Nuss, 1995) two similar antenna coupled photoconductors are used as the terahertz emitter and the detector except for the metallized titanium-gold antenna of the emitter is replaced by a metallized aluminum antenna in the detector. This technique leads to excellent noise rejection. Also, with this technique the amplitude and the phase of the transient electric field is measured, allowing the complete complex-permittivity of the sample to be obtained without having to carry out a Kramers–Kronig analysis.

The uses of photoconductive dipole antennas for generating and detecting a terahertz electrical pulse was reported by Smith *et al.* (1988). The three major parts in this antenna structure are the dipole antenna, the photoconductor, and the coplanar stripline connecting the dipole/photoconductor to the contact pads. The speed and sensitivity of an antenna are determined (Smith *et al.*, 1988) by three factors: (1) the antenna geometry, (2) the photoconductor, and (3) the optical pulse duration. The photoconductor, which is biased by applying a voltage across the contact pads, is excited with an above-bandgap laser pulse to generate carriers in the CB. The applied bias accelerates these carriers, leading to an electrical pulse, which is fed into the dipole antenna, resulting in terahertz radiation emission. When the THz pulses reach the detector, a photocurrent in the detector dipole is generated and collected at the contact pads. During the optical response measurement, the radiated pulse by the emitter was allowed to propagate through the air to the detector located a few millimeters away. The photoconductor in the antenna used for the detector was illuminated by a delayed optical pulse to gate the received signal. The temporal data were Fourier transformed to obtain the frequency domain spectra. Three antennas having different dipole lengths showed resonance peaks in 0.3–0.5 THz.

Hu and Nuss (1995) have reported a terahertz imaging system in which the photoconducting emitter was made of two strip lines spaced by 50 μm fabricated on a semi-insulating GaAs substrate, while the detector is a dipole antenna with a 50 μm length fabricated on a radiation-damaged silicon-sapphire substrate. Although these photoconductive antenna based terahertz spectroscopic systems have many advantages such as low response times and room temperature operation, the major problem is the low sensitivity of the emitter and the receiver, requiring a very strong terahertz signal. In addition, these systems are bulky compared to other semiconductor based detector systems and cannot be easily integrated into a solid state system. Also, the detector should be optically gated in order to obtain a high signal-to-noise ratio. Hence, this type of a system is suitable only for specific applications. However, the use of antennas to develop source-independent terahertz detectors are being studied (Cates *et al.*, 1998).

6 Other Approaches

In addition to the device structures and concepts discussed before, currently several other concepts are being explored as potential approaches for terahertz detection. One of the approaches is based on the free hole transitions between heavy-/light-hole bands and the split-off (SP) band in a p-type doped HEIWIP structure. Recently, room temperature detection in the 3–5 μm region using the spin SP transitions was reported (Jayaweera et al., 2008; Perera and Matsik, 2008; Matsik et al., 2009) for a p-doped GaAs/AlGaAs HEIWIP structure. Extending this idea, it should be possible to use a material system such as p-GaN, which has a SP energy of 20 meV (62 μm. 4.2 THz), to develop a terahertz detector with a response threshold of 4.2 THz. Using the model reported by Matsik et al. (2009), preliminary calculations (Perera et al., 2009) indicates that p-type GaN/AlGaN SP band detector responds up to 4.2 THz. A preliminary structure and the calculated responsivity are shown in **Figure 55(a)** and **(b)**, respectively.
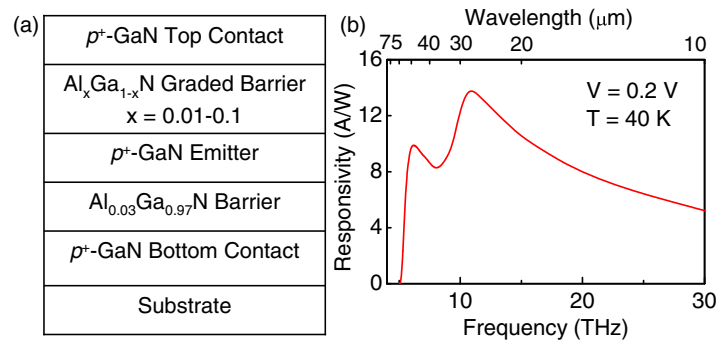

Figure 55 (a) Schematic diagram of a preliminary structure of a GaN/AlGaN split-off band detector. The thickness of the emitter and barrier layers are 20 and 400 nm, respectively. The doping concentration of the emitter and contact layers is 1×10^{19} cm^{-3}. (b) Theoretically predicted response based on the model reported by Matsik et al. (2009). The threshold at 4.2 THz (62 μm) corresponds to the split-off energy($\sim$20 meV) of p-GaN.
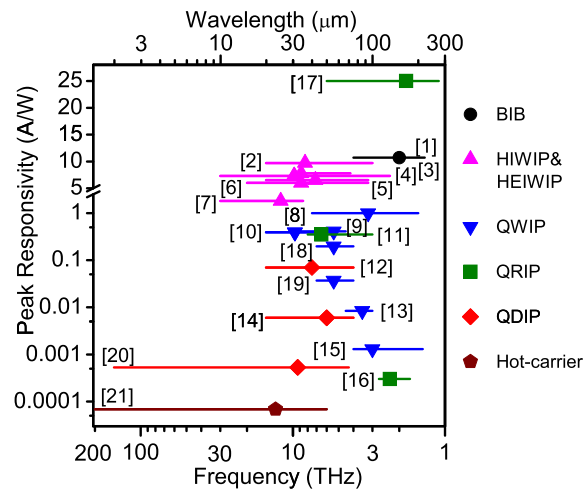

Figure 56 A summary of the response for different terahertz detectors, indicating the current status of terahertz detection capabilities. The vertical axis gives the peak responsivity for each detector. The horizontal solid lines represent the response range (ends corresponding to zero response threshold), while the symbols represent the peak response frequency/wavelength. For example, the Ge:Ga BIB (labeled by [1]) shows a response in the 4–1.36 THz range with a peak responsivity of 10.7 Å W^{-1} at 2 THz. BIB, HIWIP/HEIWIP, QWIP, QRIP, and QDIP detectors are distinguished by different symbols. The detectors used in this figure are listed below with their operating temperature (the temperature which the data in this figure was reported at, T), reported maximum operating temperature (T_{max}), and BLIP temperature(T_{BLIP}). [1]: Ge:Ga BIB (T=1.7 K), Watson et al. (1993); [2]: p-GaSb-HIWIP (T=4.9 K, T_{max}=15 K), Jayaweera et al. (2007); [3]: p-GaAs HIWIP (T=4.2 K), Esaev et al. (2004b); [4]: p-AlGaAs HEIWIP (T=4.8 K, T_{BLIP}=20 K), Rinzan et al. (2005b); [5]: n-GaAs HEIWIP (T=6 K, T_{max}=25 K), Weerasekara et al. (2007); [6]: p-GaAs HEIWIP (T=4.2 K), Matsik et al. (2003); [7]: p-Si HIWIP (T=4.6 K, T_{BLIP}=25 K, Tmax=30 K), Ariyawansa et al. (2006b); [8]: QWIP (T=8 K, T_{BLIP}=12 K), Luo et al. (2005); [9]: QWIP (T=8 K, T_{BLIP}=13 K), Luo et al. (2005); [10]: QWIP (T=8 K, T_{BLIP}=17 K), Luo et al. (2005); [11]: QRIP (T=4.2 K, T_{max}=80 K), Huang et al. (2009); [12]: QDIP (T=80 K, T_{max}=120 K), Huang et al. (2008); [13]: QCL-like QWIP (T=10 K, T_{max}=50 K), Graf et al. (2004); [14]: T-QDIP (T=80 K, T_{max}=150 K), Su et al. (2005); [15]: QWIP (T=3 K), Patrashin, and Hosako, I. (2008); [16]: QRIP (T=8 K, T_{BLIP}=50 K), Lee et al. (2009a, 2009b); [17]: QRIP (T=5.2 K, T_{max}=10 K), Bhowmick et al. (2010); [18]: QWIP (T=4.2 K), Zhang et al. (2011); [19]: QWIP (T=3.6 K), Zhang et al. (2014); [20]: QDIP (T=130 K, Tmax=10 K) Wolde et al. (2014); [21]: Hot-carrier detector (T=130 K, T_{max}=130 K), Lao et al. (2014).

Moreover, it should be mentioned that other possible approaches such as carbon nano-tubes (Rosenau da Costa et al., 2009; Fu et al., 2008; He et al., 2014; Rinzan et al., 2012; Kawano et al., 2008), graphene (Tredicucci and Vitiello, 2014; Ryzhii et al., 2014a, b) and the use of surface plasmon oscillations (Xu et al., 2008) have also attracted attention recently. With all of these interesting approaches and concepts, a revolutionary development in terahertz technology could not be far too long.

7   Conclusion

A schematic diagram indicating the spectral response ranges and the peak responsivity values of the terahertz detector structures (BIB, HIWIP, HEIWIP, QWIP, QRIP, and QDIP) discussed in this chapter is shown in **Figure 56**. In this figure, the solid lines represent the full response frequency/wavelength ranges for each detector, while the peak response frequencies/wavelengths are indicated by the symbols. The Ge:Ga BIB detector having a threshold frequency of 1.36 THz was reported by Watson et al. (1993). Terahertz QWIPs are based on the work reported by Luo et al. (2005), Graf et al. (2004) and Patrashin and Hosako (2008). QDIP data is based on the work reported by Su et al. (2006) and Huang et al. (2008), whereas QRIPs are from Huang et al. (2009), Lee et al. (2009a, 2009b). An AlGaAs emitter based terahertz HEIWIP detector, which has a threshold of 2.3 THz (128 μm), was reported by Rinzan et al. (2005b). Other HIWIPs and HEIWIPs are based on the work reported by Jayaweera et al. (2007), Esaev et al. (2004b), Weerasekara et al. (2007), Matsik et al. (2003), and Ariyawansa et al. (2006b).

In conclusion, BIB detectors have reported the shortest peak frequency ($\sim$2 THz), while both QWIPs and BIB detectors have shown similar frequency thresholds ($\sim$1.4 THz). However, one of the drawbacks associated with BIB detectors is that they require very high quality materials in the barrier in order to achieve the best performance. Also, BIB detectors' response frequency range is material specific unlike other detectors. AlGaAs/GaAs HEIWIP detectors have shown a broad response with a threshold at 2.3 THz. While QWIP, BIB, and HEIWIP detectors operate at low temperatures (below 15 K), QDIPs have shown higher operating temperatures, however, QDIPs' peak wavelengths and the wavelength thresholds are shorter than those of QWIP and HEIWIP detectors. A QRIP has reported the highest BLIP temperature (50 K) for a peak at 2.3 THz. Although photoconductive antenna detectors/emitters are fast and operates at room temperature in the terahertz region, they should be optically gated in order to obtain a high signal-to-noise ratio.

The overall work reported in this chapter indicates that there is a strong interest and a potential for terahertz detector development. However, most of the terahertz detectors have efficiencies of the order of 3–5% and operate at cryogenic temperatures. Although specific applications require specific conditions on the performance, the focus for future terahertz detectors should be to explore methods for improving absorption to increase the efficiency, while reducing the dark current, in order to increase the BLIP temperature.

Acknowledgment

References

Amtout, A., Raghavan, S., Rotella, P., et al., 2004. Theoretical modeling and experimental charactorization of InAs/InGaAs quantum dots in a well detector. Journal of Applied Physics 96, 3782–3786.

Anemogiannis, E., Glytsis, E.N., Member, S., Gaylord, T.K., 1997. Quasi-bound states determination using a perturbed wavenumbers method in a large quantum box. IEEE Journal of Quantum Electronics 33, 742–752.

Ariyawansa, G., Apalkov, V., Perera, A.G.U., et al., 2008. Bias-selectable tricolor tunneling quantum dot infrared photode-tector for atmospheric windows. Applied Physics Letters 92, 111104–111304.

Ariyawansa, G., Perera, A.G.U., Raghavan, G.S., et al., 2005a. Effect of well width on three color quantum dots-in-a-well infrared detectors. IEEE Photonics Technology Letters 17, 1064–1066.

Ariyawansa, G., Rinzan, M.B.M., Esaev, D.G., et al., 2005b. Near- and far- infrared p-GaAs dual-band detector. Applied Physics Letters 86, 143510–143513.

Ariyawansa, G., Rinzan, M.B.M., et al., 2006a. GaN/AlGaN ultraviolet/infrared dual-band detector. Applied Physics Letters 89, 091113.

Ariyawansa, G., Rinzan, M.B.M., Matsik, S.G., et al., 2006b. Characteristics of a Si dual-band detector responding in both near- and very-long-wavelength-infrared regions. Applied Physics Letters 89, 061112–061113.

Ariyawansa, G., Rinzan, M.B.M., Strassburg, M., et al., 2006c. GaN/AlGaN heterojunction infrared detector responding in 8−14 and 20−70 μm ranges. Applied Physics Letters 89, 141122–141123.

Aslan, B., Liu, H.C., Korkusinski, M., Cheng, S.J., Hawrylak, P., 2003. Response spectra from mid- to far-infrared, polarization behaviors, and effects of electron numbers in quantum-dot photodetectors. Applied Physics Letters 82, 630–632.

Auston, D.H., Cheung, K.P., Smith, P.R., 1984. Picosecond photoconducting Hertzian dipoles. Applied Physics Letters 45, 284–286.

Bandara, K.M.S.V., Choe, J.W., Francombe, M.H., Perera, A.G.U., Lin, Y.F., 1992. GaAs/AlGaAs superlattice miniband detector with 14.5 μm peak response. Applied Physics Letters 60, 3022–3024.

Bandaru, J., Beeman, J.W., Haller, EE., Samperi, S., Haegel, N.M., 2002. Influence of the Sb dopant distribution on far infrared photoconductivity in Ge:Sb blocked impurity band detectors. Infrared Physics & Technology 43, 353–360.

Barve, A.V., Sengupta, S., Kim, J.O., et al., 2011. Confinement enhancing barriers for high performance quantum dots-in-a-well infrared detectors. Applied Physics Letters 99, 191110.

Beeler, M., Bougerol, C., Bellet-Amalaric, E., Monroy, E., 2014. THz intersubband transitions in AlGaN/GaN multi-quantum-wells. Physica Status Solidi A 211 (4), 761.

Beeman, J.W., Goyal, S., Reichertz, L.A., Haller, E.E., 2007. Ion-implanted Ge:B far-infrared blocked-impurity-band detectors. Infrared Physics & Technology 51, 60–65.

Belkin, M.A., Capasso, F., Xie, F., et al., 2008. Room temperature terahertz quantum cascade laser source based on intracavity difference-frequency generation. Applied Physics Letters 92, 201101–201103.

Bhattacharya, P., Su, X.H., Chakrabarti, S., Ariyawansa, G., Perera, A.G.U., 2005. Characteristics of a tunneling quantum-dot infrared photodetector operating at room temperature. Applied Physics Letters 86, 191106–191107.

Bhowmick, S., Huang, G., Guo, W., et al., 2010. High-performance quantum ring detector for the 1 – 3 terahertz range. Applied Physics Letters 96, 231103.

Blakemore, J.S., 1982. Semiconducting and other major properties of gallium arsenide. Journal of Applied Physics 53, R123–R181.

Califano, M., Harrison, P., 2000. Presentation and experimental validation of a single-band, constant-potential model for self-assembled InAs/GaAs quantum dots. Physical Review B 61, 10959–10965.

Cao, J.C., Liu, H.C., 2011. In: David, R. Rhiger, Gunapala, Sarath, D., Chennupati, Jagadish (Eds.), Semiconductors and Semimetals, vol. 84. Elsevier, p. 195.

Cardozo, B.L., Reichertz, L.A., Beeman, J.W., Haller, E.E., 2005. Characterization of liquid phase epitaxial GaAs for blocked-impurity-band far-infrared detectors. Infrared Physics & Technology 46, 400–407.

Carr, G.L, Michael, Martin, , Wayne, C., Mckinney, R., Jordan, K., George Neil, R., Williams, G.P., 2002. High-power terahertz radiation from relativistic electrons. Nature 420, 153.

Cates, C.L., Briceno, G., Sherwin, M.S., et al., 1998. A concept for a tunable antenna-coupled intersubband terahertz (TACIT) detector. Physica E 2, 463–467.

Cha, D., Ogawa, M., Chen, C., et al., 2007. Intersubband absorption in p-type $Si_{1-x}Ge_x$ quantum dots on pre-patterned Si substrates made by a diblock copolymer process. Journal of Crystal Growth 301302, 833–836.

Chakrabarti, S., Stiff-Roberts, A.D., Su, X., et al., 2005. High Performance mid-infrared quantum dot infrared pho-todetectors. Journal of Physics D 38, 2135–2141.

Cheah, C.W., Tan, L.S., Karunasiri, G., 2002. Application of analytical k.p model with envelope function approximation to intersubband transitions in n-type III–V semiconductor Gamma quantum wells. Journal of Applied Physics 91, 51055115.

Chen, Y., Liu, H., Deng, Y., et al., 2004. THz spectroscopic investigation of 2,4-dinitrotoluene. Chemical Physics Letters 400, 357–361.

Choi, K.K., 1997. The Physics of Quantum Well Infrared Photodetectors. Singapore: World Scientific.

Colson, W.B., Johnson, E.D., Kelley, M.J., Schwettman, H.A., 2002. Putting free-electron lasers to work. Physics Today 55, 35–41.

Coon, D.D., Karunasiri, R.P.G., 1984. New mode of ir detection using quantum wells. Applied Physics Letters 45, 649–651.

Coon, D.D., Karunasiri, R.P.G., Liu, H.C., 1986. Fast response qwantum well photodetectors. Journal of Applied Physics 60, 2636–2638.

Dai, J.H., Lee, J.H. Lin, Y.L., Lee, S.C., 2008. In(Ga)As quantum rings for terahertz detectors. Japnese Journal of Applied Physics 47, 2924.

Defonzo, A.P., Lutz, C.R., 1987. Optoelectronic transmission and reception of ultrashort electrical pulses. Applied Physics Letters 51, 212–214.

Dexheimer, S.L., 2007. Terahertz Spectroscopy: Principles and Applications. Boca Raton, FL: CRC.

Doyennette, L., Vardi, A., Guillot, F., et al., 2006. GaN/AIN quantum dot photodetectors at 1.3–1.5 μm. Superlattices and Microstructures 40, 262–267.

Dumke, W.P., 1983. Band-gap narrowing from luminescence in p-type Si. Journal of Applied Physics 54, 3200–3202.

Ershov, M., Liu, H.C., 1999. Low-frequency noise gain and photocurrent gain in quantum well infrared photodetectors. Journal of Applied Physics 86, 6580–6585.

Esaev, D.G., Rinzan, M.B.M., Matsik, S.G., Perera, A.G.U., 2004a. Design and optimization of GaAs/AlGaAs heterojunction infrared detectors. Journal of Applied Physics 96, 4588–4597.

Esaev, D.G., Rinzan, M.B.M., Matsik, S.G., et al., 2004b. High performance single emitter homojunction interfacial work function far infrared detectors. Journal of Applied Physics 95, 512–519.

Escher, J.S., 1981. In: Willardson, R.K, Beer, A.C (Eds.), Semiconductors and Semimetals. New York: Academic Press, p. 195.

Etteh, N.E.I., Harrison, P., 2002. First principles calculations ofthe dark current in quantum well infrared photodetectors. Physica E 13, 381–384.

Feng, X., Xu-Guang, G., Jun-Cheng, C., 2008. Simulation of photocurrents of terahertz quantum-well photodetectors. Chinese Physics Letters 25, 1895–1897.

Fu, K., Zannoni, R., Chan, C., et al., 2008. Terahertz detection in single wall carbon nanotubes. Applied Physics Letters 92, 033105–033106.

Furdyna, J.K., 1988. Diluted magnetic semiconductors. Journal of Applied Physics 64, R29–R64.

Garcia, J.M., Medeiros-Ribeiro, G., Schmidt, K., et al., 1997. Intermixing and shape changes during the formation of InAs self-assembled quantum dots. Applied Physics Letters 71 (14), 2014.

Graf, M., Scalari, G., Hofstetter, D., Faist, , et al., 2004. Terahertz range quantum well infrared photodetector. Applied Physics Letters 84, 475–477.

Grischkowsky, D., Keiding, S., Exter, M.V., Fattinger, C., 1990. Far-infrared time-domain spectroscopy with terahertz beams of dielectrics and semiconductors. Journal of Optics Society of America B 7, 2006–2015.

Gu, L.L., Zhang, R., Tan, Z.Y., et al., 2014. Terahertz quantum well photo-detectors: grating versus 45facet coupling. Journal of Physics D: Applied Physics 47 (16), 165101.

Gunapala, S.D., Bandara, K.M.S., 1995. In: Francombe, M.H., Vossen, J.L. (Eds.), Recent Developments in Quantum-Well Infrared Photodetectors. New York: Academic Press, pp. 114–232.

Gunapala, S.D., Bandara, K.M.S.V., Levine, B.F., et al., 1994. Very long wavelength $In_xGa_{1-x}As$/GaAs quantum well infrared photodetectors. Applied Physics Letters 64, 2288–2290.

Gunapala, S.D., Bandara, S.V., Hill, C.J., et al., 2007a. Demonstration of 640×512 pixels long-wavelength infrared (LWIR) quantum dot infrared photodetector (QDIP) imaging focal plane array. Infrared Physics & Technology 50, 149–155.

Gunapala, S.D., Bandara, S.V., Liu, J.K., et al., 2007b. Towards dualband megapixel QWIP focal plane arrays. Infrared Physics & Technology 50, 217–226.

Gunapala, S.D., Bandara, S.V., Liu, J.K., et al., 2003. 640×512 Pixel Four-Band, Broadband, and Narrowband Quantum Well Infrared Photodetector Focal Plane Arrays. Infrared Technology and Applications XXVIII, first ed. Seattle, WA: SPIE.

Guo, X.G., Cao, J.C., Zhang, R., Tan, Z.Y., Liu, H.C., 2013. recent progress in terahertz quantum-well photodetectors. IEEE Journal of Selected Topics in Quantum Electronics 19 (1), 8500508.

Guo, X.G., Tan, Z.Y., Cao, J.C., Liu, H.C., 2009. Many-body effects on terahertz quantum well detectors. Applied Physics Letters 94, 201101–201102.

Haegel, N.M., 1988. Space-charge behavior near implanted contacts on infrared detectors. Journal of Applied Physics 64, 2153–2159.

Haller, E.E., Beeman, J.W., 2002. Far Infrared Photoconductors: Recent Advances and Future Prospects. In: Proceedings of the Far-IR, Sub-mm, & Millimeter Detector Technology Workshop, NASA CP-211408, Paper 2–06.

Harde, H., Grischkowsky, D., 1991. Coherent transients excited by subpicosecond pulses of terahertz radiation. Journal of Optics Society of America B 8, 1642–1651.

Harmon, E.S., Melloch, M.R., Lundstrom, M.S., 1994. Effective band-gap shrinkage in GaAs. Applied Physics Letters 64, 502–504.

He, X.W., Fujimura, N., Lloyd, J.M., et al., 2014. Carbon nanotube terahertz detector. Nano Letters 14 (7), 3953.

Heidemann, R., Pfeiffer, T.H., Jager, D., 1983. Optoelectronically pulsed slot-line antennas. Electronics Letters. 316–317.

Hu, B.B., Nuss, M.C., 1995. Imaging with terahertz waves. Optics Letters 20, 1716.

Huang, G., Guo, W., Bhattacharya, P., Ariyawansa, G., Perera, A.G.U., 2009. A quantum ring terahertz detector with resonant tunnel barriers. Applied Physics Letters 94 (10), 101115.

Huang, G., Yang, J., Bhattacharya, P., Ariyawansa, G., Perera, A.G.U., 2008. A multicolor quantum dot intersublevel detector with photoresponse in the terahertz range. Applied Physics Letters 92, 011117–011118.

Huffman, J.E., Crouse, A.G., Halleck, B.L., Downes, T.V., Herter, T.L., 1992. Si:Sb blocked impurity band detectors for infrared astronomy. Journal of Applied Physics 72, 273–275.

Jain, S.C., Mertens, R.P., Van, R.J.O., 1991. Advances in Electronics and Electron Physics. New York: Academic.

Jain, S.C., Roulston, D.J., 1991. A simple expression for band gap narrowing (BGN) in heavily doped Si Ge GaAs and Ge_xSi_{1-x} strained layers. Solid-State Electronics 34, 453–465.

Jantsch, O., 1987. Flicker (1/f) noise generated by a random walk of electrons in interfaces. IEEE Transactions on Electronics Devices 34, 1100–1115.

Jayaweera, P.V.V., Matsik, S.G., Perera, A.G.U., et al., 2007. GaSb homojunctions for far-infrared (terahertz) detection. Applied Physics Letters 90, 111109–111309

Jayasinghe, R.C., Ariyawansa, G., Dietz, N., et al., 2008. Simultaneous detection of ultraviolet and infrared radiation in a single GaN/GaAlN heterojunction. Optics Letters 33, 2422–2424.

Jayaweera, P.V.V., Matsik, S.G., Perera, A.G.U., et al., 2008. Uncooled infrared detectors for 3–5 μm and beyond. Applied Physics Letters 93, 021105–021106.

Jhabvala, M., Choi, K., Goldberg, A.C., La, A.T., Gunapala, S.D., 2004. Development of a 1 Kx 1 K GaAs QWIP far IR imaging array. Focal Plane Arrays for Space Telescopes, first ed. San Diego, CA: SPIE.

Jia, J.Y., Cao, J.H., Hao, M.R., et al., 2014. Dark current mechanism of terahertz quantum-well photodetectors. Journal of Applied Physics 116 (15), 154501.

Jiang, H., Singh, J., 1997. Strain distribution and electronic spectra of InAs/GaAs self-assembled dots: an eight-band study. Physical Review B 56, 4696–4701.

Jiang, L., Li, S.S., Yeh, N.-T., et al., 2003. In0.6Ga0.4As/GaAs quantum-dot infrared photodetector with operating temperature up to 260 K. Applied Physics Letters 82, 1986–1988.

Kane, M.J., Millidge, S., Emeny, M.T., et al., 1992. In: Rosencher, E., Vinter, B., Levine, B.F. (Eds.), Intersubband Transitions in Quantum Wells. New York: Plenum, pp. 31–42.

Kawano, Y., Fuse, T., Toyokawa, S., Uchida, T., Ishibashi, K., 2008. Terahertz photon-assisted tunneling in carbon nanotube quantum dots. Journal of Applied Physics 103 (3), 103, 034307.

Kim, E.-T., Madhukar, A., Ye, Z., Campbell, J.C., 2004. High detectivity InAs quantum dot infrared photodetectors. Applied Physics Letters 84, 3277–3279.

Klauder, J.R., 1961. The modification of electron energy levels by impurity atoms. Annals of Physics 14, 43–76.

Klein, M.V., Furtac, T.E., 1986. Optics. New York: Wiley.

Kochman, B., Stiff-Roberts, A.D., Chakrabarti, S., et al., 2003. Absorption, carrier lifetime, and gain in InAs–GaAs quantum-dot infrared photodetectors. IEEE Journal of Quantum Electronics 39, 459–467.

Kohler, R., Tredicucci, A., Beltram, F., et al., 2002. Terahertz semiconductor-heterostructure laser. Nature 417, 156–159.

Kosonocky, W.F., 1992. State-of-art in Schottky-barrier IR image sensors. SPIE. 1685, pp. 2–19.

Kozlowski, L.J., Williams, G.M., Sullivan, G.J., et al., 1991. LWIR 128 × 128 GaAs/AlGaAs multiple quantum well hybrid focal plane array. IEEE Transactions Electronics Devices 38.pp-pp.

Krishna, S., Forman, D., Annamalai, S., et al., 2005. Demonstration of a 320 × 256 two-color focal plane array using InAs/InGaAs quantum dots in well detectors. Applied Physics Letters 86, 193501–193503.

Krishna, S., Raghavan, S., Von Winckel, G., et al., 2003. Three-color ($\lambda_{p1} \sim 3.8$, $\lambda_{p2} \sim 8.5$, and $\lambda_{p3} \sim 23.2$ μm) InAs/InGaAs quantum-dots-in-a-well detector. Applied Physics Letters 83, 2745–2747.

Lao, Y.-F., Perera, A.G.U., 2012. Temperature-dependent internal photoemission probe for band parameters. Physical Review B 86, 195315.

Lao, Y.-F., Perera, A.G.U., Li, L.H., et al., 2014.Tunable hot-carrier photodetection beyond the bandgap spectral limit. Nature Photonics 8 (5), 412–418.

Lee, J.H., Dai, J.H., Chan, C.F., Lee, S.C., 2009. In(Ga)As quantum ring terahertz photodetector with cutoff wavelength at 175 mm. IEEE Photonics Technology Letters 21 (11), 721.

Lee, J.-H., Dai, J.-H., Chan, C.-F., Lee, S.-C., 2009. In(Ga)As quantum ring terahertz photodetector with cutoff wavelength at 175 μm. IEEE Photonics Technology Letters 21, 721–723.

Lee, Y.-S., 2008. Principles of Terahertz Science and Technology. New York: Springer.

Leon, R., Swift, G.M., Magness, B., et al., 2000. Changes in luminescence emission induced by proton irradiation: InGaAs/GaAs quantum wells and quantum dots. Applied Physics Letters 76, 2074–2076.

Levine, B.F., 1993. Quantum-well infrared photodetectors. Journal of Applied Physics 74, R1–R81.

Levine, B.F., Choi, K.K., Bethea, C.G., Walker, J., Malik, R.J., 1987. New 10 μ infrared detector using intersubband absorption in resonant tunneling GaAlAs superlattices. Applied Physics Letters 50, 1092–1094.

Li, J., Choi, K.K., Tsui, D.C., 2005. Voltage-tunable four-color quantum-well infrared photodetectors. Applied Physics Letters 86, 211114–211134.

Lifshifts, T.M., Nad, F.Y., Sidorov, V.I., 1967. Sov. Solid State 8, 2567.

Lim, H., Tsao, S., Zhang, W., Razeghi, M., 2007. High-performance InAs quantum-dot infrared photodetectors grown on InP substrate operating at room temperature. Applied Physics Letters 90, 131112–131113.

Lin, C.H., Yu, C.Y., Peng, C.Y., Ho, W.S., Liu, C.W., 2007. Broadband SiGe/Si quantum dot infrared photodetectors. Journal of Applied Physics 101, 033117–033147.

Lin, T.L., Maserjian, J., 1990. Novel $Si_{1-x}Ge_x$/Si heterojunction internal photoe-mission long-wavelength infrared detectors. Applied Physics Letters 57, 1422–1424.

Lin, Y.-Y., Singh, J., 2002. Self-assembled quantum dots: a study of strain energy and intersubband transitions. Journal of Applied Physics 92, 6205–6210.

Liu, H.C., Capasso, F., 2000a. Intersubband Transition in Quantum Wells: Physics and Device Applications I (Semiconductors and Semimetals), vol. 62. San Diego: Academic Press.

Liu, H.C., Capasso, F., 2000b. Quantum Well IR Photodetector Focal Plane Arrays. San Diego: Academic Press.

Liu, H.C., Gao, M., Mccaffrey, J., Wasilewski, Z.R., Fafard, S., 2001. Quantum dot infrared photodetectors. Applied Physics Letters 78, 79–81.

Liu, H.C., Noel, -P., J., Lujian, Li Buchanan, M., Simmons, J.G., 1992. Novel infrared detector concept utilizing controlled epitaxial doping profiles. Applied Physics Letters 60, 3298–3300.

Liu, H.C., Song, C.Y.S., Thorpe, A.J., Cao, J.C., 2004. Terahertz quantum-well photodetector. Applied Physics Letters 84, 4068–4070.

Lorke, A., Luyken, R.J., Garcia, J.M., Petroff, P.M., 2001. Growth and Electronic Properties of Self-Organized Quantum Rings. Japanese Journal of Applied Physics 40, 1857.

Lu, X., Karpowicz, N., Chen, Y., Zhang, X.C., 2008. Systematic study of broadband terahertz gas sensor. Applied Physics Letters 93, 261106–261306.

Luo, H., Liu, H.C., Song, C.Y., Wasilewski, Z.R., 2005. Background-limited terahertz quantum-well photodetector. Applied Physics Letters 86, 231103–231303.

Luo, M.Y., Bosman, G., Van Der Ziel, A., Hench, L.L., 1988. Theory and experiments of 1/f noise in Schottky-barrier diodes operating in the thermionic-emission mode. IEEE Transactions on Electronics Devices 35, 1351–1356.

Lutgen, S., Kaindl, R.A., Woerner, M., et al., 1996. Nonlinear intersubband absorption of a hot quasi-two-dimensional electron plasma studied by femtosecond infrared spectroscopy. Physical Review B 54, R17343.

Mahdi, Z., Abedi, K., Karimi, M., 2013. Numerical analysis of quantum ring intersub-band photodetector for far infrared detection. Optics Quantum Electronics 1.

Maimon, S., Finkman, E., Bahir, G., 1998. Intersublevel transitions in InAs/GaAs quantum dots infrared photodetectors. Applied Physics Letters 73, 2003.

Matsik, S.G., Jayaweera, P.V.V., Jayasinghe, R.C., *et al.*, 2009. Device modeling for split-off band detectors. Journal of Applied Physics. 106, 064503. (submitted for publication).

Matsik, S.G., Rinzan, M.B.M., Esaev, D.G., *et al.*, 2004. 20 μm cutoff heterojunction interfacial work function internal photoemission detectors. Applied Physics Letters 84, 3435–3437.

Matsik, S.G., Rinzan, M.B.M., Perera, A.G.U., *et al.*, 2003. Cutoff tailorability of heterojunction terahertz detectors. Applied Physics Letters 82, 139–141.

Matthews, M.R., Steed, R.J., Frogley, M.D., *et al.*, 2007. Transient photoconductivity measurements of carrier lifetimes in an InAs/In[sub 0.15]Ga[sub 0.85]As dots-in-a-well detector. Applied Physics Letters 90, 103519–103539.

Miles, R.E., Zhang, X.-C., Eisele, H., Krotkus, A., 2007. Terahertz Frequency Detection and Identification of Materials and Objects. New York: Springer.

Mittleman, D., 2004. Sensing with Terahertz Radiation. New York: Springer.

Mittleman, D.M., Jacobsen, R.H., Neelamani, R., Baraniuk, R.G., Nuss, M.C., 1998. Gas sensing using terahertz time-domain spectroscopy. Applied Physics B: Lasers and Optics 67, 379–390.

Mizuno, K., Daiku, Y., Ono, S., 1977. Design of printed resonant antennas for monolithic-diode detectors. IEEE Transactions of Microwave Theory and Technology 25, 470–472.

Mooney, J.M., Silverman, J., 1985. The theory of hot-electron photoemission in Schottky-barrier IR detectors. IEEE Transactions of Electronics Devices 32, 33–39.

Moore, W.J., Freitas, J.A., Molnar, R.J., 1997. Zeeman spectroscopy of shallow donors in GaN. Physical Review B 56, 12073–12076.

Mourou, G., Stancampiano, C.V., Antonetti, A., Orszag, A., 1981. Picosecond microwave pulses generated with a subpicosecond laser-driven semiconductor switch. Applied Physics Letters 39, 295–296.

Murdin, B.N., Heiss, W., Langerak, C.J.G.M., *et al.*, 1997. Direct observation of the LO phonon bottleneck in wide GaAs/Al$_x$Ga$_{1-x}$As quantum wells. Physical Review B 55, 5171.

Nuss, M.C., Mankiewich, P.M., OMalley, M.L., Westerwick, E.H, Littlewood, P.B., 1991. Dynamic conductivity and coherence peak in YBa$_2$Cu$_3$O$_7$ superconductors. Physical Review Letters 66, 3305–3308.

Pal, D., Chen, L., Towe, E., 2003. Intersublevel photoresponse of (In,Ga)As/GaAs quantum-dot photodetectors: Polarization and temperature dependence. Applied Physics Letters 83, 4634–4636.

Pan, D., Towe, E., Kennerly, S., 1998. Normal-incidence intersubband (In, Ga)As/GaAs quantum dot infrared photodetectors. Applied Physics Letters 73, 1937–1939.

Patrashin, M., Hosako, I., 2008. Terahertz frontside-illuminated quantum-well photodetector. Optics Letters 33, 168–170.

Pedersen, J.E., Keiding, S., 1992. THz time-domain spectroscopy of nonpolar liquids. IEEE Journal of Quantum Electronics 28, 2518–2522.

Perera, A.G.U., 2001. Semiconductor Photoemissive Structures for Far Infrared Detection. In: Perera, A.G.U., Liu, H.C., Francombe, M.H. (Eds.), Handbook of Thin Film Devices: Semiconductor optical and Electro optical Devices. Academic Press. pp. 135–169.

Perera, A.G.U., 2007. UV-IR Dual Band Detector. U. S. Patent No. 11/585048.

Perera, A.G.U., Ariyawansa, G., Jayaweera, P.V.V., *et al.*, 2008. Semiconductor terahertz detectors and absorption enhancement using plasmons. Microelectronics Journal 39, 601–606.

Perera, A.G.U., Choe, W.J., Francombe, M.H., Sherriff, R.E., Devaty, R.P., 1993. Far infrared detection with a Si p–i interface and multilayer structures. Superlattices and Microstructures 14, 123.

Perera, A.G.U., Jayaweera, P.V.V., Matsik, S.G., 2009. THz sensors based on spin orbit split off Levels. In: Proceedings of the 34th International Conference on Infrared Millimeter, and Terahertz Waves, to be published.

Perera, A.G.U., Matsik, S.G., 2007. Heterojunction Far Infrared Detector. U. S. Patent No. 7253432.

Perera, A.G.U., Matsik, S.G., 2008. High Operating Temperature SPLIT-OFF Band Infrared Detectors. International Bureau of WIPO. U. S. Provisional Patent 11/849,464.

Perera, A.G.U., Matsik, S.G., Liu, H.C., *et al.*, 2000. GaAs/InGaAs quantum well infrared photodetector with a cutoff wavelength at 35 μm. Applied Physics Letters 77, 741–743.

Perera, A.G.U., Matsik, S.G., Rinzan, M.B.M., *et al.*, 2003. The effects of light-heavy hole transitions on the cutoff wavelengths of far infrared detectors. Infrared Physics and Technology 44, 347–353.

Perera, A.G.U., Matsik, S.G., Yaldiz, B., *et al.*, 2001. Heterojunction wavelength-tailorable far-infrared photodetectors with response out to 70 μm. Applied Physics Letters 78, 2241–2243.

Perera, A.G.U., Shen, W.Z., 1999. GaAs homojuction interfacial workfunction internal photoemission (HIWIP far-infared detectors). Opto-Electronics Review 7, 153–180.

Perera, A.G.U., Shen, W.Z., Liu, H.C., *et al.*, 1998a. Demonstration of Si homojunction far-infrared detectors. Applied Physics Letters 72, 2307–2309.

Perera, A.G.U., Shen, W.Z., Matsik, S.G., *et al.*, 1998b. GaAs/AlGaAs quantum well photodetectors with a cutoff wavelength at 28 μm. Applied Physics Letters 72, 1596–1598.

Perera, A.G.U., Sherriff, R.E., Francombe, M.H., Devaty, R.P., 1992. Far infrared photoelectric thresholds of extrinsic semiconductor photocathodes. Applied Physics Letters 60, 3168–3170.

Perera, A.G.U., Yuan, H.X., Francombe, M.H., 1995. Homojunction internal photoemission far-infrared detectors: Photoresponse performance analysis. Journal of Applied Physics 77, 915–924.

Petroff, M.D., Stapelbroek, M.G., Feb. 4, 1986. U. S. Patent No. 4,568,960.

Phillips, J., Kamath, K., Bhattacharya, P., 1998. Far-infrared photoconductivity in self-organized InAs quantum dots. Applied Physics Letters 72, 2020–2022.

Pokatilov, E.P., Fonoberov, V.A., Fomin, V.M., Devreese, J.T., 2001. Development of an eight-band theory for quantum dot heterostructures. Physical Review B 64, 245328–245344.

Pulizzi, F., Walker, D., Patane, A., *et al.*, 2005. Excited states of ring-shaped (InGa)As quantum dots in a GaAs/(AlGa)As quantum well. Physical Review B (Condensed Matter and Materials Physics) 72, 085309–085609.

Raghavan, , Rotella, P., Stintz, A., *et al.*, 2002. High-responsivity, normal-incidence long-wave infrared (p 7.2 μm) InAs/In$_{0.15}$Ga$_{0.85}$As dots-in-a-well detector. Applied Physics Letters 81, 1369–1371.

Ramian, G., 1992. The new UCSB free-electron lasers. Nuclear Instruments and Methods Physical Research Section A-Accel. Spectrom. Dect. Assoc. Equip. 318, 225–229.

Reichertz, L.A., Beeman, J.W., *et al.*, 2006. Development of a GaAs-based BIB detector for sub-mm wavelengths. Millimeter and Submillimeter Detectors and Instrumentation for Astronomy III 6275, 62751S-8.

Reichertz, L.A., Cardozo, B.L., Beeman, J.W., *et al.*, 2005. First Results on GaAs blocked impurity band (BIB) structures for far-infrared detector arrays. In: Strojnik, M. (Ed.), Infrared Spaceborne Remote Sensing. SPIE. p.58830Q1–8.

Reynolds, D.B., Seib, D.H, Stetson, S.B., *et al.*, 1989. Blocked impurity bandhybrid infraredfocal plane arrays for astronomy. IEEE Transactions Nuclear Science 36, 857–862.

Rinzan, M, Jenkins, G., Drew, H.D., Shafranjuk, S., Barbara, P., 2012. Carbon nanotube quantum dots as highly sensitive terahertz-cooled spectrometers. Nano Letters 12 (6), 3097.

Rinzan, M.B.M., Esaev, D.G., Perera, A.G.U., *et al.*, 2004. Free carrier absorption in Be doped epitaxial AlGaAs thin films. Applied Physics Letters 85, 5236–5238.

Rinzan, M.B.M., Perera, A.G.U., Matsik, S.G., 2005a. Terahertz absorption in AlGaAs films and detection using heterojunctions. Infrared Physics and Technology 47, 188–194.

Rinzan, M.B.M., Perera, A.G.U., Matsik, S.G., *et al.*, 2005b. AlGaAs emitter/GaAs barrier terahertz detector with a 2.3 THz threshold. Applied Physics Letters 86, 071112–071113.

Rogalski, A., 2003. Infrared detectors: status and trends. Progress in Quantum Electronics 27, 59–210.

Rogalski, A., 2004. Optical detectors for focal plane arrays. Opto-Electronics Review 12, 221–245.

Rogalski, A., Sizov, F., 2011. Terahertz detectors and focal plane arrays. Opto-Electronics Review 19 (3), 346.

Rosenau Da Costa, M., Kibis, O.V., Portnoi, M.E., 2009. Carbon nanotubes as a basis for terahertz emitters and detectors. Microelectronics Journal 40, 776–778.

Ryzhii, V., 1996. The theory of quantum-dot infrared phototransistors. Semiconductors Science and Technology. 759–765.

Ryzhii, V., Khmyrova, I., 2002. Terahertz photomixing in quantum well structures using resonant exitation of plasma oscillations. Journal of Applied Physics 91, 1875–1881.

Ryzhii, V., Otsuji, T., Aleshkin, V.Ya, et al., 2014a. Voltage-tunable terahertz and infrared photodetectors based on double-graphene-layer structures. Applied Physics Letters 104 (16), 163505.

Ryzhii, V., Satou, A., Otsuji, T., et al., 2014b. Graphene vertical hot-electron terahertz detectors. Journal of Applied Physics 116 (11), 114504.

Sakai, K., 2005. Terahertz Optoelectronics. New York: Springer.

Savic, I., Milanovic, V., Vukmirovic, N., et al., 2005. Magnetic-field tunable terahertz quantum well infrared photode-tector. Journal of Applied Physics 98, 084509–084809.

Schmidt, K.H., Medeiros-Ribeiro, G., Oestreich, M., Petroff, P.M., Dohler, G.H., 1996. Carrier relaxation and electronic structure in InAs self-assembled quantum dots. Physical Review B 54, 11346–11353.

Schmidt, S.R., Seilmeier, A., Liu, H.C., 2002. Intersubband carrier dynamics in a biased GaAs/AlGaAs quantum-well infrared photodetector. Journal of Applied Physics 91, 5545–5549.

Schmuttenmaer, C.A., 2004. Exploring dynamics in the far-infrared with terahertz spectroscopy. Chemical Review 104, 1759–1779.

Sclar, N., 1984. Properties of doped silicon and Germanium infrared detectors. Progress in Quantum Electronics 9, 149–257.

Sergeev, A., Mitin, V., Stroscio, M., 2002. Quantum-dot photodetector operating at room temperatures: diffusion-limited capture. Physica B 316, 369–372.

Shen, W.Z., Perera, A.G.U., Francombe, M.H., et al., 1998. Effect of emitter layer concentration on the performance of GaAs p + -i homojunction far-infrared detectors: a comparison of theory and experiment. IEEE Transactions on Electron Devices 45, 1671–1677.

Shen, W.Z., Perera, A.G.U., Liu, H.C., Buchanan, M., Schaff, W.J., 1997. Bias effects in high performance GaAs homojunction far-infrared detectors. Applied Physics Letters 71, 2677–2679.

Shepherd, F.D., 1992. Infrared internal emission detectors. Proceedings of SPIE 1735, 250261.

Shepherd, F.D., Vickers, V.E., Yang, 1971. Schottky barrier photodiode with degenrate semiconductor active region. U. S. Patent No: 3,603,847.

Sherwin, M., 2002. Applied physics: terahertz power. Nature 420, 131.

Shklovskii, B.I., 1980. Theory of 1/f noise for hopping conduction. Solid State Communications 33, 273–276.

Siegel, P.H., 2002. Terahertz technology. IEEE Transaction on Microwave Theory and Techniques 50, 910–928.

Siegel, P.H., 2004. Terahertz technology in biology and medicine. IEEE Transactions on Microwave Theory and Techniques 52, 2438–2447.

Sizov, F., 2010. THz radiation sensors. Opto-Electronic Review 18 (1), 10.

Smith, P.R., Auston, D.H., Nuss, M.C., 1988. Subpicosecond photoconducting dipole antennas. IEEE Journal of Quantum Electronics 24, 255–260.

Stetson, S.B., Reynolds, D.B., Stapelbroeck, M.G., Stermer, R.L., 1986. Design and performance of blocked-impurity-band detector focal plane arrays. Proceedings of SPIE 686, 48–65.

Su, X., Chakrabarti, S., Bhattacharya, P., Ariyawansa, G., Perera, A.G.U., 2005. A resonant tunneling quantum-dot infrared photodetector. IEEE Journal of Quantum Electronics 41, 974–979.

Su, X.H., Yang, J., Bhattacharya, P., Ariyawansa, G., Perera, A.G.U., 2006. Terahertz detection with tunneling quantum dot intersublevel photodetector. Applied Physics Letters 89, 031117.

Sze, S.M., 1981. Physics of Semiconductor Devices. New York: John Wiley & Sons.

Szmulowicz, F., Madarasz, F.L., 1987. Blocked impurity band detectors-an analytical model: Figures of merit. Journal of Applied Physics 62, 2533–2540.

Ting, D.Z.Y., Chang, Y.-C., Bandara, S.V., Gunapala, S.D., 2007. Quantum well intrasubband photodetector for far infared and terahertz radiation detection. Applied Physics Letters 91, 073510–073530.

Tohyama, S., Teranishi, N., Konuma, K., et al., 1991. A new concept silicon homojunction infrared sensor. IEEE Transactions on Electronics Devices 38, 1136–1140.

Tong, S., Kim, H.-J., Wang, K.L., 2005. Normal incidence intersubband photore-sponse from phosphorus delta-doped Ge dots. Applied Physics Letters 87, 081104–081304.

Tonouchi, M., 2007. Cutting-edge terahertz technology. Nature Photon 1 (2), 97.

Tredicucci, A., Vitiello, M.S., 2014. Device concepts for graphene-based terahertz photonics. IEEE Journal of Selected Topics in Quantum Electronics 20 (1), 130.

Tsao, S., Lim, H., Zhang, W., Razeghi, M., 2007. High operating temperature 320×256 middle-wavelength infrared focal plane array imaging based on an nAs/InGaAs/InAlAs/InP quantum dot infrared photodetector. Applied Physics Letters 90, 201109–201309.

Tsaur, B.Y., Chen, C.K., Marino, S.A., 1991. Long-wavelength Ge_xSi_{1-x}/Si heterojunction infrared detectors and focal plane arrays. Proceedings of SPIE 1540, 580–595.

Urayama, J., Norris, T.B., Singh, J., Bhattacharya, P., 2001. Observation of phonon bottleneck in quantum dot electronic relaxation. Physical Review Letters 86, 4930–4933.

Vickers, V.E., 1971. Model of Schottky barrier hot-electron-mode photodetection. Applied Optics 10, 2190–2192.

Watson, D.M., Guptill, M.T., Huffman, J.E., et al., 1993. Germanium blocked-impurity-band detector arrays: unpassivated devices with bulk substrates. Journal of Applied Physics 74, 4199.

Watson, D.M., Huffman, J.E., 1988. Germanium blocked-impurity-band far-infrared detectors. Applied Physics Letters 52, 1602--1604.

Weerasekara, A., Rinzan, M., Matsik, S., et al., 2007. n-Type GaAs/AlGaAs heterostruc-ture detector with a 3.2 THz threshold frequency. Optics Letters 32, 1335–1337.

Williams, B., Kumar, S., Hu, Q., Reno, J., 2005. Operation of terahertz quantum-cascade lasers at 164 K in pulsed mode and at 117 K in continuous-wave mode. Optics Express 13, 3331–3339.

Williams, R., 1970. In: Willardson, R.K., Beer, A.C. (Eds.), Semiconductors and Semimetals, vol. 6. New York: Academic Press. p. 97.

Wolde, S., Lao, Y.-F., Perera, A.G.U., et al., 2014. High temperature terahertz response in a p-type quantum dot-in-well photodetector. Applied Physics Letters 105 (15),

Woolard, D.L., Jensen, J.O., Hwu, R.J., Shur, M.S., 2007. Terahertz Science and Technology for Military and Security Applications. Singapore: World Scientific Publishing Company.

Woolard, D.L., Loerop, W.R., Shur, M.S., 2003. Terahertz sensing technology. Electronic Devices and Advanced Systems Technology, vol. 1. Singapore: World Scientific Publication Co Inc.

Woolard, D.L., Loerop, W.R., Shur, M., 2004. Terahertz Sensing Technology: Emerging Scientific Applications & Novel Device Concepts. Singapore: World Scientific Publishing Company.

Xu, K.Y., Lu, X.F., Song, A.M., Wang, G., 2008. Enhanced terahertz detection by localized surface plasma oscillations in a nanoscale unipolar diode. Journal of Applied Physics 103, 113708–113808.

Yan, J., Kim, M-H., Elle, J.A., et al., 2012. Dual-gated bilayer graphene hot-electron bolometer. Nature Nanotechnology 7, 47278.

Ye, Z., Campbell, J.C., 2002. InAs quantum dot infrared photodetectors with $In_{0.15}Ga_{0.85}$As strain-relief cap layers. Journal of Applied Physics 92, 7462–7468.

Zhang, R., Fu, Z.L., Gu, L.L., Guo, X.G., Cao, J.C., 2014. Terahertz quantum well photodetectors with reflection-grating couplers. Applied Physics Letters 105 (23),

Zhang, R., Guo, X.G., Song, C.Y., et al., 2011. Metal-Grating-Coupled Terahertz Quantum-Well Photodetectors. IEEE Electronics Device Letters 32 (5), 659.

Zhang, S.K., Wang, W.B., Shtau, I., et al., 2002. Backilluminated GaN/AlGaN heterojunction ultraviolet photodetector with high internal gain. Applied Physics Letters 81, 4862–4864.

Zhang, Y.H., Luo, H.T., Shen, W.Z., 2002. Study on the quantum efficiency of resonant cavity enhanced GaAs far-infrared detectors. Journal of Applied Physics 91, 5538–5544.

Zhang, Y.H., Luo, H.T., Shen, W.Z., 2003. Demonstration of bottom mirrors for resonant-cavity-enhanced GaAs homojunction far-infrared detectors. Applied Physics Letters 82, 1129–1131.

Zhou, T., Zhang, R., Guo, X.G., et al., 2012. Terahertz imaging with quantum-well photodetectors. IEEE Photonics Technology Letters 24 (13), 1109.

Further Reading

Terahertz Devices and Applications:

Dexheimer, S.L., 2007. Terahertz Spectroscopy: Principles and Applications. Boca Raton, FL: CRC Press.

Miles, R.E., Harrison, P., Lippens, D., 2001. Terahertz Sources and Systems. Boston: Kluwer Academic Publishers.

National Research Council (U.S.), 2007. Committee on Assessment of Security Technologies for Transportation. Assessment of Millimeter-Wave and Terahertz Technology for Detection and Identification of Concealed Explosive and Weapons. Washington, DC: National Academies Press.

Sakai, K., 2005. Terahertz Optoelectronics. New York: Springer.

Woolard, D.L., Loerop, W.R., Shur, M., 2003. Terahertz Sensing Technology. River Edge, N.J: World Scientific.

Physics and Applications of QWIP, QDIP, HIWIP, and HEIWIP Structures:

Bhattacharya, P., 1993. Properties of Lattice-Matched and Strained Indium Gallium arsenide, London: INSPEC, Institution of Electrical Engineers.

Choi, K.K., 1997. The Physics of Quantum Well Infrared Photodetectors. London: World Scientific.

Henini, M., 2007. Handbook of Self Assembled Semiconductor Nanostructures Novel Devices in Photonics and Electronics. Elsevier Limited.

Liu, H.C., Capasso, F., 2000. Intersubband Transitions in Quantum Wells: Physics and Device Applications I. San Diego: Academic Press.

Liu, H.C., Levine, B., Andersson, J.Y., 1994. Quantum well intersubband transition physics and devices. Boston: Kluwer Academic.

Perera, A.G.U., Liu, H.C., Francombe, M.H., 2000. Handbook of Thin Film Devices. San Deigo: Academic Press.

Piotrowski, J., Rogalski, A., 2007. High-Operating-Temperature Infrared Photode-Tectors. Bellingham, WA: SPIE.

Razeghi, M., 1997. Long Wavelength Infrared Detectors. CRC Press.

Ryzhii, V., 2003. Intersubband Infrared Photodetectors. River Edge, NJ: World Scientific.

Schneider, H., Liu, H.C., 2007. Quantum Well Infrared Photodetectors: Physics and Applications. New York: Springer.

Adachi, S., 1994. GaAs and Related Materials. Singapore: World Scientific.

Sturge, M.D., 1963. Optical absorption of gallium arsenide between 0.6 and 2.75 eV. Physical Review 129, 2835–2836.